NTNU
Norwegian University of
Science and Technology

Jet fires

Marius Olof Bolstad

Master of Science in Mechanical Engineering
Submission date: June 2016
Supervisor: Ivar Ståle Ertesvåg, EPT
Co-supervisor: Kjell Erik Rian, ComputIT
Nils Inge Lilleheie, ComputIT
Reidar Stølen,

Norwegian University of Science and Technology
Department of Energy and Process Engineering

NTNU
Norges teknisk-naturvitenskapelige universitet
Institutt for energi- og prosessteknikk

EPT-M-2016-20

MASTEROPPGAVE

for

Student Marius Olof Bolstad

Våren 2016

Jetbrannar

Jet fires

Bakgrunn

Store mengder hydrokarbon under trykk er alltid ein tryggleiksrisiko. Ein jetbrann er ein lekkasje av høgtrykks gass/olje som brenn. Ein slik brann kan skade andre innretningar og skape fleire lekkasjar og brannar, slik at brannen aukar kraftig. Å forstå mogelege konsekvensar er viktig for design og drift av gass/olje-installasjonar på land og til havs.

Omfattande målingar frå stor-skala brannforsøk er nyleg frigjevne til bruk i open forsking frå SP Fire Research (tidlegare Sintef NBL - Norges branntekniske laboratorium. Målsetjinga er å lære meir om korleis jetbrannar utviklar seg ved å simulere nokre av desse tilfella numerisk og samanlikne med måledata.

Oppgåva er i samarbeid med ComputIT AS og SP Fire Research i Trondheim.

I oppgåva skal studenten

Vidareføre arbeidet utført som prosjektoppgåve hausten 2015 og saman med rettleiarane vidareutvikle problemstillingane der.
Eventuelt utvide og oppdatere litteraturstudiet omkring jetbrann, inkludert tilgjengelege målingar, numerisk modellering utført av andre, og tilhøyrande fysiske fenomen som turbulent strøyming, forbrenning og stråling.

Særleg aktuelle spørsmål er betre modellering av geometrien/forbrenningskammeret, verknader av dropediameter og –spreiing og sot og stråling.

Bruke eit eigna program for å simulere utslepp, spreiing og brann. Diskutere resultata, inkludert modellar og mogelege avvik mellom utrekningar og målingar

” - ”

Senest 14 dager etter utlevering av oppgaven skal kandidaten levere/sende instituttet en detaljert fremdrift- og eventuelt forsøksplan for oppgaven til evaluering og eventuelt diskusjon med faglig ansvarlig/veiledere. Detaljer ved eventuell utførelse av dataprogrammer skal avtales nærmere i samråd med faglig ansvarlig.

Besvarelsen redigeres mest mulig som en forskningsrapport med et sammendrag både på norsk og engelsk, konklusjon, litteraturliste, innholdsfortegnelse etc. Ved utarbeidelsen av teksten skal kandidaten legge vekt på å gjøre teksten oversiktlig og velskrevet. Med henblikk på lesning av besvarelsen er det viktig at de nødvendige henvisninger for korresponderende steder i tekst, tabeller og figurer anføres på begge steder. Ved bedømmelsen legges det stor vekt på at resultatene er grundig bearbeidet, at de oppstilles tabellarisk og/eller grafisk på en oversiktlig måte, og at de er diskutert utførlig.

Alle benyttede kilder, også muntlige opplysninger, skal oppgis på fullstendig måte. For tidsskrifter og bøker oppgis forfatter, tittel, årgang, sidetall og eventuelt figurnummer.

Det forutsettes at kandidaten tar initiativ til og holder nødvendig kontakt med faglærer og veileder(e). Kandidaten skal rette seg etter de reglementer og retningslinjer som gjelder ved alle (andre) fagmiljøer som kandidaten har kontakt med gjennom sin utførelse av oppgaven, samt etter eventuelle pålegg fra Institutt for energi- og prosessteknikk.

Risikovurdering av kandidatens arbeid skal gjennomføres i henhold til instituttets prosedyrer. Risikovurderingen skal dokumenteres og inngå som del av besvarelsen. Hendelser relatert til kandidatens arbeid med uheldig innvirkning på helse, miljø eller sikkerhet, skal dokumenteres og inngå som en del av besvarelsen. Hvis dokumentasjonen på risikovurderingen utgjør veldig mange sider, leveres den fulle versjonen elektronisk til veileder og et utdrag inkluderes i besvarelsen.

I henhold til "Utfyllende regler til studieforskriften for teknologistudiet/sivilingeniørstudiet" ved NTNU § 20, forbeholder instituttet seg retten til å benytte alle resultater og data til undervisnings- og forskningsformål, samt til fremtidige publikasjoner.

Besvarelsen leveres digitalt i DAIM. Et faglig sammendrag med oppgavens tittel, kandidatens navn, veileders navn, årstall, instituttnavn, og NTNUs logo og navn, leveres til instituttet som en separat pdf-fil. Etter avtale leveres besvarelse og evt. annet materiale til veileder i digitalt format.

☐ Arbeid i laboratorium (vannkraftlaboratoriet, strømningsteknisk, varmeteknisk)
☐ Feltarbeid

NTNU, Institutt for energi- og prosessteknikk, 13. januar 2015

Olav Bolland
Instituttleder

Ivar S. Ertesvåg
Faglig ansvarlig/veileder

Medveiledere/kontaktpersoner:
Kjell Erik Rian, ComputIT AS
Nils Inge Lilleheie, ComputIT AS
Reidar Stølan, SP Fire Research

Abstract

Knowledge of the impacts of fire is a big part of hazard analysis, and thorough fire predictions could potentially save both life and belongings. In the 1990's, a set of fire tests on compartment fires was conducted at SINTEF NBL in Trondheim, Norway. The results from the tests have, until recently, been restricted from public view. The partly release of the results from the fire tests has presented the opportunity of conducting simulations based on the fire tests, for validations of simulation software. In this thesis, simulations of one of the fire tests, fire test JF5, in Blast and Fire for Topside Structures, Test Programme F3, have been conducted in the gas dispersion and fire simulator Kameleon FireEx (KFX) by Computational Industry Technologies AS (ComputIT), for a parameter study on fire development in under-ventilated enclosures and for comparison between experimental data and numerical simulations.

The simulations conducted in this thesis, have shown large impacts on fire development from parameters with uncertain modelling. The droplet diameter in the fuel spray and the enclosure modelling were decisive on flame development in an under-ventilated enclosure. The results revealed differences between the simulated cases that was related to combustion in the upper layer of the compartment. Simulations with combustion in the upper layer of the compartment, recorded significantly higher temperatures, than the simulations without combustion in the upper layer. The combustion in the upper layer of the compartment seemed to highly depend on air entrainment. Parameters that affect flow and air entrainment, on the inside of the compartment, are therefore important.

The results obtained do not make it possible to draw any certain conclusions on validity and reliability of the computational software, for simulating under-ventilated fires. The modelling uncertainties of parameters that were of great importance were too large. Further research into important parameters, and how they should be modelled, are needed.

Sammendrag

Kunnskap om skadepotensialet i branner er viktig ved utarbeiding av sikkerhetsanalyser, hvor nøye gjennomførte brannsimuleringer potensielt kan spare både liv og eiendeler. På 1990-tallet, ble branntester på underventilerte branner gjennomført ved SINTEF NBL i Trondheim. Resultatene fra disse testene har, inntil nylig, vært lukket for offentligheten. Tilgjengeligheten til noen av resultatene fra disse testene, har åpnet en mulighet for å gjennomføre simuleringer basert på branntestene, for validering av programvare. I denne oppgaven er simuleringer av en av disse brenntestene, branntest JF5 fra Blast and Fire for Topside Structures, Test Programme F3, blitt gjennomført i simuleringsprogramvaren Kameleon FireEx (KFX) fra Computational Industry Technologies AS (ComputIT), som en parameterstudie på brannutvikling i underventilerte rom, og til sammenligning av simuleringsverktøyet mot måledata.

Simuleringene gjennomført i denne oppgaven, har vist at ulike parametere kan gi store variasjoner i brannutvikling i underventilerte rom, der store utslag med høye temperaturer er relatert til forbrenning i øvre deler av rommet. Forbrenningen viste seg å være avhengig av lufttilstrømming inn i rommet og blanding med brensel i de øvre lagene i rommet. Noen av parameterene som, i denne oppgaven, viste seg å være betydelige, var dråpediameter i brenselsprayen og hvordan geometrien var modellert. Usikkerheten rundt modellering av disse parameterene var betydelig, noe som påvirker de oppnådde resultatene.

Resultatetene presentert i denne oppgaven gjør det ikke mulig å trekke konklusjoner på validiteten og reliabiliteten til regneverktøyet. Usikkerheten rundt noen av parameterene, som har vist seg å være betydelige, var for stor. Videre forskning på parametere, som viser seg å være av betydning for brannutviklingen, og hvordan disse kan modelleres, bør gjennomføres.

Preface

This master thesis was written in 2016, as the final step towards my master degree in Mechanical Engineering at the department of Energy and Process Engineering, at NTNU in Trondheim. The thesis was given as a cooperation between NTNU, Computational Industry Technologies AS (ComputIT) and SP Fire Research (SPFR).

For all their dedication and help along the way, I would like to thank my supervisors Ivar S. Ertesvåg, Kjell Erik Rian, Nils Inge Lilleheie, Rune Natten Kleiveland & Reidar Stølen. I would also like to thank Trond Evanger, Anette Mjøen and all the other people at ComputIT, for a pleasant year and the nice lunches. Lastly, I would like to express my gratitude to mom and dad, for paving the way, and Oda Elisabeth, for her unconditional support and patience.

Trondheim, 2016-06-08

Marius Olof Bolstad

Contents

Nomenclature

Roman letters

A	Area	m^2
A_c	Parameter in radiation emissivity model	
a	Absorption coefficient	m^{-1}
a_m	Magnitude of velocity	m/s
a_s	Speed of sound	m/s
B	Buoyancy	W/kg
B_c	Parameter in radiation emissivity model	
B_d	Transfer number	
b	Parameter in radiation emissivity model	
C_2	Constant in radiation emissivity model	mK
C_D	Drag coefficient	
C_{D1}, C_{D2}	Constants in cascade model	
C_p	Specific heat capacity	J/(kg·K)
$C_{\epsilon 1}$, $C_{\epsilon 2}$, $C_{\epsilon 3}$, C_μ	Constants in $k-\epsilon$ equations	
c	Parameter in radiation emissivity model	
Co	Courant number	
D	Mass diffusivity	m^2/s
d	diameter	m
E	Constant in the log law model	
F_{liq}	Momentum source term	m/s^2
g	Acceleration	m/s^2
H_h	Enthalpy diffusion coefficient	kg/m^2s
H_m	Momentum diffusion coefficient	kg/m^2s
H_R	Heat of reaction	J/kg
h	Enthalpy	J/kg
I	Radiation intensity	W/m^2
K	Conductivity	W/mK
k	Turbulence energy	J/kg

k_0	Constant in radiation emissivity model	
L	Length scale	m
L_h	Latent heat of evaporation	J/kg
L_n	Nozzle width	m
$\dot{\mathrm{M}}$	Mass flow rate	kg/s
m	Mass	kg
$\dot{\mathrm{m}}$	Mass transfer	s^{-1}
MW	Molar mass	kg/kmol
N_p	Number of real droplets	
N_s	Number of simulated droplets	
n	Amount of substance	mole
n_0	Rate of spontaneous formation of nuclei	$(\mathrm{m}^3\mathrm{s})^{-1}$
Nu	Nusselt number	
p	Pressure	Pa
Pr	Prandtl number	
$\dot{Q}$	Rate of heat	$\mathrm{W/m}^3$
$\dot{Q}_d$	Rate of heat conducted into droplet	$\mathrm{W/m}^2$
q	heat flux	$\mathrm{W/m}^2$
$\dot{R}$	Reaction rate on mass basis	s^{-1}
r	radius	m
r_s	Stoichiometric oxygen requirement	
Re	Reynolds number	
S_{liq}	Energy source term	W/kg
$S_{n,i}$	Energy contribution from beam i, passing through control volume n	W
s	Coordinate along the path of radiation	m
$\hat{s}$	mean path length	m
Sc	Schmidt number	
Sh	Sherwood number	
T	Temperature	K
T^+	Dimensionless Temperature in log law model	
t	Time	s
U^+	Dimensionless velocity in the low law model	
U^*	Frictional velocity in the log law model	m/s
u	velocity	m/s
V	Volume	m^3
v	velocity	m/s
We	Weber number	
X	Molar fraction	
x	Distance	m

Y	Mass fraction	
y	Distance	m
y^+	Dimensionless distance in the log law model	
z	Distance	m

Greek letters

β	Pressure fraction in radiation emissivity model	
γ	Mass fraction in EDC	
ϵ	Dissipation of turbulence energy	W/kg
$\hat{\epsilon}$	Emissivity Coefficient	
ζ	Parameter in the radiation emissivity model	
η	Fine structure mixing rate coefficient	
θ	Dispersion angle	
κ	Parameter in radiation emissivity model	
$\hat{\kappa}$	Constant in the log law model	
μ	Dynamic viscosity	kg/(m· s)
ν	Kinematic viscosity	m^2/s
ξ	Number of real droplets represented of by each numerical droplet	
ϕ	Random variable	
$\phi^{(3)}$	Penta-gamma function	
ρ	Density	kg/m^3
σ	Stefan–Boltzmann constant	$W/(m^2\ K^4)$
σ_a	Surface tension	N/m
σ_e	Turbulence-Prandtl number for e	
σ_h	Turbulence-Prandtl number for h	
σ_k	Turbulence-Prandtl number for k	
σ_l	Molecular Prandtl number	
σ_T	Turbulence Prandtl number	
σ_t	Turbulence-Prandtl number for t	
σ_u	Turbulence-Prandtl number for u	
σ_Y	Turbulence-Schmidt number	
σ_ϵ	Turbulence-Prandtl number for ϵ	
τ	Shear stress	Pa
τ^*	Time scale in fine structure	s
$\tau_{\hat{\epsilon}}$	Temperature scale in the radiation emissivity model	K
$\hat{\tau}$	Time scale	s
$\hat{\tau}_a$	Time scale	s
χ	Fraction of fine structure that reacts	
Ω	Solid angle	

Subscripts and superscripts

–	Reynolds average
~	Favre average
’	Fluctuating value (Reynolds decomposition)
”	Fluctuating value (Favre decomposition
→	Vector
*	Fine structure
0	Surroundings
cond	Conduction
conv	Convection
d	Droplet
eff	Effective
f	At cell next to wall
fu	Fuel
g	Gas
gs	From solid to gas
l	liquid
liq	Liquid
liq,s	From liquid to solid
k	for species k
max	maximum
min	minimum
n	cell number n
nuc	nucleus
ox	Oxidant
p	particle
Pr	Product
rad	Radiation
reac	reaction
s	Solid
sg	From gas to solid
sur	At the wall or surface
t	for turbulence
tot	Total
w	water
λ	for surroundings

Abbreviations

3D	Three-dimensional
CAD	Computer-aided drafting
EDC	Eddy Dissipation Concept
KFX	Kameleon FireEx
SMD	Sauter Mean Diameter

Chapter 1

Introduction

In the early 1990's a research on fire development was established as a follow-up of the fire accidents on Piper Alpha and Scandinavian Star. Knowledge of the impacts of fire is a very important part of hazard analysis. Thorough fire predictions would potentially save both life and prevent loss of property. As part of this research, fire tests on compartment fires were conducted at SINTEF NBL in Trondheim, Norway. The results from the tests have, until recently, been restricted from public view.

Fire safety design is to a large degree based on fire simulations. By opening of the fire tests from SINTEF NBL, a possibility of verifying simulation software against fire tests is made available. A verification of fire simulation software could potentially increase the reliability and the validity of simulations, leading to better fire safety designs.

1.1 Limitations, structure and topic of the thesis

Through meetings with the supervisors Ivar S. Ertesvåg, Kjell Erik Rian and Nils Inge Lilleheie, the topic, limitations and structure of this thesis have been prepared.

Limitations

When simulating a spray fire inside a compartment, one is presented with indefinite possible solutions on how to set up the case. In this thesis, the limitations have been set by the fire test JF5 in the Blast and Fire Engineering for Topside Structures, Test Programme F3, found in Drangsholt et al. [6]. All simulations were set up either to be as similar to the fire test as possible, or to investigate parameters of uncertainty or of special importance in the fire test.

Structure of thesis

This thesis is set up as a scientific report. First, an introduction to the topic of the thesis is presented. The introduction also includes a review of previous work, with a summary of the Blast and Fire Engineering for Topside Structures, Test Programme F3. This is followed by a short description of the models used for the calculation. To get an understanding of how the

calculations are performed, the models are described in a general manner. This is followed by a description of the setup of the simulations in this thesis, with modelling choices and simulation procedure. The results from the simulations are presented in Ch. (4), followed by a discussion in Ch. (5). In the latter, the results from the simulations will be discussed on the basis of the investigation on fire development. A comparison between the results from the simulations in this thesis and the results from JF5, is also presented. Final remarks are presented in the conclusion with a recommendation on further work.

The objective of this thesis

The objective of this thesis is to compare the results obtained through simulations in the gas dispersion and fire simulator Kameleon FireEx (KFX) from Computational Industry Technologies AS (ComputIT) against results from the fire test JF5 in Blast and Fire Engineering for Topside Structures, Test Programme F3. A parameter study investigating the effects of enclosure modelling and spray dispersion on fire development is also included. Important parameters for comparing the results of the simulations are temperature, radiation heat flux, oxygen quantity and flow velocities.

The aim of the thesis is to further develop the knowledge on compartment spray fires and how these are modelled in computational fluid dynamics.

1.2 Previous work

Previous research on spray combustion and under-ventilated fires is described for later comparison with results presented in this thesis.

1.2.1 Spray combustion

Williams [43] presents an overview of spray combustion and related phenomena. The general descriptions of atomisation found here, are similar to the more recent publication by Ashgriz [1]. A burning spray is combustion with a non-uniform composition. This will give poorly defined combustion zones and irregularities in flame propagation. The main features of a spray flame are atomisation, air entrainment and flame stabilisation, where the mixing process is controlled by the geometry of the combustion chamber, spatial distribution and momentum of the spray and the air flow. A thorough analysis of droplet size distribution and spray angle is important in spray combustion [43](p.1,2,35).

Droplet atomisation

Much research has been done in the fields of spray combustion, where a thorough understanding on the atomisation of droplets is needed in the construction of diesel combustion engines. Williams [43] discusses the formation of a droplet from a liquid flow. When a liquid

flow, under pressure, is forced through an orifice, an unstable jet of high velocity will start to disintegrate after leaving the orifice [43](p.54). A spray with a spectrum of different droplet sizes will be produced, where the size distribution of the spray depends on the distance from the atomiser. Small diameter droplets accelerate faster than large diameter droplets. Droplet collisions will also influence the droplet sizes. Calculations on all the different droplet sizes are computationally demanding, leading to the practice of using average combustion characteristics with mean droplet diameters [43](p.35,45).

The shape of the atomizer will influence the liquid break up. An annular orifice will give a hollow or solid cone spray. Droplets in solid cone sprays tend to be smaller than those in hollow cone sprays. If the jet is unstable, columns of liquid will be produced. These columns can break into rows of droplets, if the column length is greater than the column circumference. Because different columns have different diameters, a wide range of droplet sizes is produced. For a simple plain-orifice atomizer the Sauter mean droplet diameter is in the range of 90 to 200 μm [43](p.53,54,55).

Merrington and Richardson [26] split the atomisation process into a three step process, consisting of flow enlargement leading to sinuous shaped fluctuations and finally atomisation. Ashgriz [1](p.3-5) describes that the instability of the jet is related to axial disturbances. If the axial disturbance has a wavelength larger than the diameter of the jet, the jet will become unstable. The jet will break when the amplitude of the disturbance reaches the jet radius, and a droplet is formed by each wavelength of the disturbance. For each wavelength of an unstable disturbance, one main drop and none, one or several smaller (satellite) drops are formed. The disturbance with the maximum growth rate will lead to the break up of the jet and the resulting droplet size will be in the order of the wavelength of this disturbance.

Evaporation and combustion

Williams [43] produces one simplified way of looking at spray combustion, as heterogeneous combustion. The process is split into different steps: Evaporation, mixing, ignition, burning and combustion products. The droplets act as a fuel source, where the evaporation of the droplets leads to gaseous fuel. The gaseous fuel mixes with the oxidizing environment resulting in a combustible mixture. At a certain temperature, the mixture ignites and produces a flame. The combustion produces gas phase products, ash and soot. The combustion products can recirculate and transfer heat to the reactants, contributing to the combustion, and leave the combustion zone as exhaust. Further oxidation of the reaction products can produce heat [43](p.2,27,111).

At low droplet concentrations and high droplet separations the droplets will burn as single droplets, and at high droplet concentration and low separations the droplets vaporise and burn at an external boundary of the spray. The burning taking place at an external boundary, is due to the local air-fuel ratio inside the spray being too low for combustion. Droplets break off from the spray, vaporise and burn externally [43](p.110). Onuma et al. [30] and Onuma and Ogasawara [29] found that by using an air-atomising burner, the spray did not react as

individual droplets, where every drop burn individually. The vapour from the fuel droplets will concentrate and burn like a gas diffusion flame.

The flame zone can be seen as a reaction zone with cold fuel and oxidant on one side and hot combustion products on the other side. The properties of the unburnt spray dictate the combustion products. Large droplets may give incomplete combustion in the flame zone and unburnt fuel among the products. Small droplets may give complete evaporation and combustion with gaseous reactants. The time to reach complete combustion may be influenced by the combustion zone length, liquid fuel volatility, air-fuel ratio on the reactants side and uniformity of the mixture distribution [43](p.81,111).

Emission of particulate materials like soot and gaseous emissions like CO and CO_2 are frequently present in combustion of liquid sprays. The composition of the product, regarding different particulates, depends on the composition of the fuel oil, particularly the concentration of aromatics and asphaltenes. The amount of soot produced depends on residence time, turbulence and temperature. The soot particles produced are similar for all flames. Some hydrocarbon fuels have a greater tendency to produce soot than others. The soot production depends on fuel rich conditions, where the transition from non-sooting to sooting flames depends on a critical oxygen concentration [43](p.127,128,129,130,131). Fuel rich conditions will produce more soot than fuel lean conditions [4]. The soot can both absorb and emit radiation. If the absorbed radiation is higher than the emitted radiation, the soot will act as a radiation sink preventing radiation from the flame to reach the surroundings. If the emitted radiation is higher than the absorbed radiation, the soot will contribute to thermal radiation to the surroundings [28](p.283,284,387). This provides a possibility for higher thermal radiation in fuel rich conditions [4]. Given the non-uniform composition in a spray flame, a spray flame will always have local fuel rich zones that promote sooting. The sooting of a spray flame can also be seen through the yellow luminosity of the flame. The droplet diameters and dispersion angle will influence the sooting of the flame. Small droplet diameters and large droplet dispersions will ensure good mixing of the fuel with the oxidant and reduced sooting from the flame [43](p.130,131). The production of carbon monoxide depends on temperature and amount of excess air in the combustion. Low levels of excess air will give higher concentrations of carbon monoxide. The carbon monoxide is formed in the reaction zone, by rapid oxidation of hydrocarbons by oxygen. The oxidation of carbon monoxide to carbon dioxide is much slower, giving above equilibrium values of carbon monoxide in the reaction zone. The carbon monoxide may be oxidised to carbon dioxide in the post-flame zone. For combustion with short residence times, the concentration of carbon monoxide, in the product composition, will be higher than for long residence times [43](p.136).

Hydrocarbon mixtures have different boiling points resulting in different burning behaviour, compared to single component droplets. Flashing of some of the components of the droplet can give bubble formation inside the droplet causing droplet disintegration. Mixtures with components with high boiling points can give high droplet temperatures initiating

thermal decomposition [43](p.86).

The evaporation of the droplet is controlled by heat from the environment, where the evaporation of the droplets will absorb some of the heat energy from radiation [8]. The evaporated fuel vapour will diffuse from the droplet surface into the ambient environment. This diffusion of the vapour is controlled by the species gradient through the ambient medium, where the concentration of fuel is higher at the surface of the droplet than in the ambient medium. As the fuel vapour diffuses away from the droplet, the droplet radius will shrink due to mass loss until the droplet is completely evaporated [38](p.98-103).

1.2.2 Combustion in under-ventilated geometries

Flow characteristics

The mixing of the reactants is controlled by the geometry of the combustion chamber [43]. An experimental study done by Hwang et al. [14] on a vented, insulated enclosure showed that the flow inside a combustion chamber varied remarkably with a change from an over-ventilated room to an under-ventilated room. The fuel used was heptane, released as a pool fire at the centre of the floor area. In the over-ventilated case, the flow was going into the compartment close to the floor of the vent. The flow was entrained into the flame and followed the flame and plume to the roof of the compartment. The flow flowed along the roof towards the vent and exited the room through the upper part of the vent. At the back of the enclosure, a flow rotating the opposite way was observed. Combustion products from the flame flowed along the roof towards the back wall, down the back wall and along the floor, before being entrained by the flame. An increase in flame size led to the flame front shifting towards the rear of the room, giving larger vent rotational flow and smaller back wall rotational flow. An increase in heat release rate gave a decrease in oxygen concentration and a temperature increase, especially close to the back wall of the enclosure [14].

Shifting to an under-ventilated case, the flow characteristics inside the compartment changed. The flame attached to the burner only on the front side, and the flame front had direction towards the vent, with most of the burning regions located on the outside of the compartment. Some of the combustion products circulated inside the compartment. The products flowed from the flame, along the ceiling of the enclosure towards and down the back wall. From the back wall, the products flowed along the floor before being entrained into the flame. The residence time, for the products in the under-ventilated case, was longer than for the over-ventilated case. The long residence time in the upper layer, as well as high temperatures and fuel-rich conditions, may have led to increased heat loss to the walls and increased carbon monoxide and soot formation. A sharp gradient of oxygen species concentration was observed across the flame. The oxygen concentration on the back wall side of the flame was nearly zero, whereas, the oxygen concentration on the vent side of the flame was approximately atmospheric. The temperature distribution inside the compartment was approximately uniform. The highest temperatures were located close to the vent, with a tem-

perature decrease with the rotation of the flow inside the compartment. The concentration of O_2 was higher near the sidewalls, than in the centre of the compartment. The oxygen inflow at the centre of the vent reacted at the flame front, while the oxygen inflow at the edges flowed further into the compartment and reacted with the fuel closer to the pool [14]. Variation of fuel placement led to significant changes in temperature, heat flux, and carbon dioxide and carbon monoxide distributions at the back wall of the enclosure. On the vent side of the fire, not much changes were expected with variation of fuel placement [15].

Full-scale experiments on a pool fire in an enclosure conducted by Steckler et al. [36], showed that changes in ambient temperature of up to 20^oC can give up to 12% change in opening flow rates, where opening flow rates increase with fire strength.

The upper layer

Idealized fire experiments performed at Harvard University and the California Institute of Technology, imitated an enclosure fire by placing a hood above a fire. The fire tests produced an upper layer inside the hood, that was comparable to the upper layer in an enclosure fire [32]. At temperatures of above 800K, the combustion gases in the upper layer became reactive [31], while at temperatures below 700K, the upper layer gases were largely unreactive. Increasing temperatures in the hood also gave shorter residence time needed for complete reaction [32]. For under-ventilated conditions, significant amounts of carbon monoxide formed inside the enclosure. The carbon monoxide formation took place when the fire plume entered the upper layer of rich combustion products [33]. The carbon monoxide production also depended on fuel composition, where oxygen containing fuels generated more carbon monoxide. For fuel rich conditions, a higher temperature resulted in a more complete oxidation of the fuel, where the combustion products were strongly related to the air-fuel ratio and temperature of the upper layer [32]. Low air-fuel ratio and high temperatures (above 1100K) gave higher production of carbon monoxide [31] [32]. The fuel was firstly oxidised to produce carbon monoxide, before the remaining oxygen was used to further oxidise the carbon monoxide to carbon dioxide. The chemical reactions could generally be assumed to take place either in the fire plume or the upper layer gases [32]. Higher temperatures in the upper layer also led to an increase in carbon dioxide concentration [32]. Gottuk et al. [12] have also done research on compositions in the upper layer, where it was found that an increase in carbon monoxide concentration with increasing temperature was related to increased hydrocarbon oxidation. Temperatures above 900K accelerated the carbon monoxide oxidation, leading to the increase in carbon dioxide concentration. However, hydrocarbon oxidation occurred faster than carbon monoxide oxidation, giving net increase in carbon monoxide levels [12].

1.2.3 Blast and fire engineering for topside structures–Test program F3

The simulated cases in this thesis are based on the fire test JF5 from Blast and Fire engineering for topside structures, test programme F3. The test programme was conducted during the years 1994 and 1995 at SINTEF energy – Norwegian Fire Research Laboratory (SINTEF NBL) [6]. A set of experiments on jet fires in ventilated compartments was conducted with the aim of improving the understanding of offshore fires in partially confined areas. The program consisted of 22 test cases, 15 jet fire tests and 7 pool fire tests. 21 of the 22 tests used condensate as fuel, while one used propane. Tests with vertical as well as tests with horizontal jet releases were performed. The tests were performed in two compartments of different size. One was a 415 m^3 room, as the one given in figure 3.1, the other was a room with similar geometry, but the scale reduced to 135 m^3 [4].

For the vertical jet release experiments, it was observed that, for stable fire, air was entrained close to the vent. This gave intense combustion in the lower region of the smoke layer. Increasingly fuel rich conditions led to an increase in temperature and heat fluxes at the walls. The depletion of air gave an increase in soot production towards the back wall of the enclosure. The temperatures and heat fluxes close to the ceiling of the compartment were largely unaffected by the increasingly fuel rich conditions. The effect of reduction in compartment size was negligible [4].

Test JF5

Test JF5 was one of the tests in test program F3 using a condensate fuel. The release was vertical, pointing towards the ceiling of the compartment, and the room size was 415 m^3 [6].

When the fuel was injected into the enclosure, some of the lighter hydrocarbons immediately flashed into gas phase. The liquid part of the fuel was atomized to a spray. As the spray moved towards the ceiling of the enclosure, some of the drops evaporated and some of the drops hit the ceiling before evaporation. The fuel that hit the ceiling, resulted in rain of fuel from the ceiling, initially forming small pools on the floor around the release point. The gas phase fuel was ignited to produce a flame. Initially, when the enclosure was filled with oxygen, the flame developed as an open fire. The fuel pools around the release, burned as pool fires for a short time before being evaporated. Sufficient oxygen was observed at the inside of the enclosure, leading to a fuel-controlled fire. The heat produced inside the compartment gave a net outflow of gas through the vent. This fire development lasted for approximately 10-20 seconds [6]. As the jet fire progressed, the flame hit the ceiling, and a growing smoke layer formed close to the ceiling. The oxygen inside the enclosure was slowly depleted. The smoke layer continued to grow, reaching the vent. This gave an outflow of smoke through the upper part of the vent and a build-up of a well-defined interface between the smoke in the upper part of the enclosure, and air in the lower part of the enclosure. An inflow of air through the lower part of the vent was observed, through measurements with Bi-directional low-velocity probes. These probes measured differential pressures, and the

velocities were derived from the measured pressure and temperature at each point. Partially combusted products filled the smoke layer, eventually fulfilling the temperature and composition requirements for combustion. This gave ignition and a flame propagation at the interface between the air and smoke layer. The flame propagated towards the vent and ignited the outflowing smoke. This resulted in a flame with a flame height of approximately 9-10 m, on the outside of the enclosure. Approximately 600 seconds after jet flame ignition, the heat flux, temperature and composition of the smoke layer were stabilized with only small transient variations. During the simulation, the fuel flow rate was varied. The flow of fuel started at a level of 0.85 kg/s. This flow rate was held stable for approximately 14 minutes. After the first 14 minutes, the fuel flow rate was reduced to 0.75 kg/s. The flow rate of 0.75 kg/s was held stable for 2 minutes, before the fuel flow rate was stopped. The change in fuel flow rate did not seem to have a significant effect on the measured temperatures [6].

During the JF5 fire test, temperatures and heat fluxes were logged at several positions in the enclosure. In this thesis, the results from four logging points are included for comparisons later in the thesis. The positions of the logging points are presented as points 1-4 in Fig. (1.1). All four logging points recorded thermocouple temperature. The results from Logging points 1-4 are given in Figs. (1.2–1.5). The figures represent the measured thermocouple temperatures. No data on thermocouple temperature measurement errors was provided in Drangsholt et al. [6]. More detailed information about the Blast and Fire Engineering for Topside Structures, Test Programme F3, generally, and Fire test JF5, specifically, can be found in Drangsholt et al. [6] and Chamberlain et al. [4].

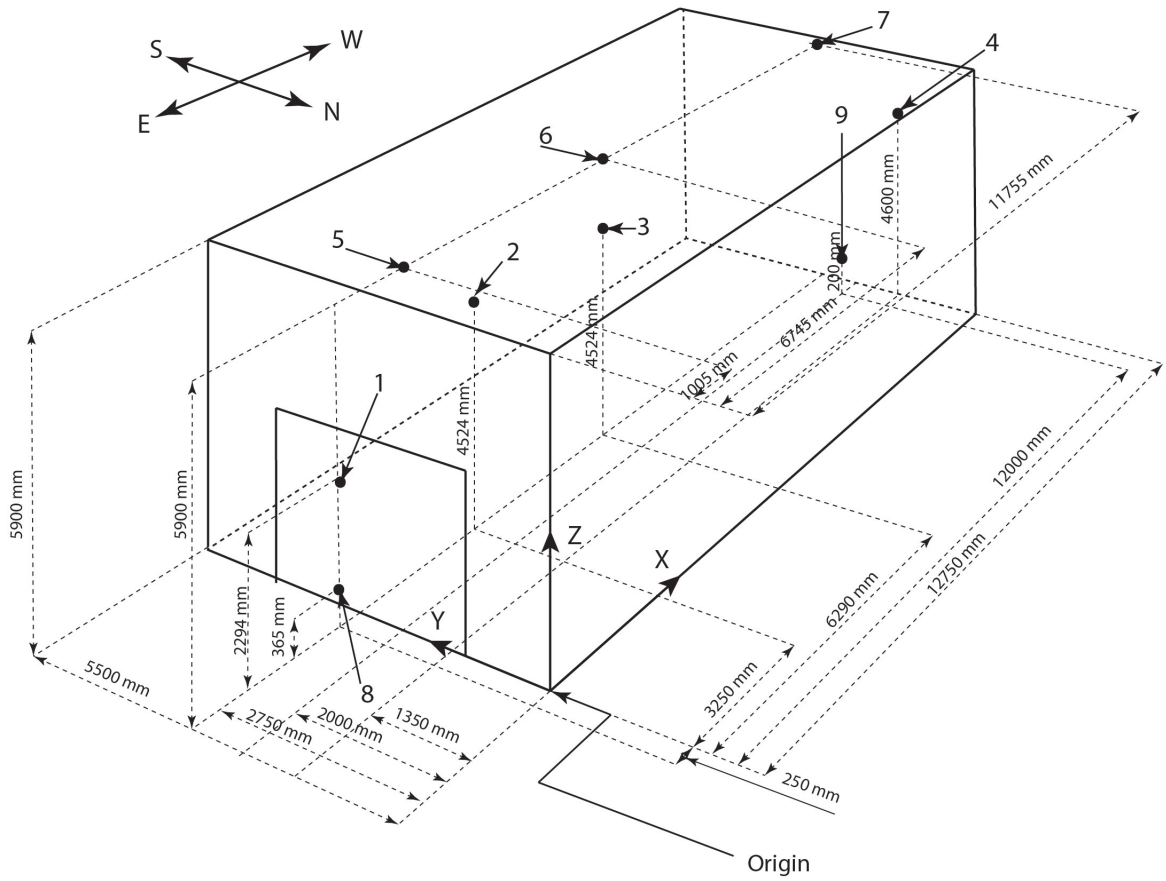

Figure 1.1: Position of logging points inside the enclosure

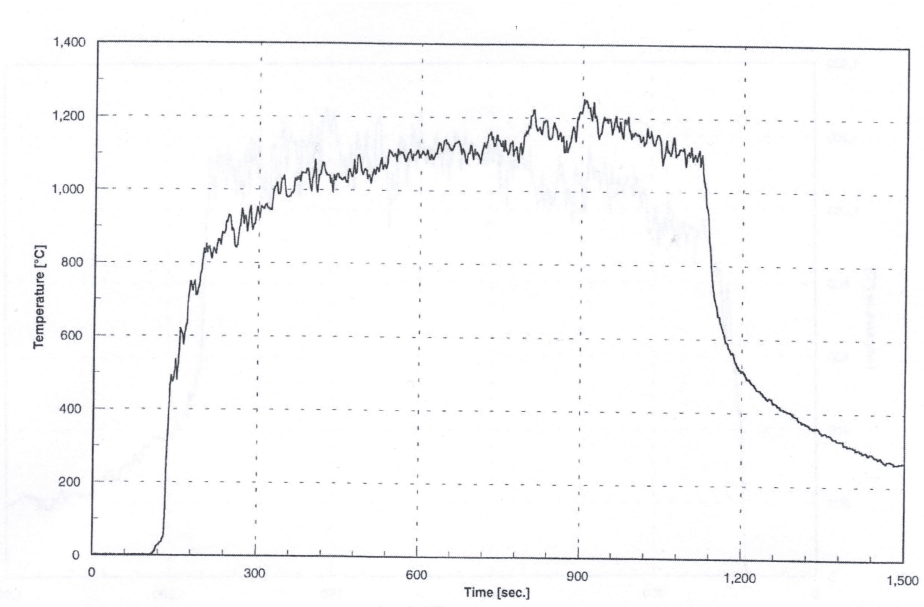

Figure 1.2: Thermocouple temperature measured at Logging point 1. Fire test JF5, Blast and Fire engineering for topside structures test programme F3. SINTEF NBL [6]

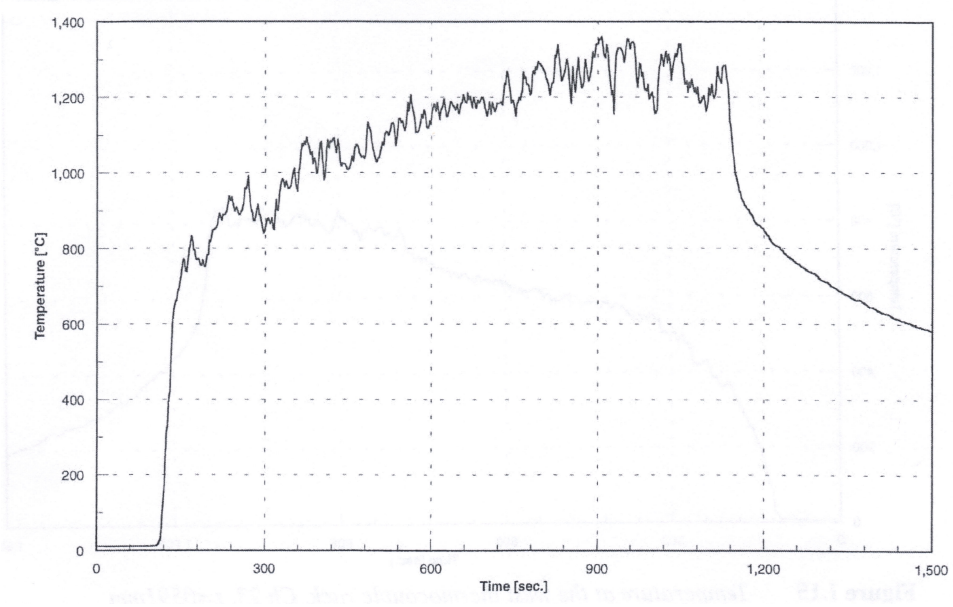

Figure 1.3: Thermocouple temperature measured at Logging point 2. Fire test JF5, Blast and Fire engineering for topside structures test programme F3. SINTEF NBL [6]

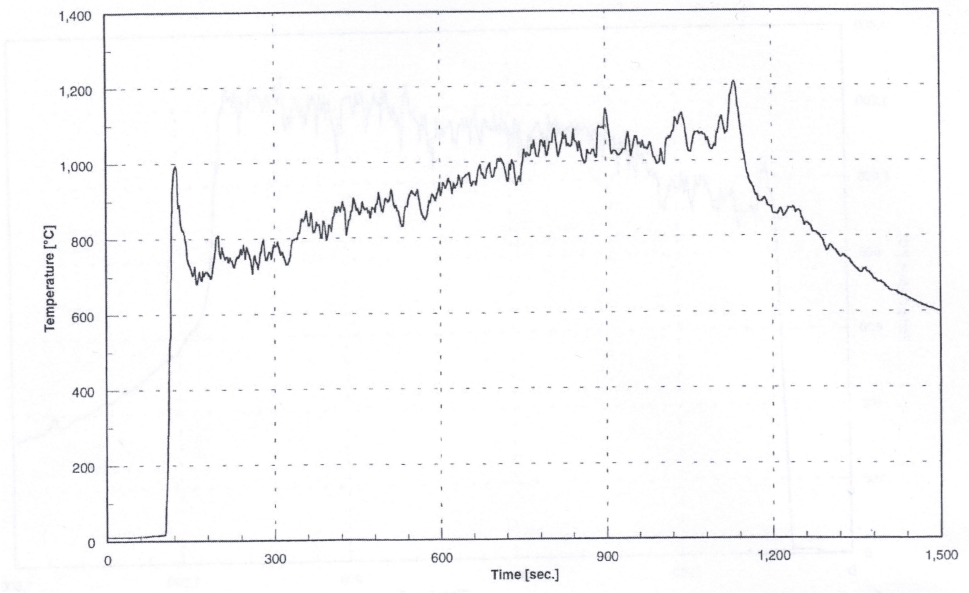

Figure 1.4: Thermocouple temperature measured at Logging point 3. Fire test JF5, Blast and Fire engineering for topside structures test programme F3. SINTEF NBL [6]

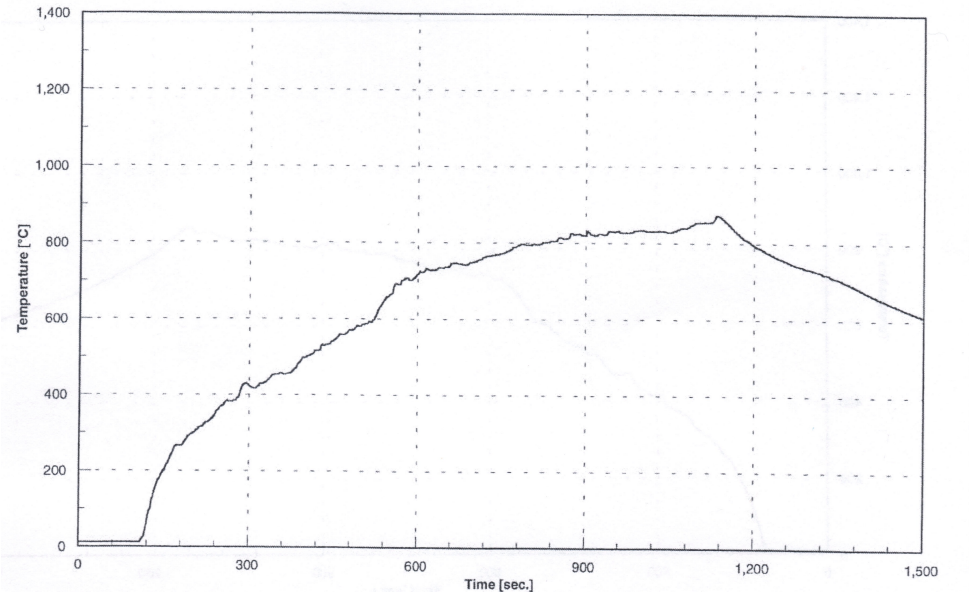

Figure 1.5: Thermocouple temperature measured at Logging point 4. Fire test JF5, Blast and Fire engineering for topside structures test programme F3. SINTEF NBL [6]

1.3 Present contribution

In this thesis the focus will be on investigation on enclosure modelling and spray dispersion. The following parameters will be investigated and discussed:

- Effect of 3D CAD geometry import into Kameleon FireEX (KFX).
- Effect of solid cell construction.
- Effect of compartment wall insulation.
- Effect of ventilation opening size.
- Effect of spray composition modelling: Single- and multi-component sprays.
- Effect of fuel flow rate.
- Effect of Droplet size.
- Effect of Dispersion angle.
- Effect of varying Courant number.

1.4 Short description of cases

A selection of 13 different simulations are run. Each representing a part in an investigation into the parameters in Sec. (1.3). A short description of the cases follows:

1. The advanced geometry case. This is the base case. It is set up to be as close to the fire test JF5 as possible. A detailed 3D CAD model is imported. The geometry and properties are altered in the calculation domain after import. A multi-component fuel spray with calculated droplet diameters and spray angle of 10° is defined.
2. The simple geometry case. Identical to the advanced geometry case (base case) except a different CAD model is imported.
3. The no-imported-geometry case. Identical to the advanced geometry case (base case) except that no CAD geometry is imported. The geometry is made directly in the KFX calculation domain window.
4. The KFX geometry case. Identical to the advanced geometry case (base case), except that no alterations to the geometry model and properties are made in the KFX calculation domain.
5. The solid cell case. Identical to the advanced geometry case (base case), except that all thin walled cells are changed to solid cells.

6. The adiabatic case. Identical to the advanced geometry case (base case), except that the conductivities of the solid structures, K, are changed to 10^{-6}.

7. The big vent case. Identical to the advanced geometry case (base case), except for a larger ventilation opening.

8. The small diameter case. Identical to the advanced geometry case (base case), except for smaller initial droplet diameters in the spray.

9. The large diameter case. Identical to the advanced geometry case (base case), except for larger initial droplet diameters in the spray.

10. Small dispersion angle case. Identical to the advanced geometry case (base case), except for a narrower spray dispersion angle.

11. Large dispersion angle case. Identical to the advanced geometry case (base case), except for a wider spray dispersion angle.

12. The one-component case. Identical to the advanced geometry case (base case), except for the fuel composition being altered to a one-component fuel, decane.

13. The low fuel flow rate case. Identical to the advanced geometry case (base case), except the fuel flow rate is reduced to half of that specified in the advanced geometry case (base case).

Chapter 2

KFX models

In this chapter, the models behind the calculations in Kameleon FireEx (KFX) are presented. In the numerical simulation, a set of equations are solved for every numerical iteration and in every cell inside the calculation domain. The equations are chosen, because of their ability to solve physical phenomena related to spray combustion.

2.1 Transport equations

To describe the transient transport and conservation of mass, momentum and heat through the calculation domain, a set of transport equations are solved. The transport equations are Favre averaged equations. The Favre averaging is done because fire or combustion problems can have large variations in densities, due to large temperature variations.

A variable can be decomposed into a density weighted average mean component (Favre averaged component), and a density weighted average fluctuating part by the equation [7](p.223):

$$\phi = \widetilde{\phi} + \phi'' \tag{2.1}$$

2.1.1 Gas phase governing equations

Continuity equation model

The conservation of mass for the gas phase inside the calculation domain, is solved through a continuity equation model [39]:

$$\frac{\partial \overline{\rho}}{\partial t} + \frac{\partial \overline{\rho}\widetilde{u}_j}{\partial x_j} = \overline{\rho}\widetilde{\dot{R}}_{\text{liq}} \tag{2.2}$$

$\widetilde{\dot{R}}_{\text{liq}}$ is the source term describing the addition of gas phase mass, due to vaporisation of the liquid fuel spray. This source term can be found in the spray model, Eq.(2.98) .

Momentum equation model

The Navier–Stokes equations are used to model the conservation of momentum of the gas phase, along the coordinate directions [39]:

$$\frac{\partial \overline{\rho}\widetilde{u}_i}{\partial t} + \frac{\partial \overline{\rho}\widetilde{u}_j\widetilde{u}_i}{\partial x_j} = -\frac{\partial}{\partial x_j}\left(\frac{\mu_{\text{eff}}}{\sigma_{\widetilde{u}}}\frac{\partial \widetilde{u}_i}{\partial x_j}\right) + \overline{\rho}g_i + \overline{\rho}\widetilde{F}_{\text{liq},i} \tag{2.3}$$

In the model, the diffusion terms of the momentum equation have been modelled using a gradient model, where $\frac{\mu_{\text{eff}}}{\sigma_{\widetilde{u}}} = \mu + \frac{\mu_t}{\sigma_{\widetilde{u}}}$, $\mu = \overline{\rho}\nu$. $\widetilde{F}_{\text{liq},i}$ is a Favre averaged source term from the evaporation of the liquid fuel spray. The source term is found in the spray model, Eq. (2.99).

Species mass fraction model

The balance of the species mass fraction is modelled [39] by:

$$\frac{\partial \overline{\rho}\widetilde{Y}_k}{\partial t} + \frac{\partial \overline{\rho}\widetilde{u}_j\widetilde{Y}_k}{\partial x_j} = -\frac{\partial}{\partial x_j}\left(\frac{\mu_{\text{eff}}}{\sigma_{\widetilde{Y}_k}}\frac{\partial \widetilde{Y}_k}{\partial x_j}\right) + \overline{\rho}\widetilde{\dot{R}}_k + \overline{\rho}\widetilde{\dot{R}}_{\text{liq},k} \tag{2.4}$$

In the model, the diffusion terms of the species mass fraction equation have been modelled using a gradient model, where $\frac{\mu_{\text{eff}}}{\sigma_{\widetilde{Y}_k}} = \mu + \frac{\mu_t}{\sigma_{\widetilde{Y}_k}}$, $\mu = \overline{\rho}\nu$. $\widetilde{\dot{R}}_{\text{liq},k}$ is a source term like the one used in the continuity equation model, but only for species k. $\widetilde{\dot{R}}_k$ is the Favre averaged reaction rate from the reactor model Eq. (2.33).

Enthalpy (for incompressible flows) model

The energy balance of the gas phase is modelled [39] by:

$$\frac{\partial \overline{\rho}\widetilde{h}}{\partial t} + \frac{\partial \overline{\rho}\widetilde{u}_j\widetilde{h}}{\partial x_j} = -\frac{\partial}{\partial x_j}\left(\frac{\mu_{\text{eff}}}{\sigma_{\widetilde{h}}}\frac{\partial \widetilde{h}}{\partial x_j}\right) + \widetilde{\dot{Q}}_{gs} + \widetilde{\dot{Q}}_{\text{Rad}} + \overline{\rho}\widetilde{S}_{\text{liq}} \tag{2.5}$$

In the model, the diffusion terms of the enthalpy equation have been modelled using a gradient model, where $\frac{\mu_{\text{eff}}}{\sigma_{\widetilde{h}}} = \mu + \frac{\mu_t}{\sigma_{\widetilde{h}}}$, $\mu = \overline{\rho}\nu$. $\widetilde{\dot{Q}}_{gs}$ is a Favre averaged source term due to heat transfer from the solid phase to the gas phase, and $\widetilde{S}_{\text{liq}}$ is the Favre averaged heat transfer from the liquid spray to the gas phase, found in the spray model Eq. (2.100). $\widetilde{\dot{Q}}_{\text{Rad}}$ is the Favre averaged net radiative heat transfer to the gas phase, found from the Eq. (2.51). The flow is assumed incompressible, meaning, the density is not affected by pressure differences. This assumption can be done because the flow velocity is much lower than the speed of sound, fulfilling the condition:

$$\frac{L}{a_s\hat{\tau}_a} << 1 \tag{2.6}$$

where L and $\hat{\tau}_a$ are a length scale and time over which the fluid velocity undergoes significant changes, and a_s is the speed of sound [20](p.122).

2.1.2 Energy equation for porous solid phase

The equation for heat transfer to solids in the calculation domain, is given [39] by:

$$\frac{\partial(\rho C_p T)}{\partial t} = \frac{\partial}{\partial x_j}(K\frac{\partial T}{\partial x_j}) + \dot{Q}_{\text{reac}} + \dot{Q}_{\text{sg}} + \dot{Q}_{\text{Rad},s} + \dot{Q}_{\text{liq},s} \tag{2.7}$$

where $\dot{Q}_{\text{Rad},s}$ is the net radiative transfer to the solid phase, which can be found from Eq. (2.51), $\dot{Q}_{\text{reac}}$ is a heat source term due to chemical reactions in the medium, and $\dot{Q}_{\text{liq},s}$ is the net energy transfer to the solid phase due to contact with liquid droplets. The energy equation for the porous solid phase and the enthalpy model is linked by:

$$\dot{Q}_{\text{sg}} = -\dot{Q}_{\text{gs}} \tag{2.8}$$

2.2 Turbulence

The influence of turbulence on the simulation is modelled by a Favre averaged $k-\epsilon$ model [18]. The model will calculate the formation and destruction of turbulence energy.

Nonlinear convection processes in the flow lead to the appearance of fluctuating velocities. The average products of these velocities are the Reynolds stresses. The Reynolds stresses are modelled [39] as:

$$-\overline{\rho}\widetilde{u_i' u_j'} = \mu_t(\frac{\partial \widetilde{u}_j}{\partial x_i} + \frac{\partial \widetilde{u}_i}{\partial x_j}) - \frac{2}{3}(\overline{\rho}k + \mu_t\frac{\partial \widetilde{u}_l}{\partial x_l})\delta_{ij} \tag{2.9}$$

where δ_{ij} is the Kronecker-delta function, which is 1 when $i = j$ and 0 when $i \neq j$. k is the turbulent kinetic energy, which is the sum of the normal Reynolds stresses. ϵ is the dissipation of turbulent kinetic energy, which describes the conversion of turbulent kinetic energy to heat. The k-equation used in the simulation is given [39] by:

$$\frac{\partial}{\partial t}(\overline{\rho}k) + \frac{\partial}{\partial x_j}(\overline{\rho}k\widetilde{u}_j) = \frac{\partial}{\partial x_j}(\frac{\mu_{\text{eff}}}{\sigma_k}\frac{\partial k}{\partial x_j}) + \overline{\rho}P_k - \overline{\rho}\epsilon + B \tag{2.10}$$

where $\frac{\partial}{\partial x_j}(\frac{\mu_{\text{eff}}}{\sigma_k}\frac{\partial k}{\partial x_j})$ is a gradient model for the turbulent and viscous diffusion, $\frac{\mu_{\text{eff}}}{\sigma_k} = \mu + \frac{\mu_t}{\sigma_k}$:

$$\frac{\partial}{\partial x_j}(\frac{\mu_{\text{eff}}}{\sigma_k}\frac{\partial k}{\partial x_j}) = \frac{\partial}{\partial x_j}(\overline{\tau_{ij}u_i''} - \frac{1}{2}\rho\overline{u_i''u_i''u_j''} - \overline{p'u_j''}) \tag{2.11}$$

$\overline{\rho}P_k$ is the production of turbulent kinetic energy given by:

$$\overline{\rho}P_k = \mu_t(\frac{\partial \widetilde{u}_j}{\partial x_i} + \frac{\partial \widetilde{u}_i}{\partial x_j})\frac{\partial \widetilde{u}_i}{\partial x_j} - \frac{2}{3}(\overline{\rho}k + \mu_t\frac{\partial \widetilde{u}_l}{\partial x_l})\frac{\partial \widetilde{u}_i}{\partial x_i} \tag{2.12}$$

The turbulence viscosity is given by:

$$\mu_t = \overline{\rho}\nu_t = C_\mu\overline{\rho}\frac{k^2}{\epsilon} \tag{2.13}$$

B is a source term representing buoyancy effects modelled[1] by:

$$B = -\frac{\mu_t}{\sigma_t}\frac{\partial \overline{\rho}}{\partial x_i} g_i \tag{2.14}$$

The ϵ-equation used in the simulation is given [39] by:

$$\frac{\partial}{\partial t}(\overline{\rho}\epsilon) + \frac{\partial}{\partial x_j}(\overline{\rho}\epsilon\widetilde{u}_j) = \frac{\partial}{\partial x_j}(\frac{\mu_{\text{eff}}}{\sigma_\epsilon}\frac{\partial \epsilon}{\partial x_j}) + C_{\epsilon 1}\frac{\epsilon}{k}\overline{\rho}P_k - C_{\epsilon 2}\frac{\epsilon}{k}\overline{\rho}\epsilon + C_{\epsilon 1}C_{\epsilon 3}\frac{\epsilon}{k}B \tag{2.15}$$

The constants in the k–ϵ model is given as in Ertesvåg [7](p.54, after Launder and Spalding [18]): $C_{\epsilon 1}$=1.44, $C_{\epsilon 2}$=1.92, C_μ=0.09, σ_k=1.0 and σ_ϵ=1.3. For the buoyancy model the constants are given by Ertesvåg [7](p. 58, after Rodi [34] and Rodi [35]) : σ_T=0.9 and $C_{\epsilon 3}$=0 for stable stratification. $C_{\epsilon 3}$=0 is chosen because it gives poor mixing in the atmosphere, which represents the worst case scenario. The worst case scenario is an important focus in risk analysis.

2.3 Combustion

The combustion model used in KFX is the Eddy Dissipation Concept (EDC)[23]. A combustion model is needed to model the interaction between turbulence and combustion. For combustion to take place, it is necessary with molecular mixing of reactants. The molecular mixing will be found in the smallest eddies of the turbulence. The EDC combustion model is split up into a cascade model and a reaction model [7].

Cascade model

The cascade model groups the turbulence depending on frequency. Low frequencies are located at the top of the cascade, and high frequencies at the bottom. Every step down in the cascade can be defined by the step above. The top step represents the main flow and the bottom step of the cascade model represents the fine structure. In the fine structure, where the smallest turbulent eddies are located, viscous forces break up the eddies and scatter and mixes the molecules [7]. It is assumed that most of the turbulent dissipation to heat and all the reactions take place in the fine structures. The cascade model allows defining the fine structure as a function of the main flow, where the fine structure states are coupled to the turbulence energy k, and the turbulence dissipation ϵ from the k–ϵ model. From the cascade model, the Reynolds number and the characteristic velocity- and length scale for the fine structure can be defined [7] as:

$$\text{Re}^* = \frac{u^* L^*}{\nu} = \frac{2C_{D2}}{3C_{D1}} \tag{2.16}$$

[1] The equation for buoyancy is given as programmed in the simulation software KFX. Although the equation is dimensionally incorrect, it is the equation used in the simulation. The effect of B is discussed in Sec. (5.1).

$$L^* = \frac{2}{3}(\frac{3C_{D2}^3}{C_{D1}^2})^{1/4}(\frac{\nu^3}{\epsilon})^{1/4} \tag{2.17}$$

$$u^* = (\frac{C_{D2}}{3C_{D1}^2})^{1/4}(\nu\epsilon)^{1/4} \tag{2.18}$$

The constants C_{D1}=0.134 and C_{D2}=0.50 are as given by Magnussen [22].

For reactions to take place, the reactants must be mixed in the correct composition for a long enough time [7]. The residence time in the fine structure is described by a fine structure time scale. The fine structure time scale is a characteristic time scale for the molecular mixing of reactants, products and heat, and is given [39] by:

$$\tau^* = 0.41\sqrt{\frac{\nu}{\epsilon}} \tag{2.19}$$

The fine structure will form between the bigger eddies, giving volumes with much fine structure and volumes with little fine structure. The fine structures are contained inside fine structure regions, both occupying a fraction of the total volume. The mass ratio of fine structure on total mass is given[2] [39] by:

$$\gamma^* = 9.7(\frac{\nu\epsilon}{k^2})^{3/4} \tag{2.20}$$

where the mass ratio of fine structure regions on total mass is given by:

$$\gamma_\lambda = (\gamma^*)^{1/3} \tag{2.21}$$

The part of the fine structure that is reacting is given[3] by[39]:

$$\chi = \frac{\widetilde{Y}_{\mathrm{Pr}}}{(\widetilde{Y}_{\mathrm{Pr}} + (1 + r_{\mathrm{s,fu}})\widetilde{Y}_{\mathrm{max}}) \cdot \gamma_\lambda} \tag{2.22}$$

where

$$\widetilde{Y}_{\mathrm{max}} = \max(\widetilde{Y}_{\mathrm{fu}}, \frac{\widetilde{Y}_{\mathrm{O_2}}}{r_{\mathrm{s,fu}}}) \tag{2.23}$$

$\widetilde{Y}_{\mathrm{Pr}}$ is the species mass fraction of products, $\widetilde{Y}_{\mathrm{O_2}}$ is the species mass fraction of oxygen, $\widetilde{Y}_{\mathrm{fu}}$ is the species mass fraction of fuel and $r_{\mathrm{s,fu}}$ is the stoichiometric oxygen requirement on mass basis [7] for the reaction(s):

$$\mathrm{Fuel} + r_{\mathrm{s,fu}}\mathrm{Air} \rightarrow (1 + r_{\mathrm{s,fu}})\mathrm{Products} \tag{2.24}$$

A fine structure mixing rate coefficient, η, is given [39] by:

[2]The equation has been revised in Magnussen [24], but Eq. 2.20 is the equation used in the simulation.

[3]This is the equation used in the simulation although it is slightly different from the one presented in Magnussen [23]. The model choice is discussed in Sec. (5.1)

$$\eta = \min(\frac{1}{\gamma_\lambda}, \frac{\widetilde{Y}_{Pr}/(1+r_{s,fu}) + \widetilde{Y}_{min}}{\widetilde{Y}_{min}}) \tag{2.25}$$

where

$$\widetilde{Y}_{min} = \min(\widetilde{Y}_{fu}, \frac{\widetilde{Y}_{O_2}}{r_{s,fu}}) \tag{2.26}$$

Reactor model

The fine structure is seen as a well-mixed homogeneous reactor, where the reaction zones are modelled as perfectly stirred. The reactors receive gas from the fine structure surroundings, which are mixed into the reactors. The flow into the reactors will have properties of the fine structure surroundings and the gas leaving the reactors will have properties of the fine structure. Thus, for a fine structure reactor, a species balance and an enthalpy balance can be given [39] by:

$$(\frac{dY_k^*}{dt}) + \frac{1}{\tau^*}(Y_k^* - Y_k^0) = \dot{R}_k^* \tag{2.27}$$

$$(\frac{dh^*}{dt}) + \frac{1}{\tau^*}(h^* - h^0) = (\frac{1}{\rho^*} \cdot \frac{dp}{dt}) \tag{2.28}$$

where superscript * correspond to the fine structure, ^{0} corresponds to the surroundings. $\dot{R}_k^*$ is the reaction rate in the burning fine structures on mass basis. Y_k is the species mass fraction, h is enthalpy.

For an adiabatic reactor, the energy going into the reactor must equal the energy leaving the reactor. Given constant mass flow through the reactor [7](p.185):

$$h^0 = h^* \tag{2.29}$$

h^0 can be found from the enthalpy field.

For a mixture at constant pressure, h^* can be given by:

$$h^* = C_p(T^* - T_{ref}) + Y_{fu}^* H_R \tag{2.30}$$

where H_R is the calorific value of the fuel and T_{ref} is a chosen reference temperature.

h^0 can be given by:

$$h^0 = C_p(T^0 - T_{ref}) + Y_{fu}^0 H_R \tag{2.31}$$

By rearranging the enthalpy balance, the temperature of the fine structure is given by:

$$T^* = \frac{H_R}{C_p}(Y_{fu}^0 - Y_{fu}^*) + T^0 \tag{2.32}$$

The density weighted average reaction rate is given [39] as (assuming all reactions take place in the fine structure):

$$\widetilde{\dot{R}}_k = \gamma^* \chi \eta \dot{R}_k^* \tag{2.33}$$

The density weighted average enthalpy is given by:

$$\widetilde{h} = \gamma^* \chi\eta h^* + (1 - \gamma^* \chi\eta) h^0 \tag{2.34}$$

The density weighted average temperature is given by:

$$\widetilde{T} = \gamma^* \chi\eta T^* + (1 - \gamma^* \chi\eta) T^0 \tag{2.35}$$

The density weighted average mass fraction is given by:

$$\widetilde{Y}_k = \gamma^* \chi\eta Y_k^* + (1 - \gamma^* \chi\eta) Y_k^0 \tag{2.36}$$

In the simulations conducted in this thesis, the reactions are viewed as infinitely fast and irreversible. Thus, the amount of fuel reacted is limited by the availability of fuel and air. Using the density weighted average mass fraction in Eq. (2.36) and the derivation seen in [7](p.182-184), the reaction rate for the fuel is given [39] by:

$$\dot{R}_{\text{fu}}^* = -\frac{1}{\tau^*(1 - \gamma^* \chi\eta)} \widetilde{Y}_{\text{min}} \tag{2.37}$$

and the density weighted average reaction rate is given by:

$$\widetilde{\dot{R}}_{\text{fu}} = -\frac{\gamma^* \chi\eta}{\tau^*(1 - \gamma^* \chi\eta)} \widetilde{Y}_{\text{min}} \tag{2.38}$$

The fine structure temperature can be found [7](p.186) through:

$$T^* = \frac{H_R}{C_p} \widetilde{Y}_{\text{min}} + \widetilde{T} \tag{2.39}$$

2.4 Soot

Soot can affect the radiative heat transfer by absorbing and emitting radiation. Consequently, for precise calculation of the radiative heat exchange in fires, a soot model that takes into account soot formation and combustion is of importance. In the simulation the soot model is decoupled from the system of energy and species mass fractions. The soot model used is the Eddy Dissipation Soot Model [25]. The model takes into account formation and combustion of soot and nucleus through species balances. The nuclei are the smallest particles, which set on the soot formation. Production and the movements of nuclei is therefore important for modelling of soot. The soot and nucleus balances are given [39] by:

Nucleus balance

$$\frac{dY_{\text{nuc}}^*}{dt} + \frac{1}{\hat{\tau}}(Y_{\text{nuc}}^* - \widetilde{Y}_{\text{nuc}}) = \frac{n_0^*}{\rho^*} + (f - g) Y_{\text{nuc}}^* - \frac{g_0 \cdot a}{b} Y_{\text{nuc}}^* \frac{Y_{\text{soot}}^*}{Y_{\text{soot,max,3}}} - \frac{1}{\hat{\tau}} \frac{Y_{\text{min}}}{\widetilde{Y}_{\text{fu}}} \widetilde{Y}_{\text{nuc}} \tag{2.40}$$

Soot balance

$$\frac{dY^*_{soot}}{dt} + \frac{1}{\hat{\tau}}(Y^*_{soot} - \widetilde{Y}_{soot}) = \rho b \cdot Y_{soot,max,1} \cdot Y^*_{nuc}(1 - \frac{Y^*_{soot}}{Y_{soot,max,2}}) - \frac{1}{\hat{\tau}}\frac{Y_{min}}{\widetilde{Y}_{fu}}\widetilde{Y}_{soot} \tag{2.41}$$

where

$$Y_{soot,max,1} = Y_{soot,max,2} = Y_{soot,max,3} = \frac{a \cdot m_p}{b\rho} \tag{2.42}$$

$$\frac{1}{\hat{\tau}} = \frac{\dot{m}^*}{1 - \gamma^* \chi \eta} \tag{2.43}$$

$$\tau^* = \frac{1}{\dot{m}^*} \tag{2.44}$$

and $a = 10^5$ [(part.,soot)/(part.,nuc s)], $b = 8.0 \cdot 10^{-14}$ [m^3/(part.,nuc s)], n is amount of soot nucleus per m^3, $f - g = 100$, $g_0 = 10^{-15}$ [m^3/(part.,soot s)] and m_p is the mass of the soot particle.

Limiting values for the fine structure are given [39] by:

$$Y^*_{soot} = Y_{soot,max,2} \tag{2.45}$$

$$Y^*_{nuc} = \frac{\frac{n^*_0}{\rho^*} + \frac{1}{\hat{\tau}}\widetilde{Y}_{nuc}}{\frac{1}{\hat{\tau}} + \frac{g_0 \cdot a}{b}\frac{Y_{soot,max,2}}{Y_{soot,max,3}} - (f - g)} \tag{2.46}$$

and limiting values for the fine structure surroundings are given [39] by:

$$Y^0_{soot,max} = 0.08 \cdot Y_{soot,max,3} \tag{2.47}$$

$$Y^0_{nuc,max} = \frac{51.39 \cdot 10^{12}}{\rho} \tag{2.48}$$

In the combustion model, it is assumed that the soot and the nucleus combustion are proportional to the fuel combustion.

2.5 Radiation

In the simulation, an enhanced version of the Discrete Transfer Model by Shah and Lockwood [21] is used. Grey gas is assumed, giving the absorption coefficient to be approximately constant over all wavelengths. The enclosure, inside the calculation domain, is divided into a finite number of elements. A prescribed number of radiation beams are fired from each element at one boundary, and numerical integration is carried out along each beam until it reaches another boundary. As the beam passes through a control volume, the changes in radiation intensity due to absorption and emission are calculated.

The change of intensity for one beam, passing through a control volume is given [39] by:

$$I_{n+1} = \frac{\sigma \widetilde{T}^4}{\pi}(1 - e^{-as}) + I_n e^{-as} \tag{2.49}$$

where I is the radiation intensity, n describes the placement of the control volume in the domain, σ is the Stefan-Boltzmann constant, $\widetilde{T}$ is the density averaged temperature (found from the EDC reactor model Eq. (2.35)), a is the absorption coefficient and s is the coordinate along the radiation path.

The contribution from one beam, passing through a control volume, is given [39] by:

$$S_{n,i} = (I_{n+1} - I_n)\Omega dA d\Omega \tag{2.50}$$

where dA is the area element at the origin boundary and Ω is the solid angle represented by the beam.

The total radiation source for the nth control volume is given by summing over all the beams passing through the control volume[39]:

$$\dot{Q}_{\text{Rad}} \cdot dV = S_n = \sum_{i=1}^{j} S_{n,i} \tag{2.51}$$

where j is the total number of beams. The net gain or loss of radiation energy in a control volume is appended to the energy conservation equation, where $\dot{Q}_{\text{Rad}}$ can be used for the source term in the Eqs. (2.5) and (2.7).

The absorption coefficient is calculated through a relation with emissivity, $\hat{\epsilon}$[39]:

$$a = -\frac{1}{s} ln(1 - \hat{\epsilon}) \tag{2.52}$$

where s is a characteristic length for the gas volume, $\hat{\epsilon}$ is the total emissivity coefficient. The total emissivity coefficient is further calculated from the emissivities of gas and soot:

$$\hat{\epsilon} = \hat{\epsilon}_{\text{soot}} + \hat{\epsilon}_g - \hat{\epsilon}_{\text{soot}}\hat{\epsilon}_g \tag{2.53}$$

$\hat{\epsilon}_{\text{soot}}$ is the spectral integrated emissivity of soot, $\hat{\epsilon}_g$ is the gas emissivity. $\hat{\epsilon}_{\text{soot}}\hat{\epsilon}_g$ is an overlap correction. The emissivity of a gas is dependant on the state of the gas and how thick the gas volume is. The emissivity of soot is calculated from Vembe et al. [39], after Felske and Tien [9]:

$$\hat{\epsilon}_{\text{soot}} = 1 - \frac{15}{\pi^4}\phi^{(3)}(1 + \frac{k_0 \rho Y_{\text{soot}} \widetilde{T} s}{\rho_{\text{soot}} C_2}) \tag{2.54}$$

where $\phi^{(3)}$ is the penta-gamma function, $k_0 = 7.0$, $C_2 = 0.01439\,\text{mK}$ and ρ_{soot} is the specific density of soot.

The gas emissivity $\hat{\epsilon}_g$ is from Vembe et al. [39], after Leckner [19]:

$$\hat{\epsilon}_g = \hat{\epsilon}_{CO_2} + \hat{\epsilon}_{H_2O} - \Delta\hat{\epsilon}_{ov} \tag{2.55}$$

where the emissivity for a given gas component, $\hat{\epsilon}_k$, is given by:

$$\hat{\epsilon}_k = \hat{\epsilon}_0(1 + (\frac{A_c \cdot p_E + B_c}{p_E + A_c + B_c - 1} - 1) \cdot (\exp(-\kappa(\zeta_{\max} - \zeta)^2))) \tag{2.56}$$

$$\log\hat{\epsilon}_0 = \sum_{i=0}^{M} b_i \zeta^i \tag{2.57}$$

$$b_i = \sum_{j=0}^{N} c_{ji} \tau_{\hat{\epsilon}}^j \tag{2.58}$$

$$\tau_{\hat{\epsilon}} = \frac{\widetilde{T}}{1000} \tag{2.59}$$

$$\zeta = \log(p_{\text{gas}} \cdot \hat{s} \cdot 100) \tag{2.60}$$

where p_{gas} is the partial pressure of the gas component and $\hat{s}$ is the mean path length. Subscripts and potencies i and j are taken from Tables. (2.1) and (2.2)

For CO_2 the constants are given as:

$$p_E = p(1 + 0.28\frac{p_{CO_2}}{p}) \tag{2.61}$$

p is total pressure.

$$\zeta_{\max} = \log(0.225\tau_{\hat{\epsilon}}^2) \tag{2.62}$$

$A_c = 0.10\tau_{\hat{\epsilon}}^{-1.45} + 1.0$, $B_c = 0.23$, $\kappa = 1.47$.

The values for c_{ji} used in the emissivity model for CO_2 is for values of $\widetilde{T} > 400K$, M=3 and N=4, given in Table (2.1).

Table 2.1: CO_2 emissivity constants

$c_{j,i}$	j=0	j=1	j=2	j=3	j=4
i=0	-3.9781	2.7353	-1.9882	0.31054	0.015719
i=1	1.9326	-3.5932	3.7247	-1.4535	0.20132
i=2	-0.35366	0.61766	-0.84207	0.39859	-0.063356
i=3	-0.080181	0.31466	-0.19973	0.046532	-0.0033086

For H_2O the constants are given as:

$$p_E = p(1 + 4.9\frac{p_{H_2O}}{p}\sqrt{273/\widetilde{T}}) \tag{2.63}$$

$$\zeta_{\max} = \log(13.2\tau_{\hat{\epsilon}}^2) \tag{2.64}$$

$A_c = 1.888 - 2.053\log\tau_{\hat{\epsilon}}$, $B_c = 1.1\tau_{\hat{\epsilon}}^{-1.4}$, $\kappa = 0.5$.

The values for c_{ji} used in the emissivity model for H_2O is for values of $\widetilde{T} > 400K$, M=2 and N=2 given in Table (2.2).

Table 2.2: H_2O emissivity constants

$c_{j,i}$	j=0	j=1	j=2
i=0	-2.2118	-1.1987	0.035596
i=1	0.85667	0.93048	-0.14391
i=2	-0.10838	-0.17156	0.045915

The correction term is calculated by:

$$\Delta\hat{\epsilon}_{ov} = (\frac{\beta}{10.7 + 101\beta} - 0.0089\beta^{10.4})\zeta_{ov}^{2.76} \tag{2.65}$$

$$\beta = \frac{p_{H_2O}}{p_{H_2O} + p_{CO_2}} \tag{2.66}$$

$$\zeta_{ov} = \log((p_{H_2O} + p_{CO_2}) \cdot \hat{s} \cdot 100) \tag{2.67}$$

To improve efficiency of the radiation model, KFX uses random distributions of rays. For the modelled enclosure walls, a radiation focus is done. This is done to precisely calculate the radiation related to the walls. Every cell on the surface of the enclosure acts as a starting point for radiation beams. This way, every wall point is hit by radiation giving representative energy balances for the wall cells.

The radiation energy leaving a surface is given [39] by:

$$q_{\text{rad,out}} = a\sigma T_{\text{surface}}^4 \tag{2.68}$$

a is the absorption coefficient. σ is the Stefan-Boltzmann constant, which is given to be $5.670 \cdot 10^{-8}$ W/m^{2}K^4. For points in the calculation domain where the temperature is above 800 K, a ray trace box is created. From every node on the ray trace box, a number of 96 rays are traced. A relaxation factor of 0.3 is used to smooth out radiation heat flux on all solid surfaces [39].

2.6 The log-law

For calculations of shear stress, heat flux and mass flux from a fluid to a solid wall, KFX uses the logarithmic law of the wall (log-law). The assumption is that close to a solid wall, the turbulent boundary layer is seen as laminar. The log-law is derived for boundary layers without pressure gradients, without mass flow through the walls and along smooth walls.

The log law velocity profile is given [39] by:

$$U^+ = \frac{1}{\hat{\kappa}} \ln(E \cdot y^+) \tag{2.69}$$

$\hat{\kappa}$ and E are constants, U^+ and y^+ are dimensionless velocity and distance from the wall and is given by:

$$U^+ = \frac{u_f}{U^*} \tag{2.70}$$

$$y^+ = \frac{y_f U^*}{\nu_f} \tag{2.71}$$

where u_f is the velocity parallel to the wall in the cell centre next to the wall, y_f is the distance to the wall from the cell centre next to the wall, ν_f is the kinematic viscosity in the cell centre next to the wall. U^* is the frictional velocity and is given by:

$$U^* = \sqrt{\frac{\tau_{\text{sur}}}{\rho_f}} \tag{2.72}$$

where ρ_f is the density at the cell centre next to the wall and τ_{sur} is the shear stress at the wall.

The log-law temperature profile is given [39] by:

$$T^+ = \sigma_T (\frac{1}{\hat{\kappa}} \ln(E \cdot y^+) + P^+) \tag{2.73}$$

where T^+ is a dimensionless temperature, σ_T is the turbulent Prandtl number, P^+ is given by:

$$P^+ = 9.0[(\frac{\sigma_l}{\sigma_T})^{0.75} - 1][1 + 0.28e^{-0.007\frac{\sigma_l}{\sigma_T}}] \tag{2.74}$$

where σ_l is the molecular Prandtl number, and T^+ is given by:

$$T^+ = \frac{\rho_f C_p U^* (T_f - T_{\text{sur}})}{q_{\text{sur}}} \tag{2.75}$$

where C_p is heat capacity, T_f is the temperature at the cell centre next to the wall, T_{sur} is the wall temperature and q_{sur} is the heat flux into the wall.

Through Newton iteration of Eq. (2.70) y^+ is found, and the following variables are calculated [39]:

Frictional velocity:

$$U^* = \frac{\nu_f \cdot y^+}{y_f} \tag{2.76}$$

Turbulent kinetic energy:

$$k_f = \frac{U^{*2}}{\sqrt{C_\mu}} \tag{2.77}$$

Dissipation of turbulent kinetic energy:

$$\epsilon_f = \frac{U^{*3}}{\kappa \cdot y_f} \tag{2.78}$$

Wall shear-stress:

$$\tau_{\text{sur}} = \rho_f U^{*2} \tag{2.79}$$

Momentum diffusion coefficient:

$$H_m = \frac{\hat{\kappa} \cdot \rho_f U^*}{\ln(E \cdot y^+)} \tag{2.80}$$

Enthalpy diffusion coefficient:

$$H_h = \frac{\rho_f U^*}{\sigma_T(\frac{1}{\hat{\kappa}}\ln(E \cdot y^+) + P^+)} \tag{2.81}$$

In the laminar sub-layer, if y^+ is lower than $y^+_{edge} = 10.5$, the following relations are used:

$$y^+ = \sqrt{\frac{u_f y_f}{\nu_f}} \tag{2.82}$$

$$U^* = \frac{u_f}{y^+} \tag{2.83}$$

$$k_f = \sqrt{C_\mu} U^{*2} (\frac{u_f}{U^* y^+_{edge}})^2 \tag{2.84}$$

$$\epsilon_f = \frac{U^{*4}}{\hat{\kappa} \cdot \nu_f y^+_{edge}} \tag{2.85}$$

$$H_m = \frac{\rho_f \nu_f}{y_f} \tag{2.86}$$

$$H_h = \frac{\rho_f \nu_f}{\sigma_l y_f} \tag{2.87}$$

In KFX, the transport equations for k and ϵ are not solved at grid nodes adjacent to solids. Instead the values for k_f and ϵ_f, obtained from the log law model, are used [39].

2.7 Spray and Droplet modeling

For the simulation, the liquid spray is treated separately from the gas flow. A spray is viewed as a collection of individual droplets. To prevent simulating every droplet individually, KFX uses a number of discrete numerical droplets, that represent a given amount of real droplets. It is assumed that the droplet is spherical and of pure liquid.

Trajectory model

The liquid droplets trajectory is modelled [39] by:

$$\frac{d\vec{x}_d}{dt} = \vec{v}_d \tag{2.88}$$

Here $\vec{x}_d$ is the position vector of the droplet, while $\vec{v}_d$ is the velocity vector of the droplet.

Mass model

The liquid droplets will increase or decrease in size due to diffusion, where evaporated fuel vapour at the surface of the droplet diffuses towards the environment. This is governed by a mass model[39]:

$$\frac{dr_d}{dt} = \frac{\rho D_g(\overline{T})}{2\rho_l} \frac{Y_l^* - Y_l}{1 - Y_l} Sh_d \tag{2.89}$$

where r_d is the droplet radius, $D_g(\overline{T})$ is the diffusivity of the gas phase, Y_l^* is the mass fraction of the fuel vapour at the surface of the droplet. Sh_d is the Sherwood number, given by:

$$Sh_d = (2 + 0.6 Re_d^{1/2} Sc_d^{1/3}) \frac{\ln(1 + B_d)}{B_d} \tag{2.90}$$

where the Schmidt number, $Sc_d = \frac{\mu_g(\overline{T})}{\rho_g D_g(\overline{T})}$. $\mu_g(\overline{T})$ and ρ_g are the dynamic viscosity and density respectively of the gas phase. The transfer number $B_d = \frac{Y_l^* - Y_l}{1 - Y_l^*}$. The fuel vapour mass fraction Y_l^* is given by:

$$Y_l^* = \frac{\mathrm{MW}_l}{\mathrm{MW}_l + \mathrm{MW}_0 (\frac{p}{p_v(T_d)} - 1)} \tag{2.91}$$

where MW_1 is the molecular weight of the fuel species, MW_0 is the molecular weight of all species except the fuel species and p_v is the equilibrium vapour pressure at the temperature T_d.

Momentum model

As a droplet travels along its trajectory, the momentum of the droplets can change. This variation of the momentum of a droplet is governed by a momentum model[39]:

$$\frac{d\vec{v}_d}{dt} = C_D \frac{3}{8} \frac{\rho_g}{\rho_l} \frac{|\vec{u}_g - \vec{v}_d|}{r_d} (\vec{u}_g - \vec{v}_d) + \vec{g} \tag{2.92}$$

Here $\vec{u}_g$ is the velocity of the surrounding gas and $\vec{v}_d$ is the velocity of the droplets. The drag coefficient C_D is given by:

$$C_D = \begin{cases} \frac{24}{Re_d}(1 + \frac{1}{6} Re_d^{2/3}) & \text{for} Re_d < 1000 \\ 0.424 & \text{for} Re_d \geq 1000 \end{cases} \tag{2.93}$$

The Reynolds number Re_d is given by:

$$Re_d = \frac{2\rho|\vec{u}_d - \vec{v}_d|r_d}{\mu_g(\overline{T})} \tag{2.94}$$

$\overline{T}$ is the average surface layer temperature given by: $\overline{T} = \frac{T_g + 2T_d}{3}$.

Energy model

As the droplets are heated, evaporation can occur. The energy balance of the droplets is modelled [39] as:

$$\frac{dT_d}{dt} = \frac{4\pi r_d^2(\dot{Q}_d + \rho_l \dot{r}_d L_h(T_d))}{\rho_l \frac{4}{3}\pi r^3 C_{p,l}} \tag{2.95}$$

where $\dot{Q}_d$ is the rate of heat conducted into the droplet per unit area, given by:

$$\dot{Q}_d = \frac{K_g(\overline{T})(T - T_d)}{2r_d} Nu_d \tag{2.96}$$

$L_h(T_d)$ is the latent heat of evaporation for the droplet at the temperature T_d, $C_{p,l}$ is the heat capacity of the liquid fuel, $\dot{r}_d$ is the change in radius of the droplet. The Nusselt number is given by:

$$Nu_d = (2 + 0.6Re_d^{1/2}Pr_d^{1/3})\frac{\ln(1 + B_d)}{B_d} \tag{2.97}$$

where Pr_d is the Prandtl number given by: $Pr_d = \frac{\mu_g(\overline{T})C_{p,g}(\overline{T})}{K_g(\overline{T})}$, K_g is the thermal conductivity of the gas phase, $L(T_d)$ is the latent heat of evaporation for the droplet at temperature T_d, $C_{p,g}$ is the specific heat at constant pressure for the gas phase and $C_{p,l}$ is the heat capacity of the liquid fuel.

When the droplets are modelled, it is assumed that the volume fraction that the droplets occupies is negligible compared to the total gas volume. Seen from the gas phase, the droplets acts as a source of mass/species, momentum and energy. The evaporation of the liquid droplets act as a source of vapour, that can be used for combustion. Seen from the liquid phase, the gas interacts with the droplets by moving them around and make them evaporate and lose their mass.

The evaporated droplets source contribution to the gas phase equations, summed over all the simulated droplets in the cell volume for one time step, is modelled [39] by:

Conservation of mass, source term

$$\dot{R}_{\text{liq}} = \frac{4\pi\rho_l}{\rho_g \Delta V \Delta t} \sum_{n=1}^{N_s} \xi_n (r_{d,n,o}^3 - r_{d,n}^3) \tag{2.98}$$

Conservation of momentum, source term

$$F_{\text{liq,i}} = \frac{4\pi\rho_l}{\rho_g \Delta V \Delta t} \sum_{n=1}^{N_s} \xi_n (u_{i,n,o} r_{n,o}^3 - u_{i,n} r_n^3) \tag{2.99}$$

Conservation of energy, source term

$$S_{\text{liq}} = \frac{4\pi\rho_l}{\rho_g \Delta V \Delta t} \sum_{n=1}^{N_s} \xi_n (h_{n,o} r_{n,o}^3 - h_n r_n^3) \tag{2.100}$$

The subscript $_o$ refers to the state of the drop before the current time step, Δt. ΔV is the cell volume. The number of droplets represented by each simulated droplet is given by:

$$\xi = \frac{N_p}{N_s} \tag{2.101}$$

where N_s is the number of simulated droplets and N_p, the number of physical droplets, is given by:

$$N_p = \frac{\int_0^{t_{\text{inj}}} \dot{M}_{\text{inj}} dt}{\frac{4}{3}\pi r_{\text{inj}}^3 \rho_l} \tag{2.102}$$

2.7.1 Initial and Boundary conditions

Initial properties of the droplets like position vector, velocity vector, size and temperature needs to be specified initially. At the time of generation, for each simulated droplet, the droplets position vector, velocity vector, size and temperature must be specified. If a droplet impinges on a solid surface, the droplet will either be evaporated, if the surface temperature is above 100°C, or be terminated, if the surface temperature is below 100°C. Heat for evaporation of the droplets are provided from the surface. If the droplet diameter is below 10μm, the droplet goes to gas phase.

2.8 Numerical solution and calculation domain

The numerical method used in the simulations is a cartesian Finite Volume Method (FVM). The transient behaviour is modelled with the backward Euler scheme. A finite number of points, surrounded by control volumes, are distributed throughout the calculation domain. The combined control volumes constitute a numerical staggered grid. Scalar variables and thermo- and fluid dynamical properties like density, heat capacity and conductivity are stored at the cell centres, and vector variables like velocities are stored at the cells boundaries. In KFX, two choices of cell types are available for modelling of solid constructions: Solid cells and thin walled cells. The transient temperature profile through the walls, is calculated by a one dimensional explicit finite difference technique. When 3D CAD models are imported into KFX, a simulation model and computational grid are generated. Also as part of the import process, a porosity file with model properties is generated. This file is used by KFX for

calculations [39].

Solid cell

A solid cell is built up as seen in Fig. (2.1), with a solid core and no flow allowed to move through the cell. Solid properties like density, heat capacity and heat conductivity, valid for the entire cell, are stored at the cell centre. These values can be used for calculation of heat transfer through the cell. The cell core has a uniform temperature. Heat can be transferred through all sides of the cell, giving three dimensional heat transfer. For calculation of heat transfer through to the core of the cell, and for finding surface temperatures of the solid cell, a shell can be specified around the core of the cell. The shell is given a specified thickness (dw), and the same properties of density, heat capacity and heat conductivity as are applied for the core. This allows heat transfer to be calculated across the shell, and surface temperatures can be found. Two types of solid cells can be specified: isothermal, where the temperature at the core of the cell is constant in time, and temperature solved, where the temperature in the core varies and are calculated from heat exchange [39].

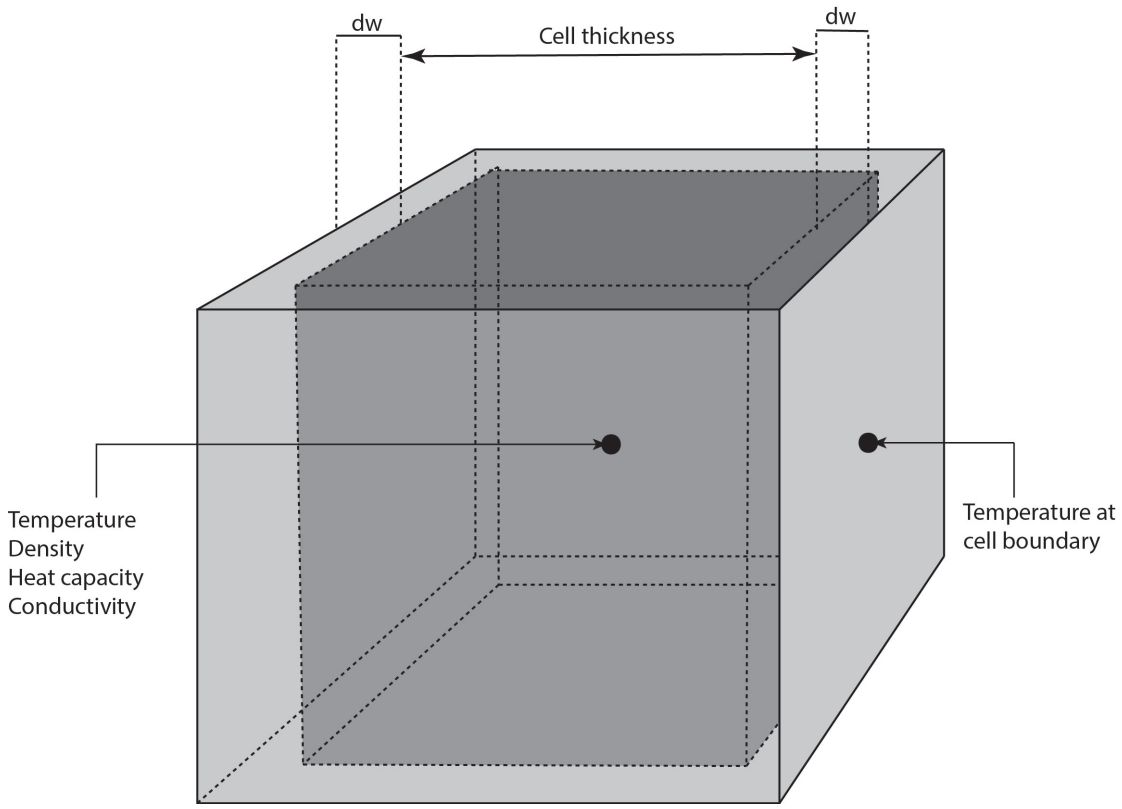

Figure 2.1: Solid cell

Thin walled cell

An alternative solution for modelling of the solid enclosure is to use porosities. The cells are defined as free flow cells, where any flow can move freely through the cell. As for the solid

cell, solid properties of density, heat conductivity and heat capacity, valid for any solid part of the cell, are stored at the cell centre. Given the staggered grid, porosities can be assigned to the cell boundaries in positive coordinate directions. This porosity, limits the amount of flow that can move through the cell boundary. By setting the porosity to 0, a solid cell boundary is obtained. The properties of the solid boundaries are given by the properties stored at the cell centre. By assigning a boundary thickness, one dimensional heat transfer can be calculated through the cell boundary, simulating a thin wall. Modelling of a thin walled cell makes it possible to simulate walls thinner than the cell width without blocking the entire cell. On the basis of the wall properties and solving one dimensional heat balance equations to find convective heat transfer, a transient surface temperature can be calculated [39]. Illustration of the thin walled cell is given in Fig. (2.2).

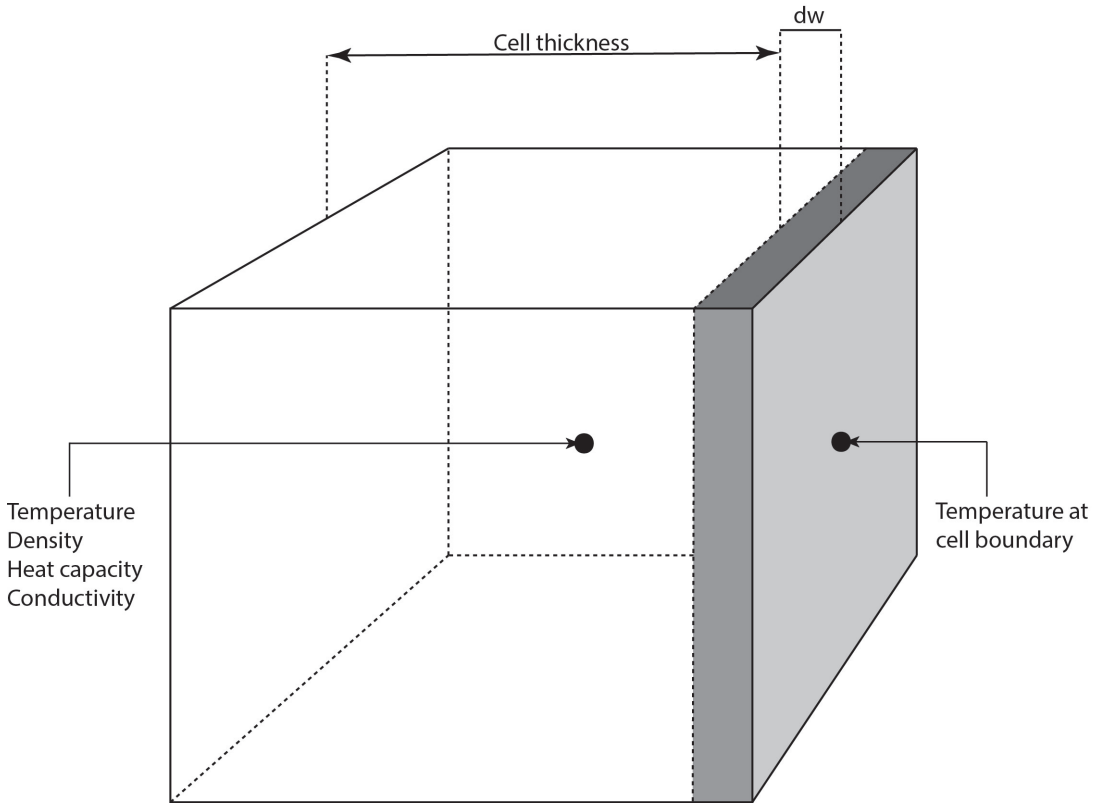

Figure 2.2: Thin walled cell

Numerical calculation

The equations needed for the calculation, are discretized by an integration over the control volumes [39]. By substituting to finite difference type approximations, the integral equations are transformed to a system of coupled algebraic equations. The equations are solved by an iterative method [41]. The solver used in the simulation is the SIMPLEC algorithm. The SIMPLEC algorithm uses the same solution chart as the SIMPLE algorithm [39]. The solution chart used is described by Gran [13]:

1. Guess initial conditions for all variables.

2. Update the boundary conditions.
3. Solve the momentum equations.
4. Solve the pressure-correction equation.
5. Correct the pressure, mass flow rate and Cartesian velocity components.
6. Solve the k equation.
7. Solve the ϵ equation.
8. Solve the other scalar equations.
9. Calculate the temperature, density and viscosity.
10. Use the new values as initial condition, and repeat steps 2 to 10 until convergence is reached.

The solver used for pressure correction and pressure in the simulations, are Stone Strongly Implicit. The maximum number of iterations for pressure correction and pressure equations are chosen to be 100, while the maximum number for all other equations are chosen to be 4. The solver used for transport equations including momentum is Quadratic Tridiagonal Matrix Algorithm (QTDMA). When the calculation converges, the next time step is initiated [41]. The calculation converges if the equation solver convergence criterion is met and a new time step is initiated. The equation solver convergence criterion describes the ratio between ingoing and outgoing residual, and is chosen to be 0.0001 [39]. The same numerical algorithm, solvers and convergence criterion are used for all simulations in this thesis.

The Courant number is defined [37] as:

$$\mathrm{Co} = a_m \frac{\Delta t}{\Delta x} \tag{2.103}$$

where a_m [m/s] is the magnitude of the velocity, Δt [s] is the time step and Δx [m] is the length interval. The Courant number can be thought of as a value in numerical simulation that describes how far a particle in a flow are allowed to travel per time step. If the Courant number is too large, the calculation will lose track of particles and their motion. This could lead to instabilities.

Numerical Solution of the spray equations

The "Lsode" method is used as solution algorithms for the spray equations. The time step of the droplets is based on the gas phase time step, but to ensure a proper interaction with the gas phase, the droplet time step will be sub-cycled. This is done to prevent the droplet from moving beyond the centre of neighbour cells in one (sub)time step. When a full gas time step is reached, the droplet (sub)time stepping ends [39].

Chapter 3

Method

The numerical simulations carried out in this thesis were done in Kameleon FireEx (KFX). A selection of cases was created to investigate the effect of various parameters on fire development inside a compartment. First, a base case was created. This case was made based on the fire test JF5, given in Sec. (1.2.3). The base case will hereafter be called: "The advanced geometry case (base case)". Second, a selection of cases was created, where parameters were adjusted to investigate the effects of geometry import, geometry cell types, single-component or multi-component spray dispersion, fuel flow rate, droplet size, dispersion angle, insulation, size of ventilation opening and Courant number.

3.1 Setup of the base case: The advanced geometry case

3.1.1 Numerical solution and calculation domain

A calculation domain of approximately 617 000 control volumes was created. The grid was mostly uniform with quadratic cells of 0.2 m length. With exception of the lower z-direction boundary, a gradual increase in the cell volumes, as moving towards the domain boundaries, was specified. A modelled enclosure was placed inside the part of the calculation domain, where the cell volumes were uniform. The geometry of the modelled enclosure is shown in Fig. (3.1). One horizontal and one vertical structure, in the form of cylinders, were present inside the enclosure.

The modelled enclosure was created in Doozer, which is a built-in three-dimensional CAD drawing tool in KFX [40]. In the current work, Doozer has been used to make a model based on the enclosure used in test JF5, given in Drangsholt et al. [6]. The model was designed in Doozer with wall thickness and wall properties comparable to JF5. The walls and ceiling of the enclosure in JF5 were insulated with Kaowool Pyro-bloc modular insulation with a stainless steel lining on the side of the wall exposed to the flame [6]. In the geometry designed in Doozer, the materials of the walls, structures and ceiling were simplified to a single material with properties calculated as average values of the materials used in JF5. The wall thickness (Δx_{tot}) was 0.151 m. Initial temperature of the walls were 293 K, identical to

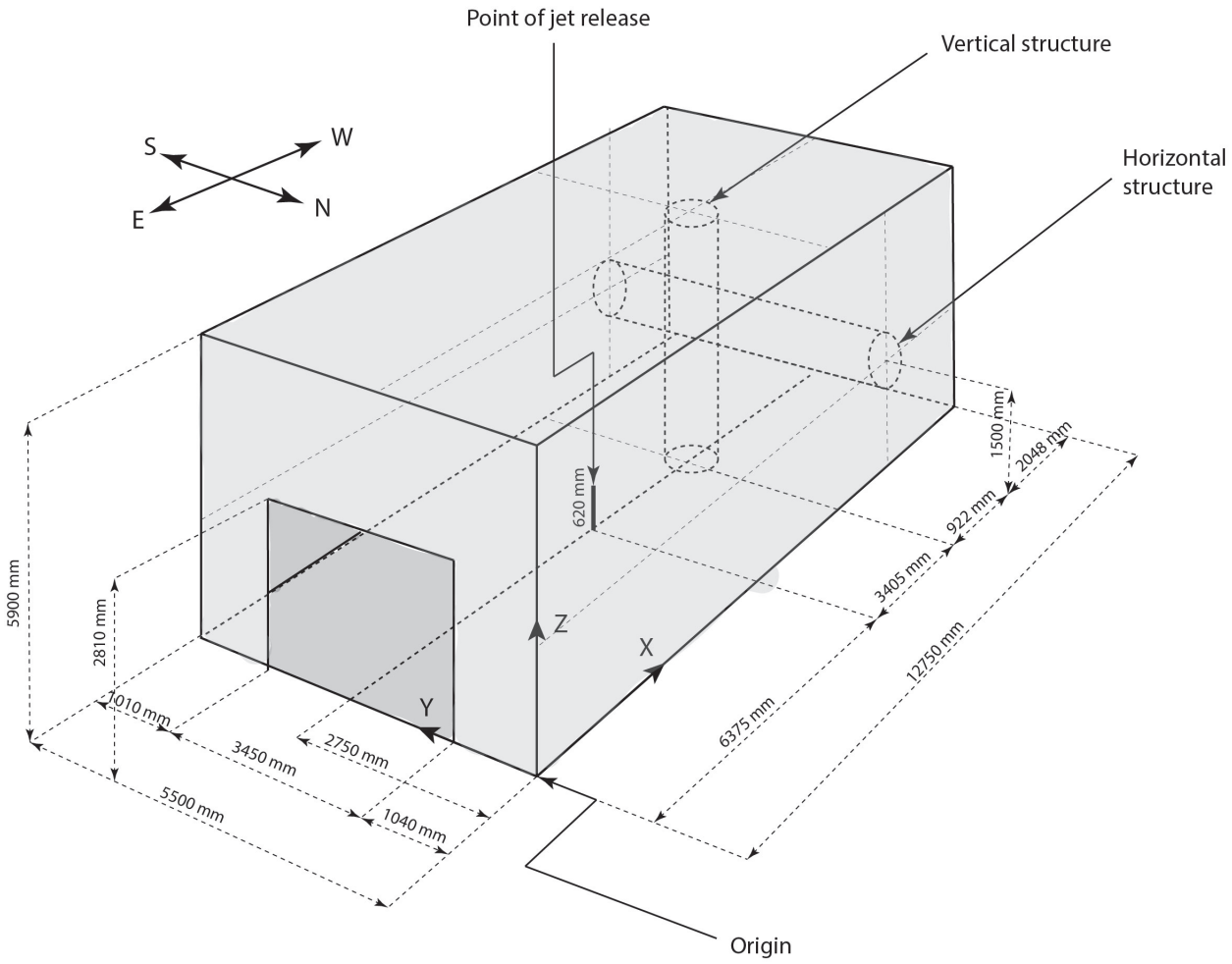

Figure 3.1: Fire enclosure geometry

the initial ambient air temperature. The conductivity (K) was calculated:

$$K_{\text{tot}} = \frac{\Delta x_{\text{tot}}}{\frac{\Delta x_{\text{lining}}}{K_{\text{lining}}} + \frac{\Delta x_{\text{insulation}}}{K_{\text{insulation}}}} = 0.161\text{W/mK} \tag{3.1}$$

Density ρ_{tot}:

$$\rho_{\text{tot}} = \frac{\rho_{\text{lining}}\Delta x_{\text{lining}} + \rho_{\text{insulation}}\Delta x_{\text{insulation}}}{\Delta x_{\text{tot}}} = 243.71\text{kg/m}^3 \tag{3.2}$$

Heat capacity $C_{\text{p,tot}}$:

$$C_{p,\text{tot}} = \frac{C_{p,\text{lining}}\rho_{\text{lining}}\Delta x_{\text{lining}} + C_{p,\text{insulation}}\rho_{\text{insulation}}\Delta x_{\text{insulation}}}{\rho_{\text{lining}}\Delta x_{\text{insulation}} + \rho_{\text{insulation}}\Delta x_{\text{insulation}}} = 0.997\text{kJ/kgK} \tag{3.3}$$

For the enclosure walls the absorption coefficient a was 0.9.

The compartment floor was modelled with a thickness of 0.151m and properties listed in

Drangsholt et al. [6] for Siporex: $\rho = 500\,\mathrm{kg/m^3}$, $C_p = 1\,\mathrm{kJ/kgK}$ and K=0.12 W/mk. After the geometry was made in Doozer, a geometry import was done generating a calculation grid, a simulation geometry model and a porosity file.

The geometry import created a geometry model in the KFX domain consisting of both solid cells and thin walled cells, described in Sec. (2.8). While the structures inside the enclosure (see Fig. (3.1)) were left as specified after the import, the enclosure wall, ceiling and floor cells were all altered to thin walled cells. The material properties and thicknesses of the walls and ceiling were left unaltered and equal to Eqs. (3.1), (3.2) and (3.3). The properties and thicknesses of the enclosure floor were altered from the Siporex properties to that of the ceiling and walls.

Initial and Boundary conditions

For the calculation domain, initial and boundary conditions were specified. The lower boundary of the domain was modelled as a solid isothermal wall to simulate the surface of earth. No heat or flow were allowed to pass through the boundary. The other boundaries of the domain were modelled as non-reflecting free flow boundaries. All outgoing flow were destructed and disappeared from the calculation domain. No wind was specified in the simulation, giving no inflow at the boundaries. Initial properties of the free flow cells in the calculation domain were that of air with a composition of 21 mol% O_2 and 79 mol% N_2. Initial temperature was 293 K. In the free flow cells, an initial value for turbulent kinetic energy of 1 J/kg and initial value of dissipation of turbulent kinetic energy of 1000 W/kg were chosen.

Numerical calculation and courant number

For the simulation, the equation solver convergence criterion was set to 0.0001. The time step was set to be between 0.005 s and 0.2 s. The Courant number had an initial value of 0.5, and increase factor (how much the Courant number can change per time step) of 1.1. In this thesis, the effect of the maximum Courant number was investigated by increasing the maximum Courant number during the simulation from 2 to 5.

3.1.2 Combustion

For the simulations in this thesis, 10 reactions were solved. In the reaction hierarchy, the hydrocarbon reactions were calculated simultaneously, before the the CO and H_2 reactions were calculated simultaneously. The calculated reactions were:

$$C_3H_8 + 1.5O_2 \rightarrow 3CO + 4H_2 \tag{3.4}$$

$$C_4H_{10} + 2O_2 \rightarrow 4CO + 5H_2 \tag{3.5}$$

$$C_5H_{12} + 2.5O_2 \rightarrow 5CO + 6H_2 \tag{3.6}$$

$$C_6H_{14} + 3O_2 \rightarrow 6CO + 7H_2 \tag{3.7}$$

$$C_7H_{16} + 3.5O_2 \rightarrow 7CO + 8H_2 \tag{3.8}$$

$$C_8H_{18} + 4O_2 \rightarrow 8CO + 9H_2 \tag{3.9}$$

$$C_9H_{20} + 4.5O_2 \rightarrow 9CO + 10H_2 \tag{3.10}$$

$$C_{10}H_{22} + 5O_2 \rightarrow 10CO + 11H_2 \tag{3.11}$$

$$CO + 0.5O_2 \rightarrow CO_2 \tag{3.12}$$

$$H_2 + 0.5O_2 \rightarrow H_2O \tag{3.13}$$

All cells were set to potentially ignite given the right conditions. Ignition time was set to 0 s.

3.1.3 Spray and Droplet modelling

For every species in the simulation, the number of numerical droplets that was released per second was 4000. The droplets were simulated to originate from the position x=6.375 m, y=2.75 m, z=0.62 m, with a composition given by Table (3.1). This composition was comparable to the composition used in JF5, given in Drangsholt et al. [6].

Table 3.1: Composition of fuel, mole fractions

Composition	mol%
Propane (C3)	0.007
Butane (C4)	7.075
Pentane (C5)	21.625
Hexane (C6)	12.517
Heptane (C7)	15.325
Octane (C8)	15.721
Nonane (C9)	7.949
Decane (C10)	19.783

Every component of the fuel were simulated as an independent spray, giving 8 independent sprays originating from the same position. The total mass flow rate of fuel, spraying

out of the nozzle, was for the first 850 s of the simulation, 0.85 kg/s. From 850 s to 894 s, a linear reduction to 0.75 kg/s was performed. The flow rate was held constant at 0.75 kg/s until 1004 s, before linearly decreasing to 0, reached at 1014 s. The mass injection rate for each of the fuels was calculated by:

$$\dot{M}_{\text{inj, fuel}} = \frac{\text{MW}_{\text{fu}} X_{\text{fu}}}{\sum_{k=C3}^{C10} \text{MW}_k X_k} \dot{M}_{\text{tot}} \tag{3.14}$$

where MW represents the molar mass and $\dot{M}_{\text{tot}}$ is the total flow rate. The spray pointed towards the compartment ceiling, with direction: x=0, y=0, z=1. The injection velocity was calculated as:

$$v = \frac{4\dot{M}_{\text{tot}}}{\pi d^2 \rho} \tag{3.15}$$

where d is the nozzle diameter (0.0057m) and ρ is the fuel mixture density (735 kg/m^3). The droplet temperature was 300K. The hollow cone angle was 0 degrees.

The initial droplet diameters of the fuels were given by the Sauter Mean Diameter (SMD), calculated from Witlox et al. [44]:

$$\text{SMD} = d(74\text{We}^{-0.85}\text{Re}^{0.44}(\frac{L_n}{d})^{0.114}(\frac{\mu_l}{\mu_w})^{0.97}(\frac{\sigma_{a,l}}{\sigma_{a,w}})^{-0.37}(\frac{\rho_l}{\rho_w})^{-0.11}) \tag{3.16}$$

where We is the Weber number given by:

$$\text{We} = \frac{\rho_l v^2 d}{\sigma_{a,l}} \tag{3.17}$$

and the Reynolds number (Re) is given by:

$$\text{Re} = \frac{\rho_l v d}{\mu_l} \tag{3.18}$$

L_n is the nozzle width. Given that the nozzle in this simulation had a circular orifice, L_n equals d. v is the injection velocity at a discharge rate of 0.85 kg/s (=44.78 m/s). μ is the dynamic viscosity, σ_a is the surface tension, ρ is the density. The subscript $_l$ refers to fuel saturated liquid properties at 16.5 bar (nozzle pressure) for density and dynamic viscosity, and 1 atm for surface tension. The subscript $_w$ refers to properties of water at standard conditions (pressure of 1 atm and temperature of 0°C). The calculated droplet diameters are given in Table (3.2).

The dispersion angle was defined as the angle of the outer edge of the spray in relation to the axial direction of the spray. The dispersion angle (θ) was calculated from Ashgriz [1](p.229)

$$\tan(\frac{\theta}{2}) = 0.31(\frac{\rho_g}{\rho})^{0.19} \tag{3.19}$$

where ρ_g is the density of the ambient gas, and ρ is the density of the fuel. Using a density of

Table 3.2: SMD – Droplet diameters

Component	SMD
Propane (C3)	531.1 μm
Butane (C4)	337.6 μm
Pentane (C5)	312.8 μm
Hexane (C6)	267 μm
Heptane (C7)	241 μm
Octane (C8)	231 μm
Nonane (C9)	193.4 μm
Decane (C10)	162 μm

1.2754 kg/m^3 for ρ_g and 735 kg/m^3 for ρ (which is the mixture density specified in Drangsholt et al. [6]), gave a dispersion angle of approximately 10°. This dispersion angle was chosen for all the components in the spray.

3.2 Alternative simulations

A selection of alternative simulations was made for investigating the effect different parameters could have on fire development.

3.2.1 Enclosure modelling

Due to the several ways of modelling solid structures in KFX, an understanding of the effects the different geometry modelling choices have is imperative. The effect of enclosure modelling was investigated through comparisons between a selection of cases.

Simple geometry case

The geometry model used in the simple geometry case was made in Doozer. The walls, ceiling and floor were made by simple shell boundaries. The properties of the walls were, initially, given typical values of steel: ρ=7850 kg/m^3, C_p=490 J/kgK and K=50 W/mK.

The geometry was imported into KFX, generating a calculation grid, a simulation geometry model and a porosity file. The simulation geometry model created in the calculation domain, had walls, ceiling and floor modelled as thin walled cells, described in Sec. (2.8). The structures at the inside of the enclosure (see Fig. (3.1)), were made out of a selection of solid and thin walled cells. The defined cell types were left unaltered in the calculation domain. The material properties and thicknesses of the imported geometry walls, ceiling and floor were altered to identical thickness, of 0.151 m, and properties, given in Eqs. (3.1), (3.2) and (3.3), as the advanced geometry case (base case). All other calculation parameters were left identical to the advanced geometry case. The only parameter differing the simple geometry case and the advanced geometry case, was the CAD model.

No-imported-geometry case

A simulation case was made without importing a Doozer CAD geometry model. An empty calculation grid was created equal to the one in the advanced geometry case (base case). A geometry was made in the calculation domain, as given in Fig. (3.1), but the horizontal and vertical structures were excluded. The insulated geometry walls, ceiling and floor were made out of thin walled cells, given in Sec. (2.8), with identical thickness, of 0.151 m, and properties, from Eqs. (3.1), (3.2) and (3.3), as the advanced geometry case (base case). All other calculation parameters were identical to the advanced geometry case (base case). The parameters differing the no-imported-geometry case and advanced geometry case (base case), were the CAD model import and the exclusion of the horizontal and vertical structures.

KFX geometry case

The KFX geometry case was identical to the advanced geometry case (base case), except that no cell alterations were done after the import. All cell types, material properties and thicknesses were as specified in Doozer and created by the KFX CAD import generator. The geometry cell types chosen by KFX, were a mix of thin walled cells and solid cells, as described in Sec. (2.8). All other calculation parameters were as specified for the advanced geometry case (base case).

Solid cell case

For investigation of the effect of different wall cell types, one case (hereafter called the solid cell case) was created for comparison against the advanced geometry case (base case). The case was identical to the advanced geometry case (base case), except where the advanced geometry case (base case) geometry cells were altered to thin walled cells, the solid cell case had geometry cells altered to solid cells as described in Sec. (2.8). All other parameters including material properties and thicknesses were identical to the advanced geometry case (base case).

Adiabatic case

The effect of the compartment insulation was investigated by setting up a case (hereafter called the adiabatic case), where the enclosure walls, ceiling and roof were modelled as adiabatic. The modelling of adiabatic walls was obtained by setting the heat conductivity (K) of the walls, ceiling and floor to 10^{-6} W/mK. Except for the heat conductivity, the case was identical to the advanced geometry case (base case). The adiabatic case was compared against the advanced geometry case (base case) to observe the effect of enclosure insulation on the fire development.

Big vent case

The effect of additional ventilation at the inside of the compartment was investigated through a case where the size of the ventilation opening was increased (hereafter called the big vent case). The size of the ventilation opening was adjusted by increasing the vent height with one cell row (0.2 m) and increasing the width of the vent to equal the width of the compartment. This meant an increase in vent area of approximately 7.8 m^2. The big vent case was identical to the advanced geometry case (base case), except for the vent size.

3.2.2 Spray dispersion

Spray dispersion is complex, with many parameters that could potentially affect the flame development. For this reason, simplified modelling of the spray, as seen in KFX [39], is done. An understanding of the impact the spray dispersion has on fire development, is important for further research into spray dispersion and fire modelling. For investigation of the effect of spray dispersion modelling, a selection of 5 cases were created, where different spray parameters were altered. All the cases were created with the advanced geometry case as a base. The parameters investigated were fuel composition, fuel flow rate, droplet diameter and dispersion angle.

One-component case

The effect the composition of the fuel had on fire development was investigated by comparing the advanced geometry case (base case), with a multicomponent fuel composition, with a single component fuel release case (the one-component case). The liquid component chosen as fuel was decane. Decane was chosen as fuel because of a density of approximately 730 kg/m^3, which was approximately the same as for the measured composition in Drangsholt et al. [6]. All other parameters than the fuel composition, were identical between the advanced geometry (base case) and the single component case.

Low fuel flow rate case

The effect of decreasing the fuel flow rate in the simulations was investigated by comparing the advanced geometry case (base case), with a case with half the fuel flow rate of the advanced geometry case (base case). This gave an initial fuel release rate, for the low fuel flow rate case, of 0.425 kg/s, and 0.375 kg/s after 894 s. All other parameters than the fuel composition were identical between the advanced geometry case (base case) and the low fuel flow rate case.

Small diameter case

For investigation of the effect of droplet diameters, two cases with different droplet diameters were created and compared against the advanced geometry case (base case). The small

diameter case was identical to the advanced geometry case (base case), except the droplet diameters were altered to $\frac{1}{5}$ th of the SMD values given in Table (3.2).

Large diameter case

The large diameter case was set up as the small diameter case, but with droplet diameters 5 times as large as the SMD values given in Table (3.2). The large diameter case was, otherwise, identical to the small diameter and the advanced geometry (base case) cases.

Small dispersion angle case

The effect of the dispersion angle of the spray was investigated through comparing the advanced geometry case (base case)(dispersion angle of 10°) with two cases with different dispersion angles. One of the cases (hereafter called the small dispersion angle case) had a dispersion angle of 5°, while otherwise being identical to the advanced geometry case (base case).

Large dispersion angle case

For the other case investigating the effect of the dispersion angle (hereafter called the large dispersion angle case) a dispersion angle of 20° was chosen. Except for the adjusted dispersion angle, the large dispersion angle case was identical to the small dispersion angle and advanced geometry cases (base case).

3.3 Logging of simulation parameters

History points

For logging of parameter and property values inside the calculation domain, a number of history points were distributed inside the calculation domain. The history points were placed at the cell centre and stored the specified properties in a separate file. This file contained the transient development of the chosen properties at the specified cell. One of the chosen properties, to be logged, was the thermocouple temperature. In JF5, thermocouple temperature was used for presentation of results. To be able to compare the simulated results with the results from JF5, thermocouple temperatures were modelled in KFX. The thermocouple temperature was modelled by heat exchange through a solid material. On one side of the material was the gas temperature, on the other side of the material was the thermocouple temperature. The thermocouple was modelled as a half sphere connected with a cylinder at the flat side. The diameter of the thermocouple was 0.0015 m and the length was 0.01 m, with direction in negative x-direction. The material properties were constant with a density of 8730 kg/m^3, heat capacity of 500 J/kgK, heat conductivity of 8 W/mK and a radiation absorption coefficient of 0.9 [39].

Bulletmonitor

At set points in the calculation domain, information about radiation was stored by using bullet monitors. Bullet monitors stored intensities calculated from the ray tracing in the discrete transfer radiation model on a spherical surface. The surface was split up in a number of solid angles, where every solid angle had an intensity connected to it. The desired number of solid angles was set to 9999, which describes how detailed the intensity distribution on the surface of the sphere is. To find the radiation heat flux related to a point on the surface, every intensity was multiplied with the cosine of the angle between the surface normal, and the direction vector from the point on the surface to the location of the intensity on the sphere around the point. The angle weighted intensities were integrated over the sphere to obtain a value for the radiation heat flux [39]. A number of locations for the bullet monitors were chosen, with a surface normal for the bullet monitors pointing towards the floor of the compartment (negative z-direction). Bullet monitor intensities were stored every second, giving a transient heat flux distribution.

3.3.1 Positions for logging of results during simulations

For the comparison of results 8 different logging points were chosen. 4 logging points showing temperature, 3 showing heat flux, and one showing flow rate. The positions of the logging points are given in: Table (3.3) and Fig. (3.2).

Table 3.3: Logging point positions

Label	Type	x–coordinate [m]	y–coordinate [m]	z–coordinate [m]
1	Thermocouple temperature [K]	-0.250	2.750	2.294
2	Thermocouple temperature [K]	3.250	2.750	4.524
3	Thermocouple temperature [K]	6.290	2.750	4.524
4	Thermocouple temperature [K]	12.750	1.350	4.600
5	Radiation heat flux (bullet monitor) [W/m^2]	1.005	2.750	5.900
6	Radiation heat flux (bullet monitor) [W/m^2]	6.745	2.750	5.900
7	Radiation heat flux (bullet monitor) [W/m^2]	11.755	2.750	5.900
8	Flow velocity $\vec{x}$ [m/s]	-0.250	2.750	0.365

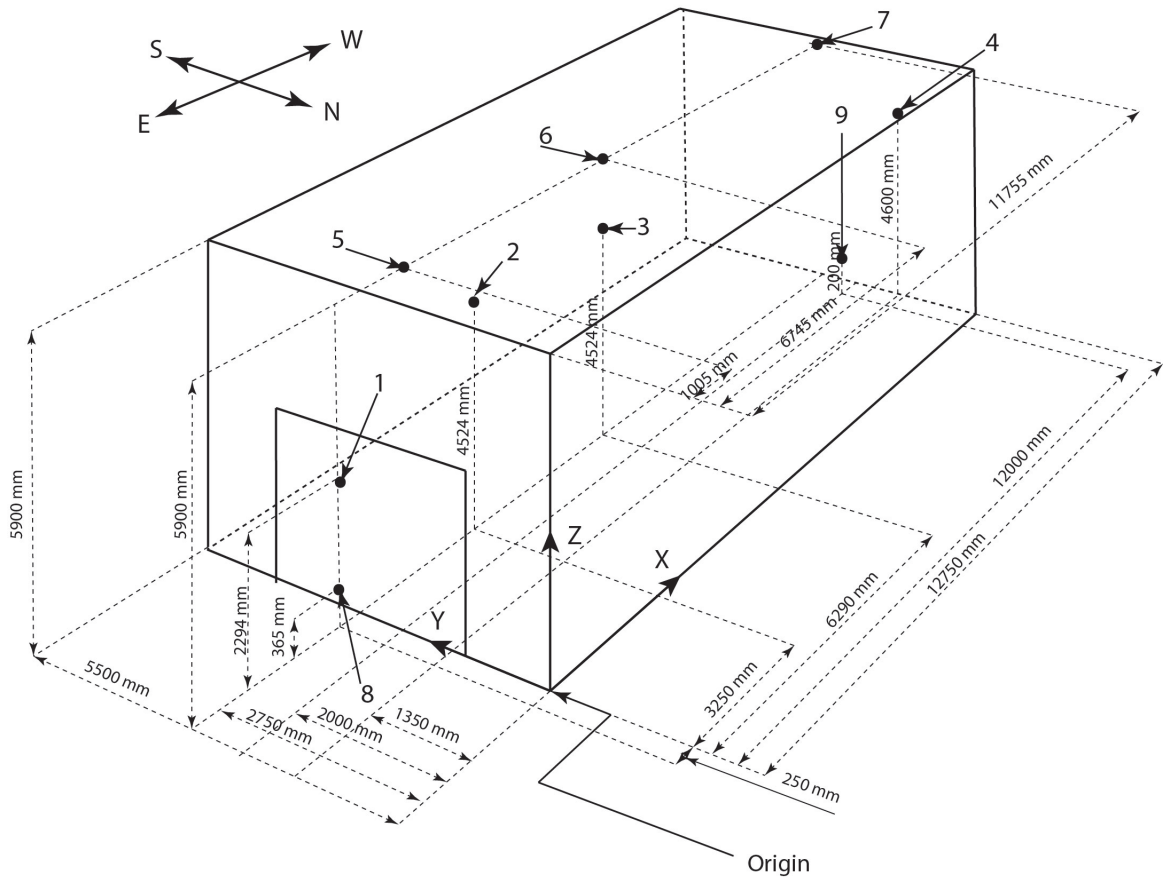

Figure 3.2: Position of logging points at the inside of the enclosure

Chapter 4

Results

4.1 3D CAD geometry model

For investigation of the effect a 3D CAD model has on the calculations, four different cases are compared: Three cases where the geometry and properties of the 3D CAD model were adjusted in the KFX domain window after the geometry import (advanced geometry (base case), simple geometry and no-imported-geometry cases), and one case where the geometry and properties of the geometry were not adjusted (KFX geometry case). The adjustments done were related to the grid and geometry in the calculation domain, and the porosity file. All other parameters in the cases are identical, as described in Ch. (3). By comparing the cases, the aim is to investigate the different ways of modelling the enclosure (modelling through the KFX geometry import, through the domain window and combinations of the two). The cases are compared on the basis of values obtained in the logging points 1-8.

Flame development

Large differences in flame development were observed between the KFX geometry case, and the simple geometry, advanced geometry (base case) and no-imported-geometry cases. Initially, all cases had similar flame development. At 0.22 s after fuel release, the flame was ignited close to the fuel release point. After ignition, the flame grew gradually towards the ceiling, impinging on the ceiling at 0.66 s after fuel release. The flame expanded along the ceiling, leading to a build up of a flame "layer" in the upper part of the enclosure. The flame layer increased in size, reaching the vent approximately 10 s after the fuel release was started. The flame stretched out through the vent and an external flame was established. After this point, the KFX geometry case had a different transient development than the simple geometry, advanced geometry (base case) and no-imported-geometry cases. For the KFX geometry case, the quasi-stable, upper layer flame was maintained. Flames were observed in the upper part of the enclosure, while oxygen were observed in the lower part of the enclosure. The simple geometry, advanced geometry (base case) and no-imported-geometry cases showed similar transient developments. At approximately 10 s from fuel release, flames close to the

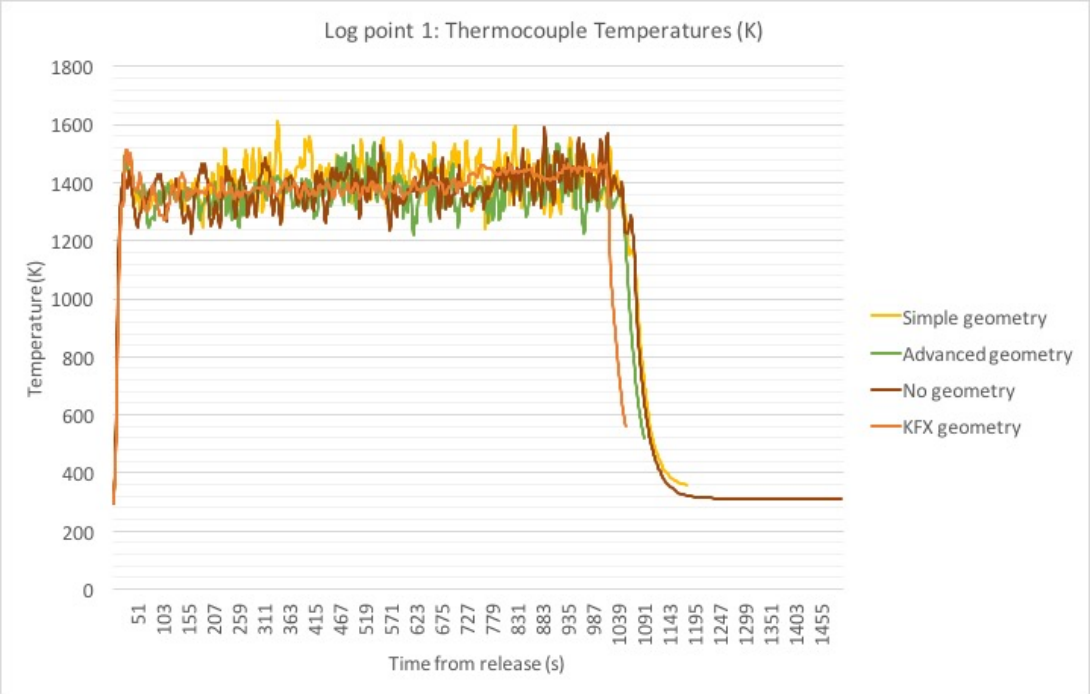

Figure 4.1: Investigation into the effect of 3D CAD model imports, Different CAD models and import procedures are compared, thermocouple temperatures, logging point 1.

west wall of the enclosure were extinguished. This resulted in the flame moving towards the vent in the east wall. From approximately 120 s after fuel release, a quasi-stable flame was observed at a boundary reaching from the fuel release point to the east wall. The flames stretched between the north and the south walls and were observed to enclose the upper part of the vent. On the east side of the boundary, oxygen was observed, and on the west side of the boundary, fuel was observed. The quasi-stable external flames in the simple geometry, advanced geometry (base case) and no-imported-geometry cases were observed to be significantly higher than what was observed in the KFX geometry case.

Temperatures at the inside of the compartment

Thermocouple temperatures at logging point 1 were similar for all four cases, given in Fig. (4.1). All cases showed a large increase in temperatures initially, followed by more stable temperatures of approximately 1400 K. In the quasi-stable temperature time period, a small transient increase in temperatures was observed. The KFX geometry case recorded smaller amplitudes in the temperature variations during the quasi-stable temperature time period, than the advanced geometry (base case), simple geometry and no-imported-geometry cases.

At logging point 2, given in Fig. (4.2), larger temperature differences between the cases than what was seen at logging point 1 were observed. The KFX geometry case generally recorded the highest temperatures. All four cases had a sharp initial increase in temperatures reaching up towards 1600 K, before a decrease to quasi-stable temperatures was observed. The KFX geometry case had a slow increase in temperatures for the duration of the quasi-

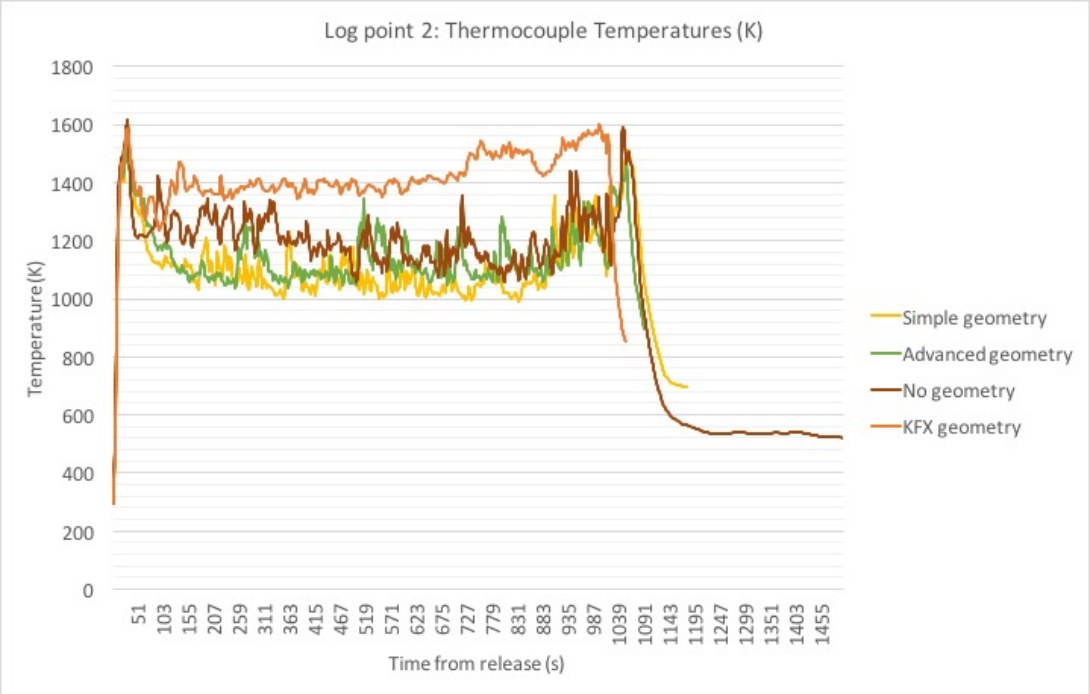

Figure 4.2: Investigation into the effect of 3D CAD model imports, Different CAD models and import procedures are compared, thermocouple temperatures, logging point 2.

stable temperature time period, reaching a maximum temperature of approximately 1600 K, before the fuel release was stopped. For the simple geometry, advanced geometry (base case) and no-imported-geometry cases, a sharper temperature increase was observed between 850 s and 1050 s after fuel release, reaching a maximum temperature of approximately 1600 K. The trend regarding temperature variations observed at logging point 1, was also seen at logging point 2.

At logging point 3, given in Fig. (4.3), the differences between the KFX geometry case and the advanced geometry (base case), simple geometry and no-imported-geometry cases, in recorded temperatures, was up towards 400 K. The simple geometry, advanced geometry (base case) and no-imported-geometry cases recorded similar temperature distributions, with the no-imported-geometry case generally logging slightly higher temperatures than the advanced (base case) and simple geometry cases, especially in the initial stages of the simulation. All cases logged a sharp temperature increase towards the end of the simulation. Less temperature variations were recorded at logging point 3 than at logging point 1 and 2.

At logging point 4, given in Fig. (4.4), the large differences in recorded temperatures between the KFX geometry case and the simple geometry, advanced geometry (base case) and no-imported-geometry cases, were further increased compared to logging point 3. The temperatures recorded at logging point 4, for the simple geometry, advanced geometry (base case) and no-imported-geometry cases were very similar to the temperatures recorded at logging point 3, while for the KFX geometry case a large temperature increase compared to logging point 3 was recorded. A maximum temperature of over 1800 K was observed for the KFX geometry case. The KFX geometry case also showed more temperature variations than

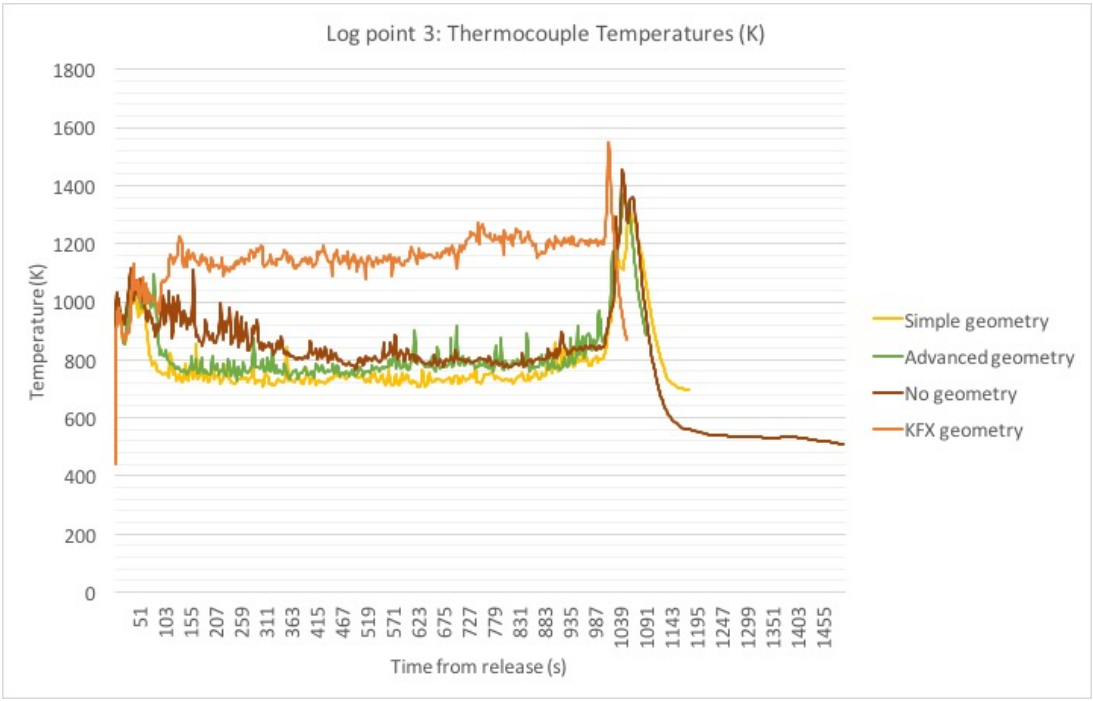

Figure 4.3: Investigation into the effect of 3D CAD model imports, Different CAD models and import procedures are compared, thermocouple temperatures, logging point 3.

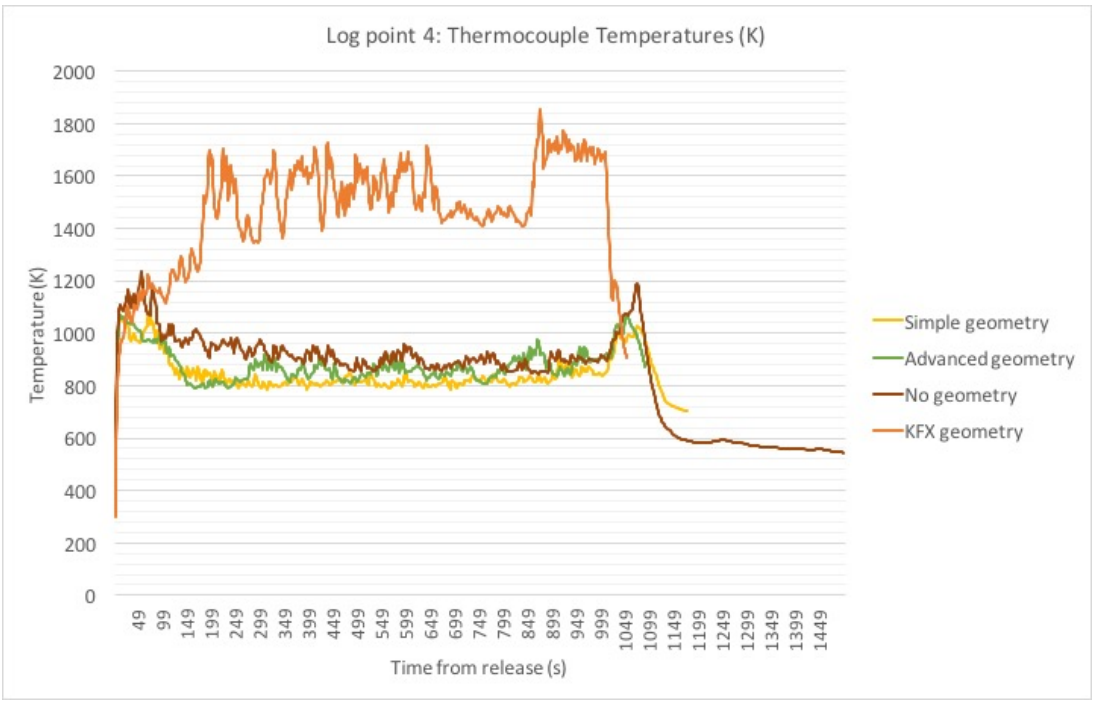

Figure 4.4: Investigation into the effect of 3D CAD model imports, Different CAD models and import procedures are compared, thermocouple temperatures, logging point 4.

the other three cases, with the amplitudes of the variations reaching as high as 450 K.

Wall temperatures

During the quasi-stable temperature time period, temperatures on the inside and outside surfaces of the wall were observed. For the simple and advanced geometry (base case) cases, temperatures between 600 and 1650 K were observed on the inside of the enclosure walls. The highest temperatures were observed close to the vent, while the coldest temperatures were observed close to the west wall of the enclosure. On the outside surface of the walls, uniform temperatures of approximately 300 K were observed, but higher temperatures of above 1600 K were observed on the outside surface of the east wall, facing the flame.

The temperatures recorded at the inside of the enclosure walls in the no-imported-geometry case, differed slightly from the simple and advanced geometry (base case) cases. The maximum temperatures close to the vent were approximately 1600 K, while the minimum temperatures, observed close to the west wall, were higher for the no-imported-geometry case, than the simple and advanced (base case) geometry cases, at approximately 800 K. On the outside of the enclosure walls, the temperatures recorded were less uniform than what was observed for the simple and advanced (base case) geometry cases, varying between approximately 290 and 390 K. The highest temperatures on the outside of the walls were located close to the vent, while the lower temperatures were located close to the west wall of the enclosure. As for the simple and advanced (base case) geometry cases, similarly high temperatures were recorded close to the flame, on the outside of the east wall.

For the KFX geometry case, the temperatures recorded on the inside of the enclosure walls differed from the simple geometry, advanced geometry (base case) and no-imported-geometry cases. Maximum temperatures of 1850 K and minimum temperatures of approximately 950 K were recorded at the inside of the enclosure walls. Interestingly, for the KFX geometry case, the highest temperatures were recorded close to the west wall, while the lowest temperatures were recorded close to the floor of the compartment. On the outside of the enclosure walls, temperatures between 265 and 350 K were recorded. The temperatures on the outside of the enclosure walls were highest close to the vent. On the outside of the east wall, similar temperature distributions as in the the simple geometry, advanced geometry (base case) and no-imported-geometry cases, were recorded. All four cases showed large transient temperature variations on the inside surface of the enclosure walls.

Radiation heat flux

During the simulations, radiation heat fluxes were logged at three positions just below the ceiling of the compartment, given in Figs. (4.5), (4.6) and (4.7). The recording of radiation heat fluxes showed a similar trend as observed for the temperatures, where more radiation heat flux were recorded in the KFX geometry case than the other cases.

At logging point 5, given in Fig. (4.5), the simple geometry, advanced geometry (base

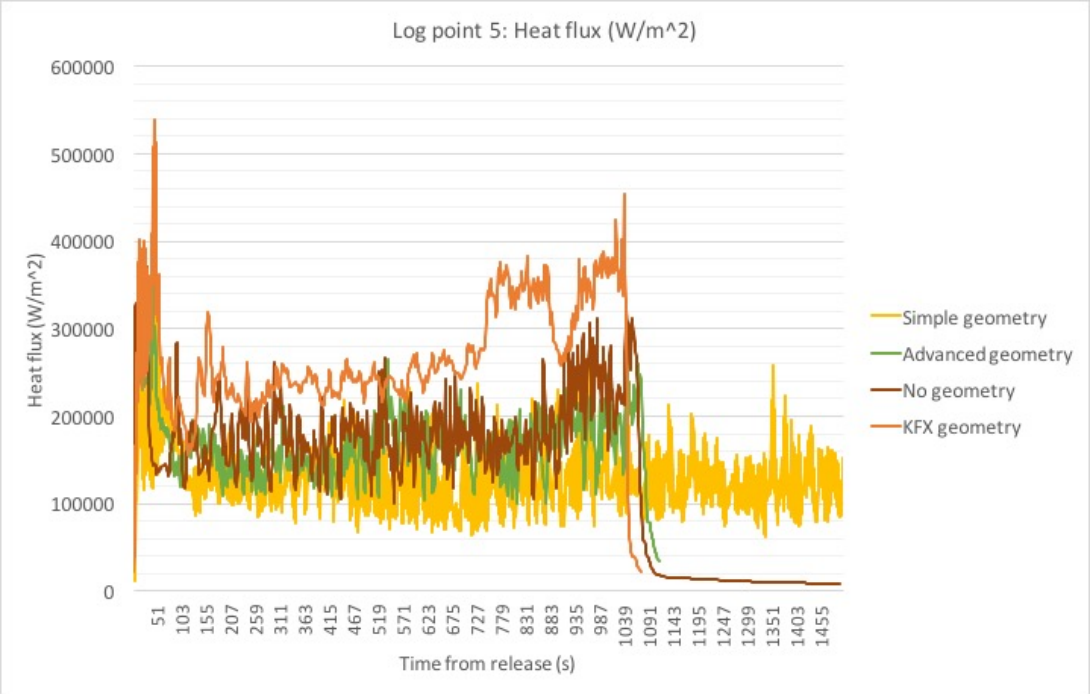

Figure 4.5: Investigation into the effect of 3D CAD model imports, Different CAD models and import procedures are compared, radiation heat flux, logging point 5

case) and no-imported-geometry cases recorded more variations in radiation heat flux than the KFX geometry case. variation amplitudes of approximately 100 kW/m^2 were logged, compared to approximately 50 kW/m^2 for the KFX geometry case. Initially, very high radiation heat fluxes were recorded for all cases, followed by a decrease to more stable values. All the cases except the simple geometry case, had a transient, noticeable, increase in recorded radiation heat flux during the quasi-stable period.

At logging point 6, given in Fig. (4.6), all the cases showed a decrease in recorded radiation heat flux compared to logging point 5. The simple geometry, advanced geometry (base case) and no-imported-geometry cases recorded less variations in radiation heat flux, while the KFX geometry case recorded more variations, compared to what were seen at logging point 5. Immediately before the fuel release was stopped, all cases showed a sudden increase in recorded heat fluxes. For the advanced geometry (base case), simple geometry and no-imported-geometry cases, the variations decreased transiently. The KFX geometry case showed an increase in recorded heat fluxes after approximately 700 s after the fuel release was started.

At logging point 7, given in Fig. (4.7), the heat fluxes recorded for the simple geometry, advanced geometry (base case) and no-imported-geometry cases were very similar to that logged at logging point 6, but with smaller peaks in the heat fluxes observed close to the end of the simulation. The KFX geometry case showed a different transient development at logging point 7, compared to logging point 6. The recorded heat fluxes were much higher and with much more variations.

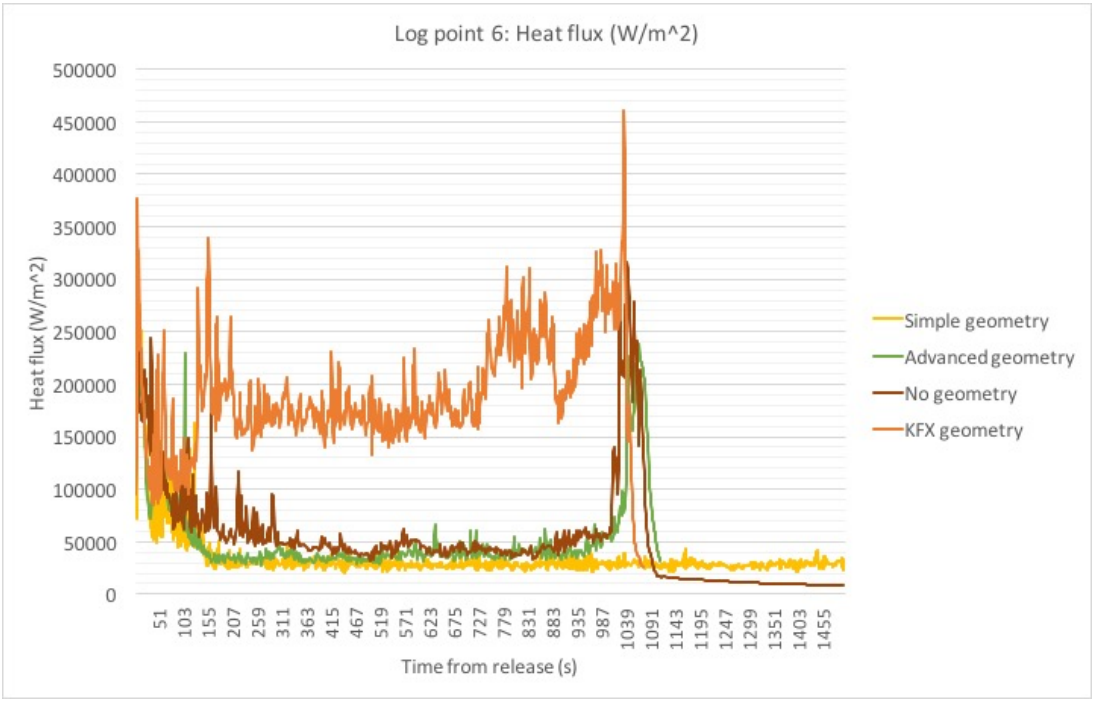

Figure 4.6: Investigation into the effect of 3D CAD model imports, Different CAD models and import procedures are compared, radiation heat flux, logging point 6

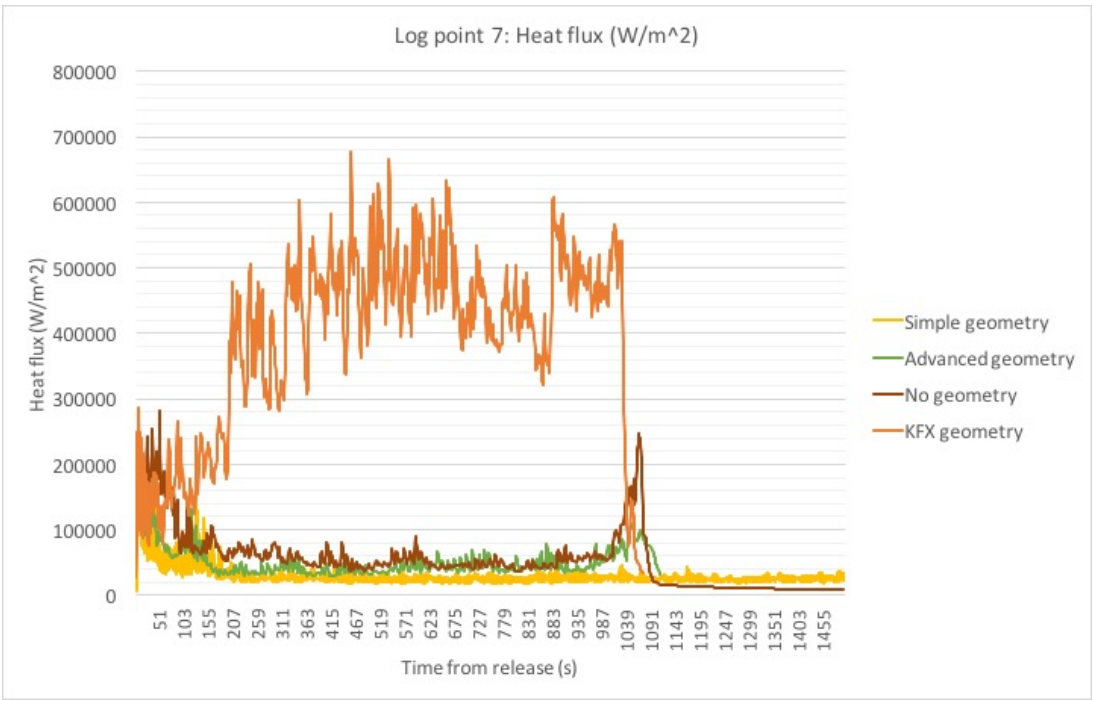

Figure 4.7: Investigation into the effect of 3D CAD model imports, Different CAD models and import procedures are compared, radiation heat flux, logging point 7

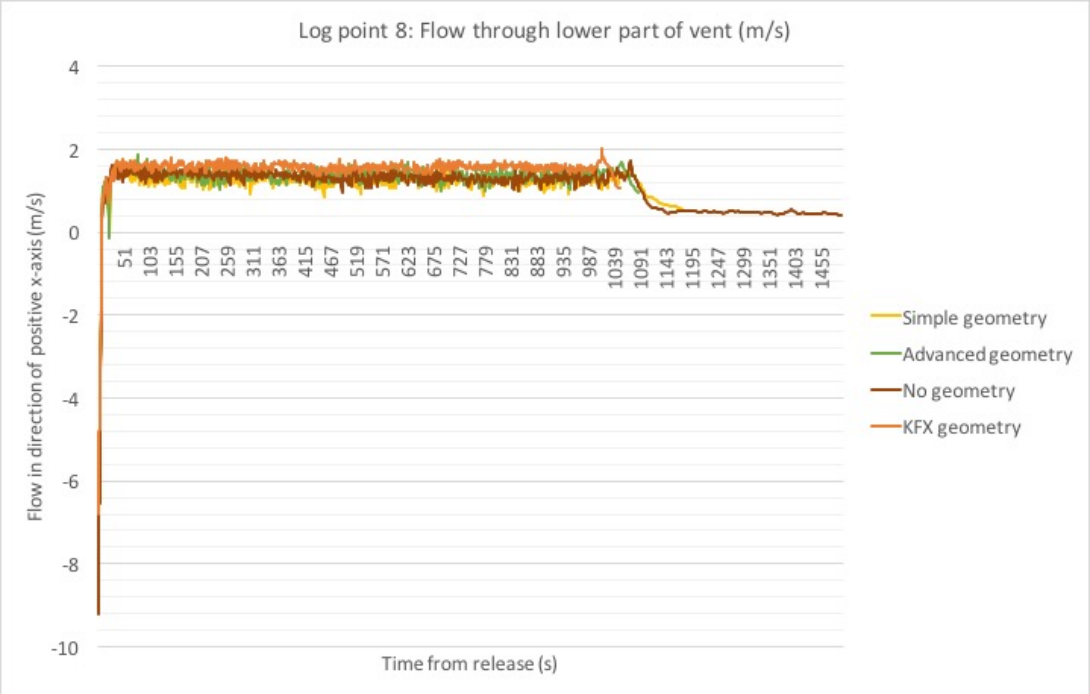

Figure 4.8: Investigation into the effect of 3D CAD model imports, Different CAD models and import procedures are compared, vent flow, logging point 8

Oxygen distribution

Logging of oxygen inside the enclosure was done at the z=0.3 m plane. Logging of the vent flow was done at logging point 8, given in Fig. (4.8). For logging of oxygen content inside the enclosure, transient development in the quasi-stable temperature time span was observed. At logging point 8, a flow was observed entering the compartment.

For the simple geometry, advanced geometry (base case) and no-imported-geometry cases, oxygen of approximately atmospheric quantity, as described in Sec. 3.1.1, was observed to enter 5-7 m into the room, measured from the vent. For the advanced geometry (base case) and no-imported-geometry cases, the oxygen was observed to flutter between the south wall and the north wall. The KFX geometry case showed a very different development regarding air flow inside the enclosure, than the three other cases. At the z=0.3 m plane, oxygen of approximately atmospheric quantity was observed reaching all parts of the compartment. While oxygen was observed at all positions, some low oxygen areas were observed at various positions during the simulation.

4.2 Thin walled and solid cell enclosure construction

In the KFX domain solid constructions can basically be modelled in two different ways, with solid cells or thin walled cells, given in Sec. (2.8). The comparison of the advanced geometry (base case)(thin walled cell construction) and the solid cell (solid cell construction) cases, is done to investigate the effect the choice of solid cell type has on the simulations.

Flame development

The advanced geometry (base case) and solid cell cases recorded similar initial fire development. The initial flame development was as described in Sec. (4.1). From approximately 120 s after start of the fuel release, a quasi-stable fire was observed inside the compartment. The quasi-stable flames of the advanced geometry case (base case) and the solid cell case were slightly different. While both cases developed flames in the boundary between an oxygen rich zone close to the vent and a fuel rich zone facing the west wall, the flame zone was thinner for the solid cell case. The flame of the solid cell case reached from the floor at approximately 4 m into the enclosure, measured from the vent, to the upper edge of the vent. The flames of the adiabatic case did not enclose the upper part of the vent and east wall, as were observed for the advanced geometry case (base case). From approximately 930 s after fuel release, the flame was observed to increase for the solid cell case, with stable flames in the east half of the room from approximately 940 s.

Temperatures

At logging point 1, given in Fig. (4.9), the advanced geometry case (base case) and the solid cell case recorded very similar temperatures. For the advanced geometry case (base case), slightly higher temperatures were recorded initially compared to the solid cell case. The solid cell case had a more gradual increase to quasi-stable temperatures than the advanced geometry case (base case). Similar temperature variations were recorded for both cases in the quasi-stable temperature period.

At logging point 2, given in Fig. (4.10), slightly higher temperatures were recorded initially for the advanced geometry case (base case), compared to the solid cell case. The temperature differences between the cases diminished during the transient development, leading to approximately equal temperatures at the end of the simulations.

Similar trends as seen at logging point 2, continued at logging point 3, given in Fig. (4.11). The advanced geometry case (base case) generally recorded higher temperatures than the solid cell case. Although diminishing slightly, a temperature difference between the cases was observed transiently to the end of the simulation. For both cases, a sharp increase in temperatures was observed before the fuel release was stopped.

For logging point 4, given in Fig. (4.12), the thermocouple temperature logging point of the solid cell case was located inside the wall. The temperatures recorded in the solid cell case can therefore not be compared to the thermocouple temperatures recorded for the advanced geometry case (base case).

Radiation heat flux

The logging of radiation heat fluxes revealed similar trends as observed for the temperatures. High radiation heat fluxes initially, followed by a decrease to quasi-stable values, were observed at all three radiation heat flux logging points. Higher heat fluxes and more variations

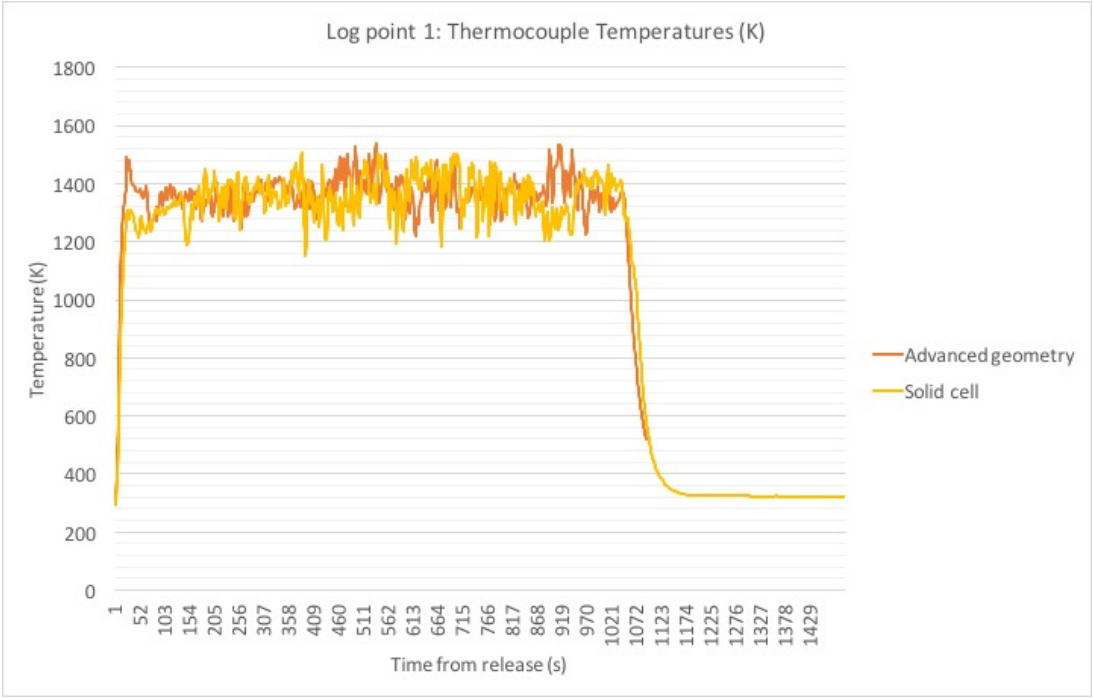

Figure 4.9: Investigation into the effect of different cell types for modelling of solid walls. Solid cell type is compared to thin walled cell type. thermocouple temperatures, logging point 1

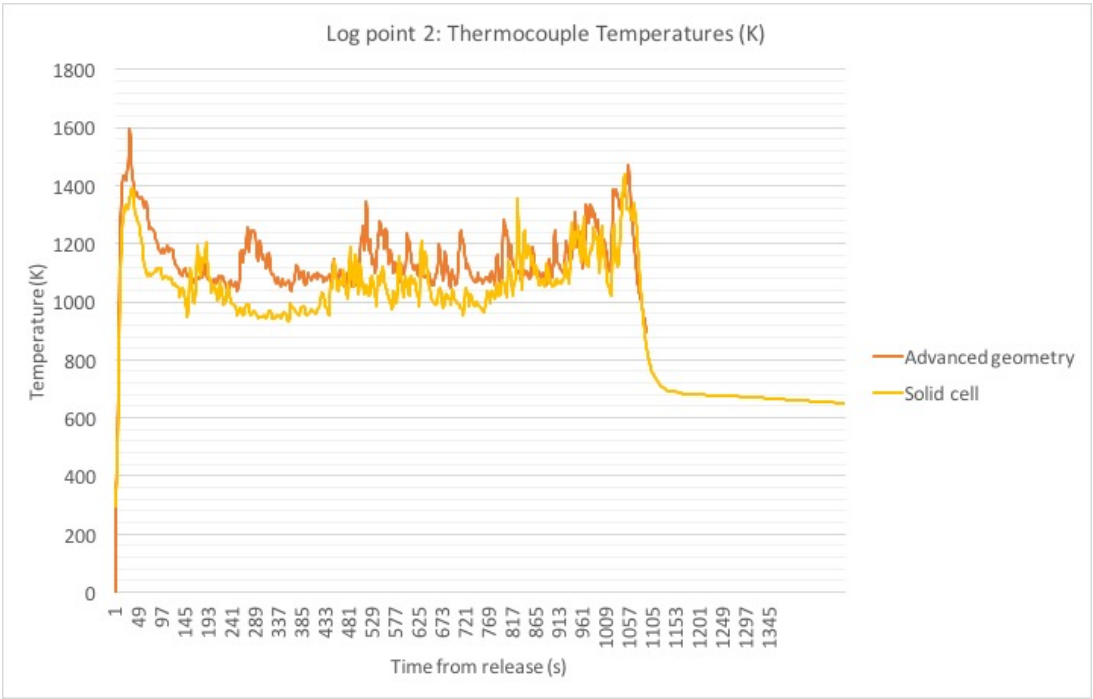

Figure 4.10: Investigation into the effect of different cell types for modelling of solid walls. Solid cell type is compared to thin walled cell type. thermocouple temperatures, logging point 2

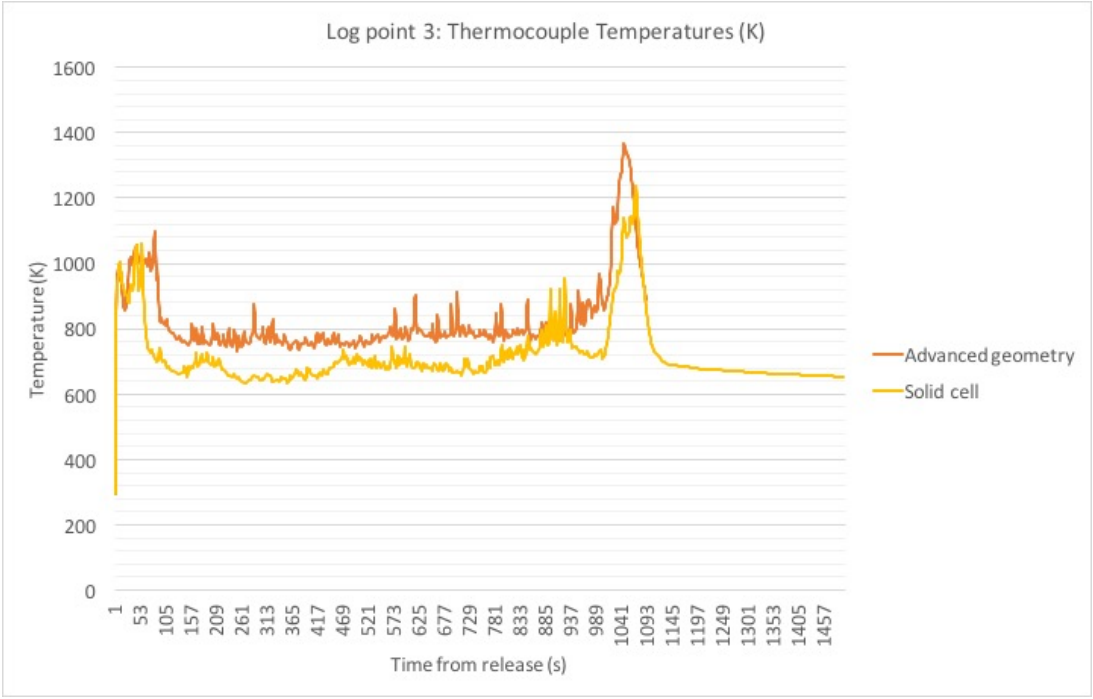

Figure 4.11: Investigation into the effect of different cell types for modelling of solid walls. Solid cell type is compared to thin walled cell type. thermocouple temperatures, logging point 3

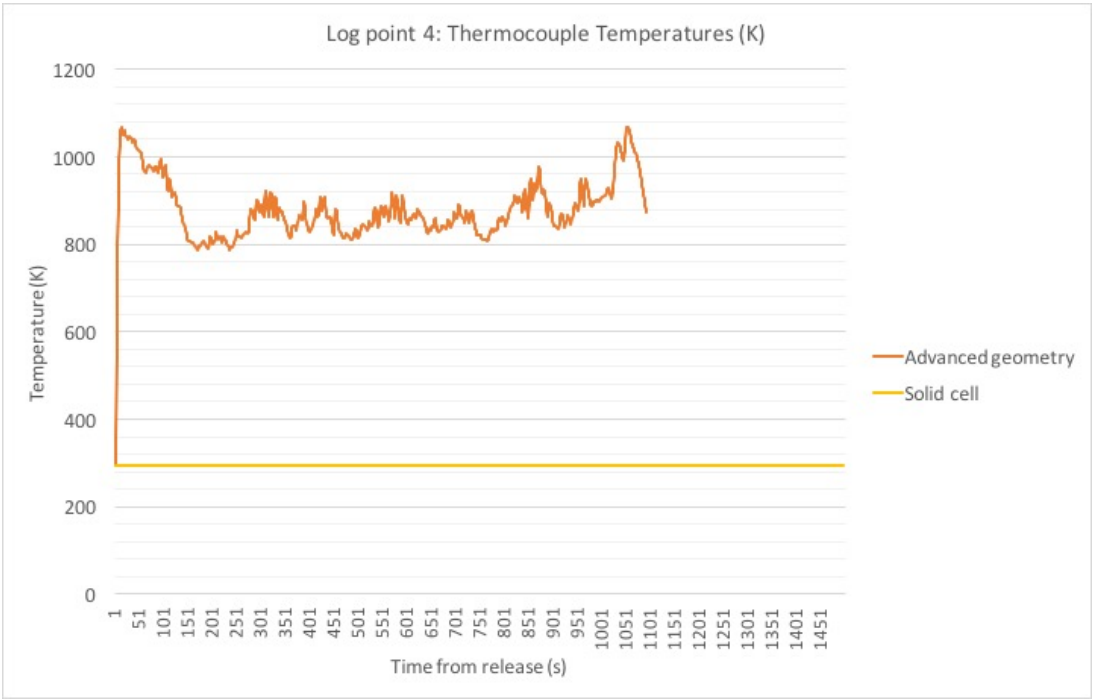

Figure 4.12: Investigation into the effect of different cell types for modelling of solid walls. Solid cell type is compared to thin walled cell type. thermocouple temperatures, logging point 4

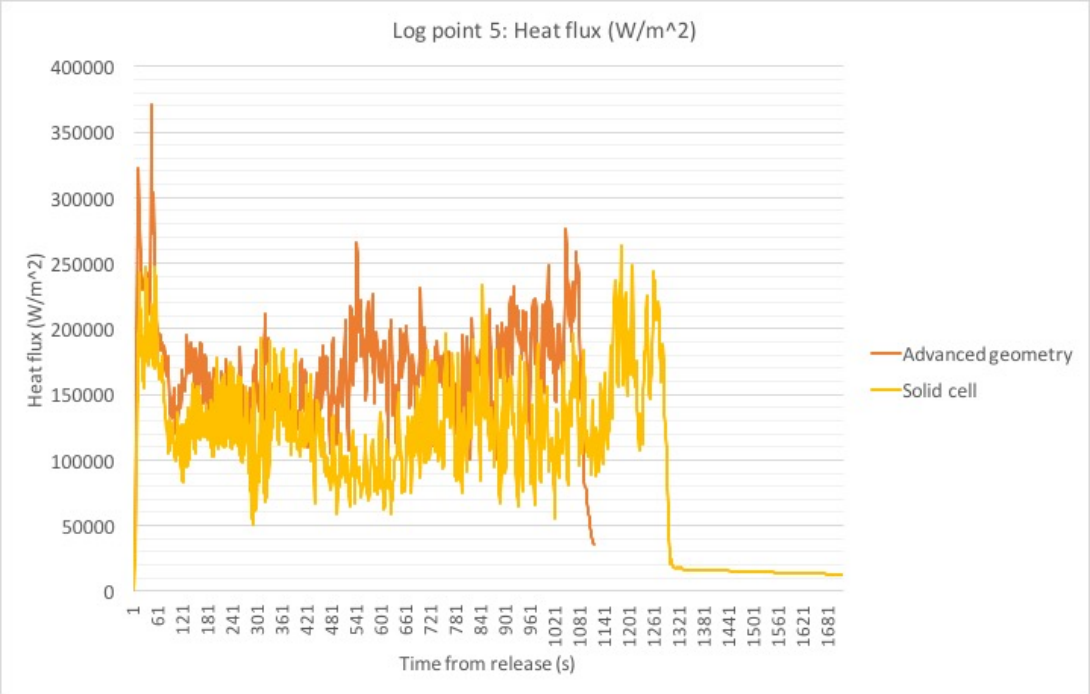

Figure 4.13: Investigation into the effect of different cell types for modelling of solid walls. Solid cell type is compared to thin walled cell type. Radiation heat flux, logging point 5

were observed for both the advanced geometry (base case) and solid cell cases at logging point 5, given in Fig. (4.13), than observed at logging points 6, given in Fig. (4.14), and at logging point 7, given in (4.15). At all logging points, the advanced geometry case (base case) recorded slightly higher radiation heat fluxes than the solid cell case. At logging points 6 and 7, the difference in radiation heat flux between the cases was observed to increase transiently. For both the advanced geometry case (base case) and the solid cell case, a peak of high heat fluxes was recorded close to the end of the simulation at logging points 6 and 7. Interestingly, the peak of the solid cell case was observed 200 s after the advanced geometry case (base case). At logging point 5, while the radiation heat flux of the advanced geometry case (base case) started to diminish from approximately 1050 s, the recorded radiation heat flux of the solid cell case continued to increase until approximately 1300 s after start of fuel release.

Oxygen inside the compartment

The oxygen quantity inside the compartment was logged at the z=0.3 m plane during the quasi-stable temperature time. Logging of flow in u direction was done at logging point 8, given in Fig. (4.16). The advanced geometry case (base case) and the solid cell case showed very similar development regarding oxygen quantity inside the compartment and flow through the lower part of the vent.

For both cases, approximately atmospheric oxygen was observed to enter 5-7 m into the enclosure, measured from the vent. The distance the oxygen reached into the compartment

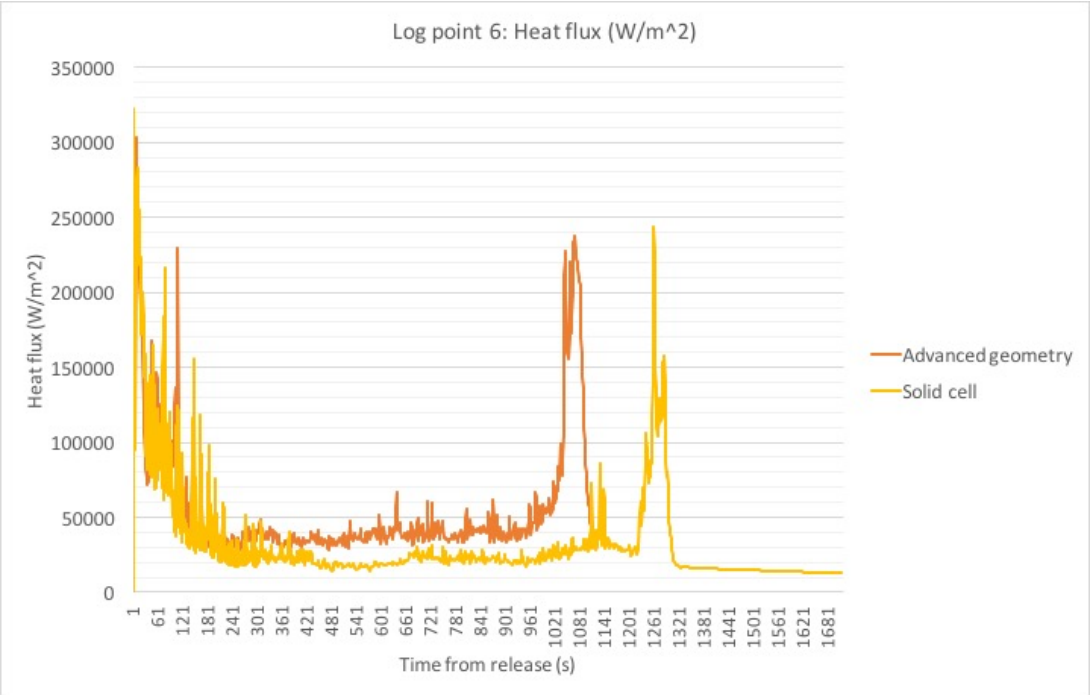

Figure 4.14: Investigation into the effect of different cell types for modelling of solid walls. Solid cell type is compared to thin walled cell type. Radiation heat flux, logging point 6

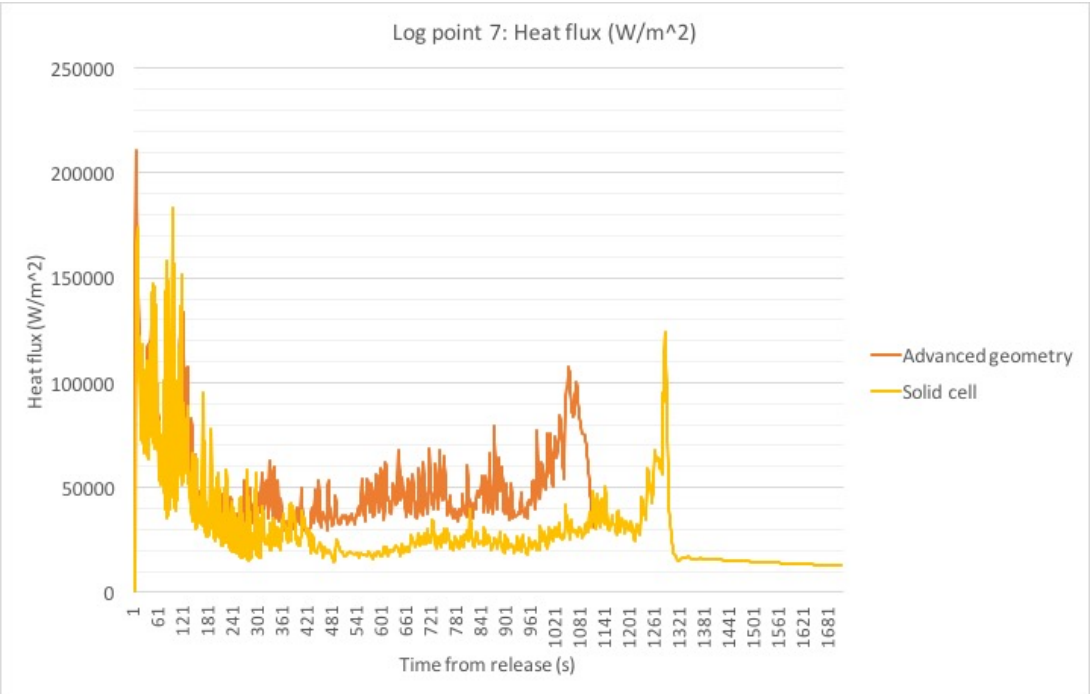

Figure 4.15: Investigation into the effect of different cell types for modelling of solid walls. Solid cell type is compared to thin walled cell type. Radiation heat flux, logging point 7

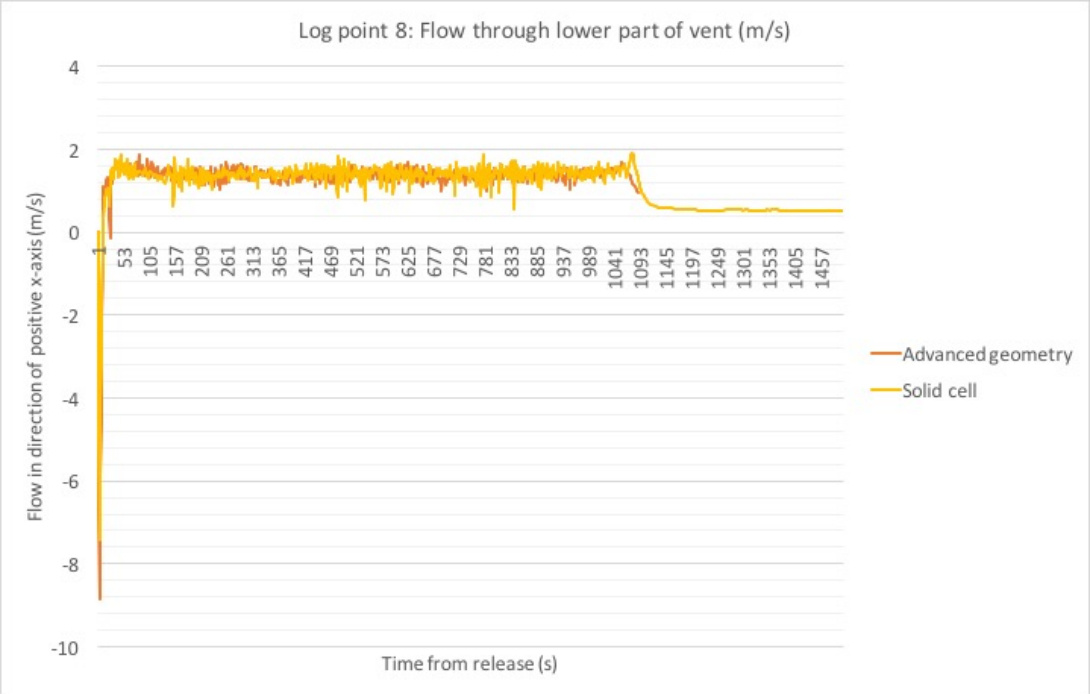

Figure 4.16: Investigation into the effect of different cell types for modelling of solid walls. Solid cell type is compared to thin walled cell type. vent flow, logging point 8

was very stable for both cases, but for both cases the oxygen was observed to flutter in y-direction, between the north wall and the south wall.

4.3 Fuel composition and flow rate of spray

The effect of the fuel composition and the flow rate of fuel are investigated through a comparison of the advanced geometry (base case), low fuel flow rate and one-component cases. The advanced geometry case (base case) had the fuel flow rate given in [6] and described in Sec. (3.1.3). In the low fuel flow rate case the fuel flow rate was halved, compared to the advanced geometry case (base case). In the one-component case, the flow rate was identical to the advanced geometry case (base case), but the fuel composition consisted only of decane.

Flame development

The one-component and advanced geometry (base case) cases showed similar flame development. Initial flame development for the advanced geometry (base case), low fuel flow rate and one-component cases was as described in Sec. (4.1). For the advanced geometry (base case) and one-component cases, during the quasi-stable temperature time period, stable flames were observed stretching from the fuel release point to the east wall, between the north wall and south wall, enclosing the upper part of the vent and the east wall. The flames were observed on a boundary between fuel on the west side of the flame, and air on the east side of the flame. The low fuel flow rate case showed a different flame development after the

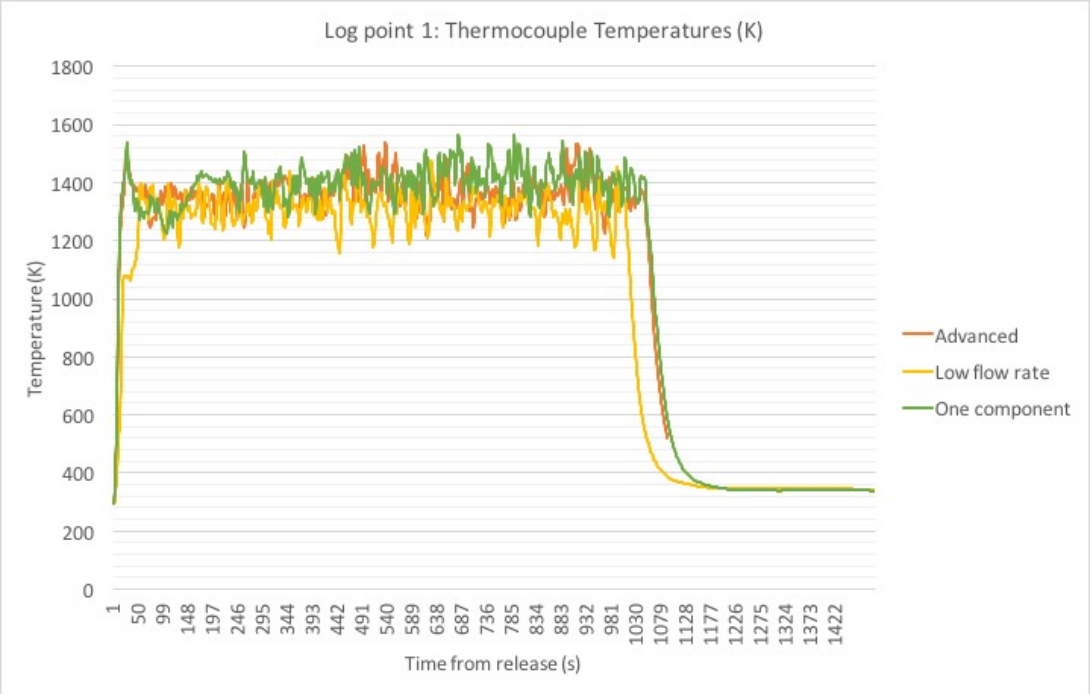

Figure 4.17: Investigation into the effect of different fuel compositions and fuel flow rates. The advanced geometry case (base case), with initial flow rate of 0.85 kg/s and composition given in Table. (3.1), is compared with one case with half the flow rate of the advanced geometry case (base case) and one case with pure decane as fuel. thermocouple temperatures, logging point 1.

initial period, where the flame layer in the upper part of the enclosure was maintained for as long fuel was released.

Temperatures

At the position of logging point 1, given in Fig. (4.17), similar temperatures were observed for all cases. The low fuel flow rate case recorded slightly lower temperatures than the other cases, during the quasi-stable temperature period. When the fuel release was stopped, the final decrease in temperatures happened earlier for the low fuel flow rate case. The low fuel flow rate case also had a slightly more gradual increase in temperatures up to the quasi-stable temperatures.

At logging point 2, given in Fig. (4.18), a difference in temperatures were observed. The low fuel flow rate case recorded higher temperatures than the advanced geometry (base case) and one-component cases. The advanced geometry case (base case) and the one-component case had a very similar temperature development, where similar temperatures were recorded. Interestingly, the frequency of the variations of the low fuel flow rate case in the quasi-stable temperature time period was very stable and similar amplitudes in temperature were recorded. The final temperature decrease was observed earlier for the low fuel flow rate case, than for the advanced geometry (base case) and one-component cases.

As for logging point 2, the low fuel flow rate case generally recorded higher temperatures

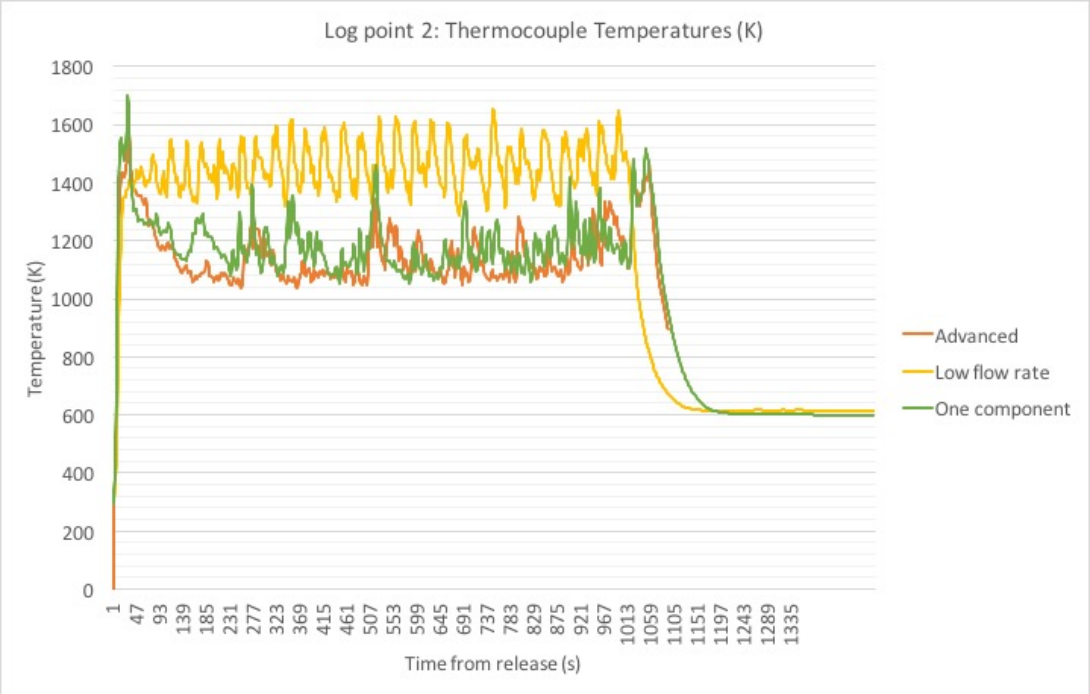

Figure 4.18: Investigation into the effect of different fuel compositions and fuel flow rates. The advanced geometry case (base case), with initial flow rate of 0.85 kg/s and composition given in Table. (3.1), is compared with one case with half the flow rate of the advanced geometry case (base case) and one case with pure decane as fuel. thermocouple temperatures, logging point 2.

than the advanced geometry (base case) and one-component cases at logging point 3, given in Fig. (4.19). The large variations seen for the low fuel flow rate case at logging point 2 were also observed at logging point 3. The advanced geometry case (base case) and the one-component case recorded similar temperature distributions and for both cases a sharp temperature increase was observed finally, when the fuel release was stopped. The final temperature increase of the one-component case was significantly higher than what was observed for the advanced geometry (base case) and low fuel flow rate cases, reaching close to 1700 K. The final temperature decrease was observed earlier for the low fuel flow rate case than for the advanced geometry (base case) and one-component cases.

At logging point 4, given in Fig. (4.20), the temperature development of the advanced geometry (base case) and one-component cases was very similar, as also observed at the other temperature logging points. The low fuel flow rate case recorded higher temperatures than the two other cases, but the stable variations seen at logging point 2 and 3 were slightly more unstable at logging point 4. The final temperature decrease, after the fuel release was stopped was observed earlier for the low fuel flow rate case, as also noted for logging points 2 and 3.

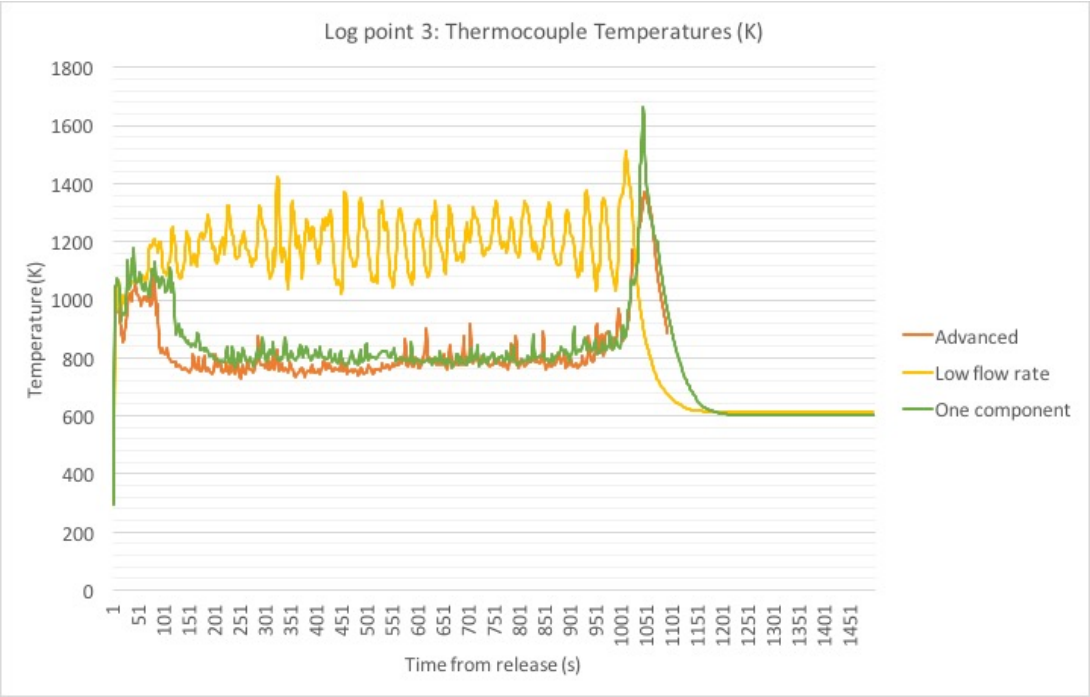

Figure 4.19: Investigation into the effect of different fuel compositions and fuel flow rates. The advanced geometry case (base case), with initial flow rate of 0.85 kg/s and composition given in Table. (3.1), is compared with one case with half the flow rate of the advanced geometry case (base case) and one case with pure decane as fuel. thermocouple temperatures, logging point 3.

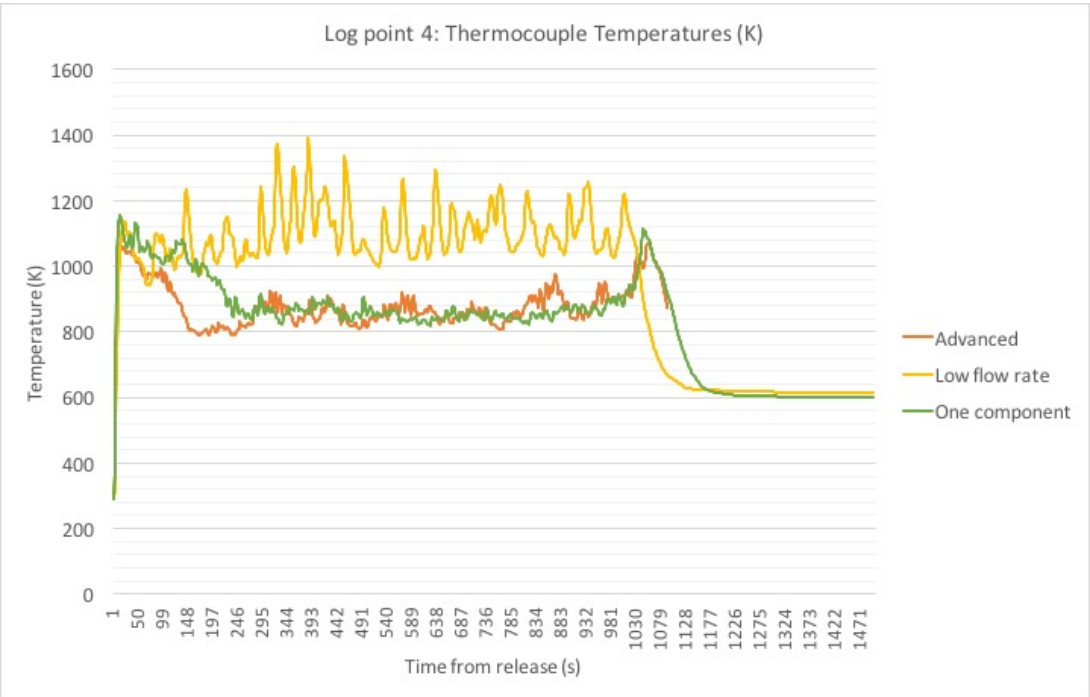

Figure 4.20: Investigation into the effect of different fuel compositions and fuel flow rates. The advanced geometry case (base case), with initial flow rate of 0.85 kg/s and composition given in Table. (3.1), is compared with one case with half the flow rate of the advanced geometry case (base case) and one case with pure decane as fuel. thermocouple temperatures, logging point 4.

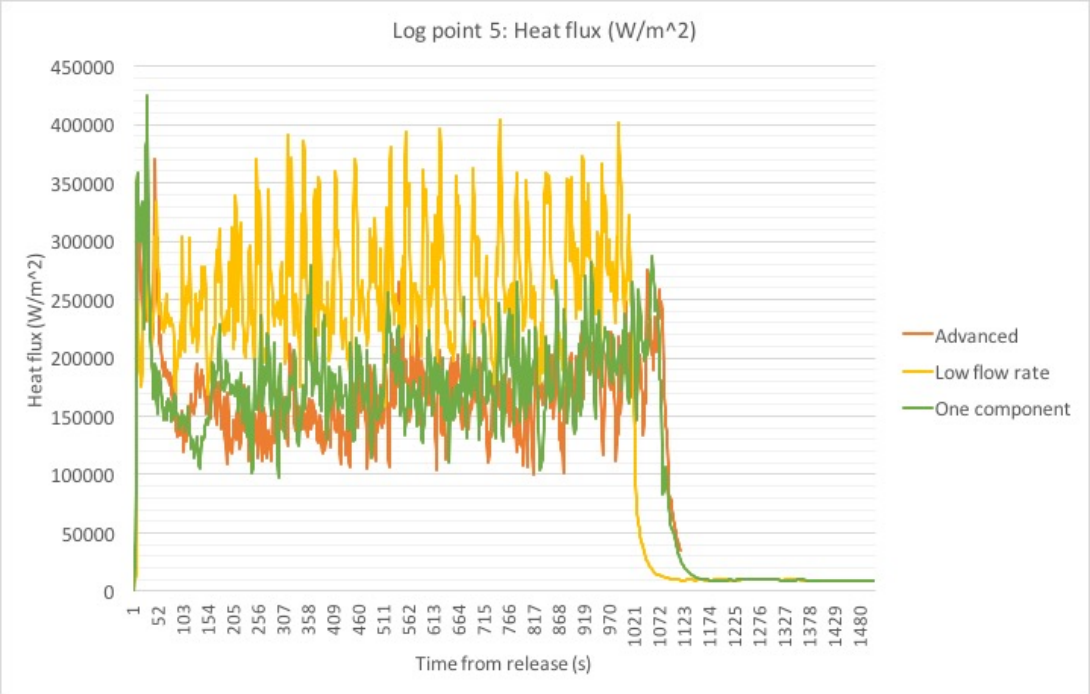

Figure 4.21: Investigation into the effect of different fuel compositions and fuel flow rates. The advanced geometry case (base case), with initial flow rate of 0.85 kg/s and composition given in Table. (3.1), is compared with one case with half the flow rate of the advanced geometry case (base case) and one case with pure decane as fuel. Radiation heat flux, logging point 5.

Radiation heat flux

At logging points 5, 6 and 7, given in Figs. (4.21), (4.22) and (4.23), the three cases showed similar trends regarding radiation heat fluxes, as observed for the temperatures at logging points 2, 3 and 4. The advanced geometry case (base case) and the one-component cases recorded very similar radiation heat fluxes, while the low fuel flow rate case generally recorded higher radiation heat fluxes at all the logging points 5, 6 and 7. The low fuel flow rate case recorded very high variations in radiation heat fluxes compared to the advanced geometry (base case) and one-component cases, variations of up to 400 kW were recorded.

Oxygen quantity and flow rate

Observations of oxygen quantity inside the compartment were conducted during the quasi-steady temperature time period, at the z=0.3 m plane. For the one-component case, similar oxygen distributions as for the advanced geometry case (base case) were observed. Oxygen was observed to flow 5-7 m into the enclosure, measured from the vent. In the low fuel flow rate case, oxygen was observed entering all parts of the enclosure at the z=0.3 m plane.

Regarding flow through the lower part of the vent, given in Fig. (4.24), the three cases showed similar distributions. For the low fuel flow rate case, the inflow into the compartment decreased earlier after the fuel flow rate was stopped, than what was observed for the

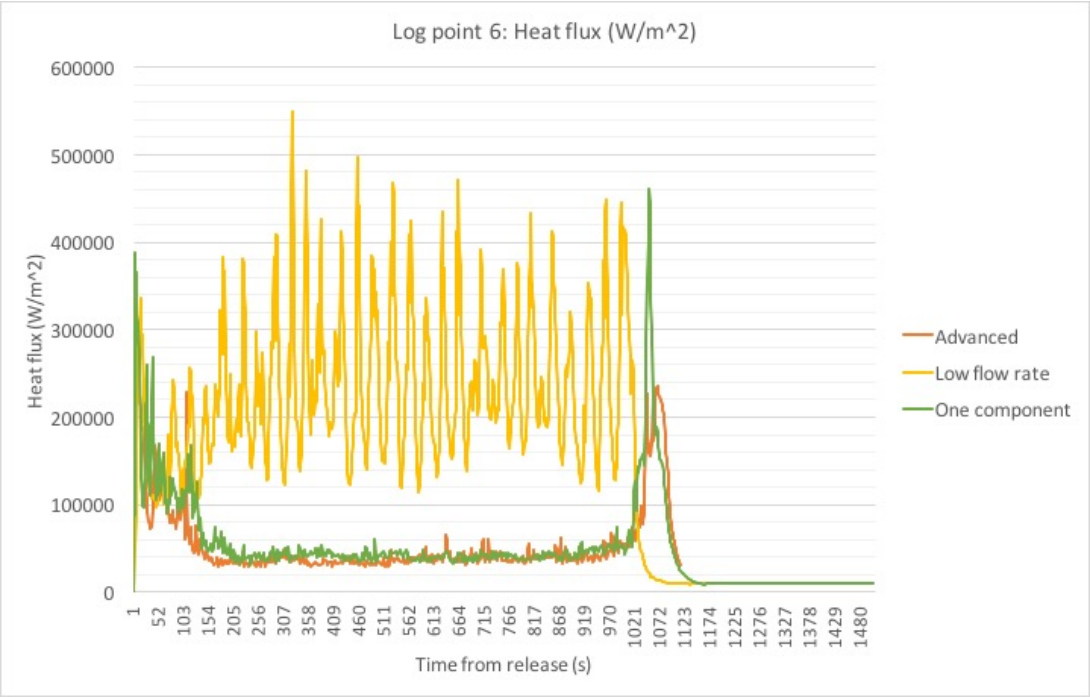

Figure 4.22: Investigation into the effect of different fuel compositions and fuel flow rates. The advanced geometry case (base case), with initial flow rate of 0.85 kg/s and composition given in Table. (3.1), is compared with one case with half the flow rate of the advanced geometry case (base case) and one case with pure decane as fuel. Radiation heat flux, logging point 6.

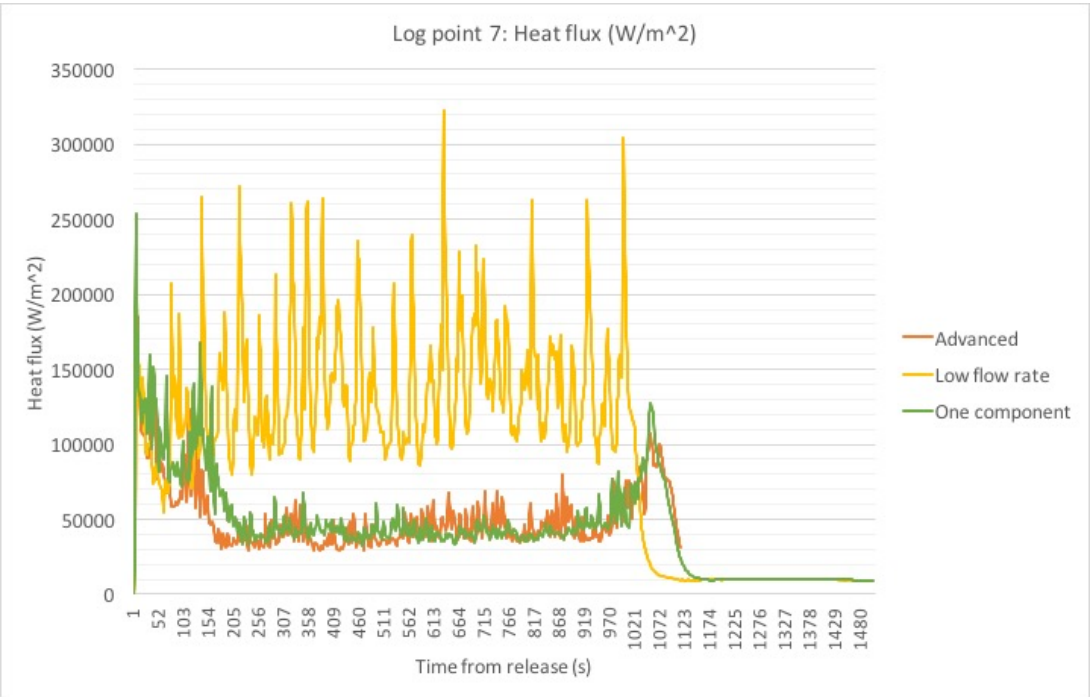

Figure 4.23: Investigation into the effect of different fuel compositions and fuel flow rates. The advanced geometry case (base case), with initial flow rate of 0.85 kg/s and composition given in Table. (3.1), is compared with one case with half the flow rate of the advanced geometry case (base case) and one case with pure decane as fuel. Radiation heat flux, logging point 7.

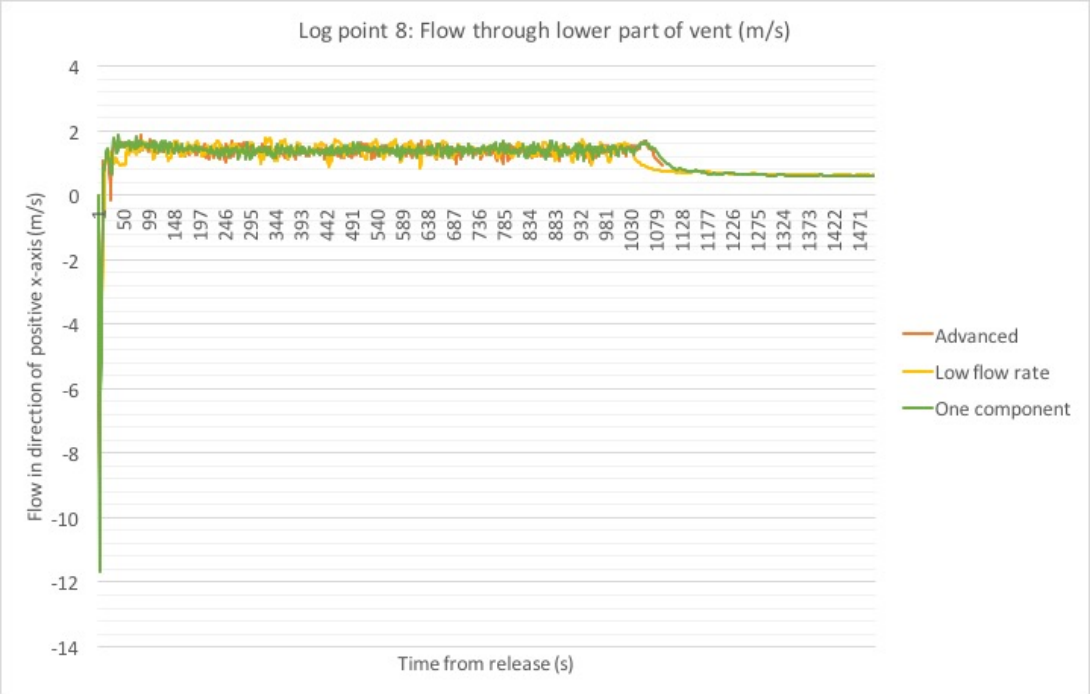

Figure 4.24: Investigation into the effect of different fuel compositions and fuel flow rates. The advanced geometry case (base case), with initial flow rate of 0.85 kg/s and composition given in Table. (3.1), is compared with one case with half the flow rate of the advanced geometry case (base case) and one case with pure decane as fuel. Flow rate at vent, logging point 8.

advanced geometry (base case) and the one-component cases.

4.4 Droplet size

For investigation of the effect of spray droplet sizes, three cases are compared. The first case is the advanced geometry case (base case) as described in Ch. (3). This case has droplet diameters calculated from Eq. (3.16), given in Table (3.2). For comparison of the effect of droplet diameters against this case, two cases, one with droplet diameters 5 times larger than the advanced geometry case (the large diameter case) and one with droplet diameters 1/5 th of the advanced geometry case (the small diameter case) were created. The large diameter and small diameter cases are identical to the advanced geometry case (base case), except for the change in droplet diameter.

Flame development

The three cases showed different flame distributions during the quasi-stable temperature time period. While the advanced geometry case (base case) had flames stretching from the fuel release point towards the east wall, the large diameter case had flames observed in the whole east half of the enclosure. For the small diameter case, the flame layer in the upper part of the enclosure, observed initially for all three cases, was maintained for the whole duration of the fuel release. Some positions with local extinction were observed close to the west wall, for the small diameter case.

Evaporation

As can be seen from the Figs. (4.25), (4.26) and (4.27), the spray distribution and evaporation depended on the droplet size. With larger droplet diameters, the droplets travel longer before full evaporation. For the largest droplet diameter, given in Fig. (4.25), the spray was seen impinging on the ceiling before all droplets evaporate. Due to the way sprays are modeled in KFX, all droplets impinging on the ceiling will be terminated, giving no rain of unevaporated droplets from the ceiling.

The advanced geometry case (base case), with droplet sizes as calculated by Eq. (3.16), given in Fig. (4.26), gave no impingement of droplets on the ceiling of the enclosure. All droplets were evaporated approximately 0.5-1 m before the flow reached the ceiling.

For the case with the smallest droplet size, given in Fig. (4.27), the evaporation of the droplets happened over a smaller distance. The spray was fully evaporated 1-2 m above the fuel release point. For every species of the composition, the number of numerical droplets that was released per second were 4000.

Temperatures

At logging point 1, given in Fig. (4.28), the temperatures recorded were similar for the advanced geometry case (base case) and the large diameter case. The small diameter case had a different temperature development than the two other cases. The temperatures recorded

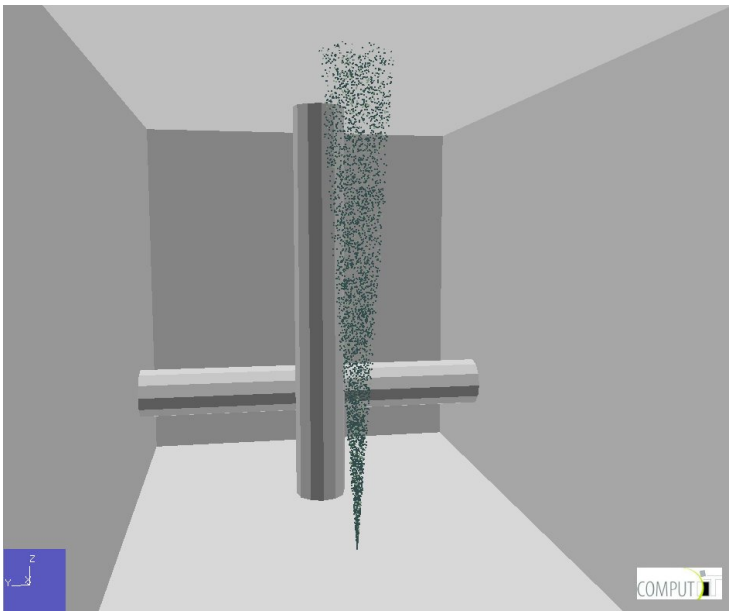

Figure 4.25: Investigation into the effect of fuel spray droplet size: Spray distribution inside enclosure for the large diameter case with 5 times the droplet diameter of the advanced geometry case (base case). The image is from 400 s after fuel release

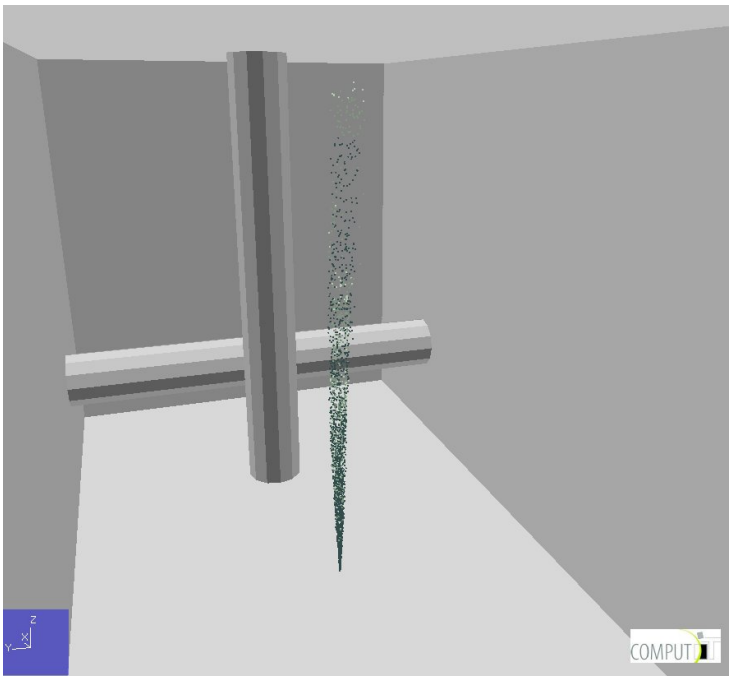

Figure 4.26: Investigation into the effect of fuel spray droplet size: Spray distribution inside enclosure for the advanced geometry case (base case) with droplet sizes given in Table. (3.2). The image is from 400 s after fuel release

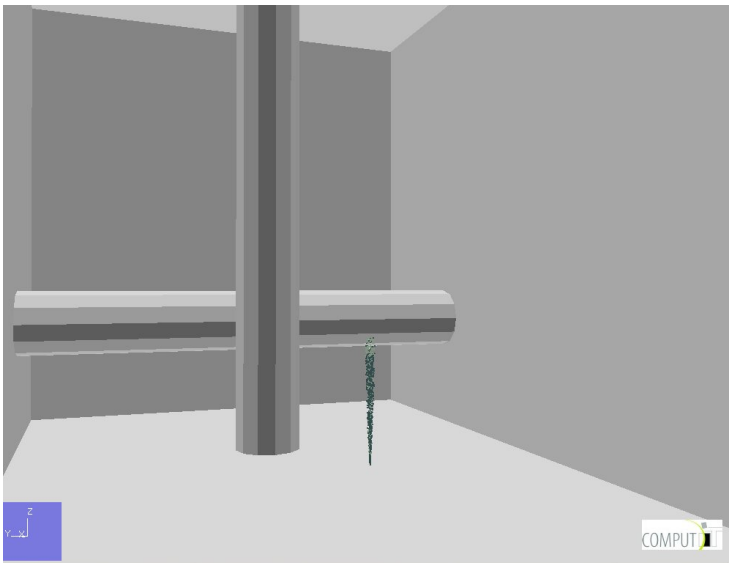

Figure 4.27: Investigation into the effect of fuel spray droplet size: Spray distribution inside enclosure for small diameter case with 1/5 th the droplet diameter of the advanced geometry case (base case). The image is from 400 s after fuel release

for the small diameter case at logging point 1, were approximately 200 K lower than the temperatures measured for the advanced geometry (base case) and the large diameter cases. It was also observed that the small diameter case had smaller temperature variations, at logging point 1, than the advanced geometry (base case) and large diameter cases.

The temperature differences between the advanced geometry (base case) and the large diameter cases were larger at logging point 2, given in Fig. (4.29), than at logging point 1. The temperatures recorded for the large diameter case were approximately 200 K higher than the advanced geometry case (base case). Both the advanced geometry (base case) and large diameter cases had larger temperature variations at logging point 2, compared to logging point 1. At the start of the simulation, high temperatures of above 1600 K were recorded for the advanced geometry (base case) and large diameter cases, before the temperatures decreased to quasi-stable temperatures. A small transient increase in temperatures was observed during the quasi-stable temperature time period, for all cases. The small diameter case had a much more stable transient temperature distribution, with lower initial temperatures and less variations than the advanced geometry (base case) and large diameter cases. The quasi-stable temperatures were higher for the small diameter case than for the advanced geometry (base case) and large diameter cases. As for the advanced geometry (base case) and large diameter cases, a small increase in temperatures was observed during the quasi-stable time period.

The temperature difference between the large diameter and the advanced geometry (base case) cases, observed at logging point 2, increased at logging point 3, given in Fig. (4.30). A decrease in temperature variations was observed for the advanced geometry case (base case), compared to what was observed at logging points 1 and 2. While the advanced geometry case (base case) had a large final increase in recorded temperatures, the large diameter case did not. The large diameter case had a gradual increase in temperatures from around

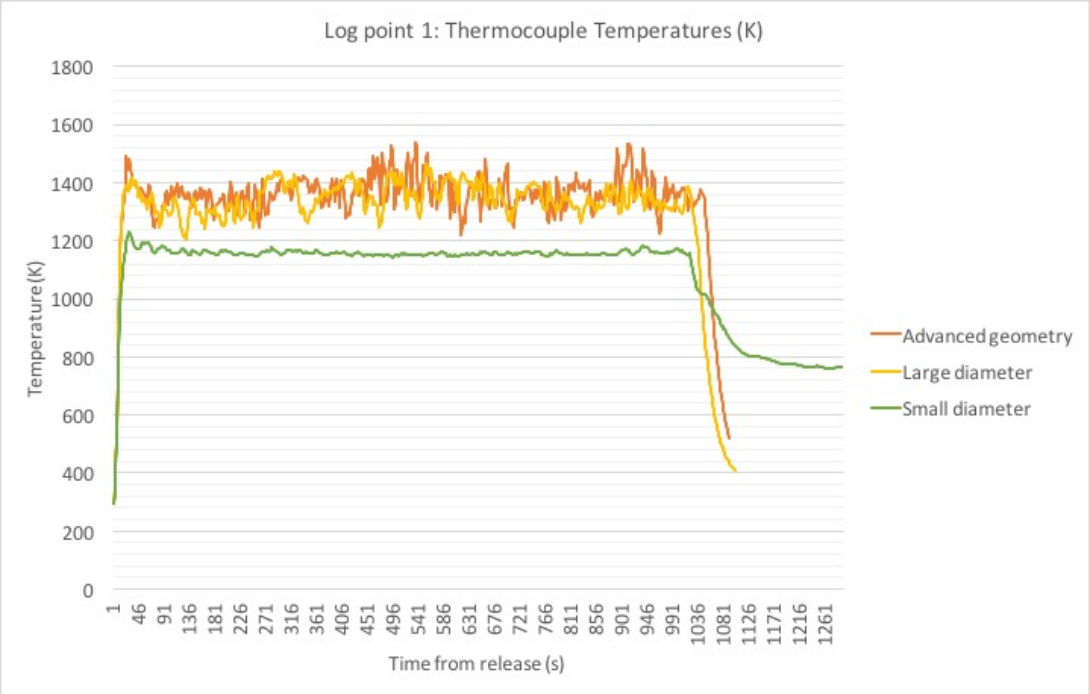

Figure 4.28: Investigation into the effect of fuel droplet size. The advanced geometry case (base case)(with droplet diameters given in Table. (3.2)) is compared to the large diameter case, with 5 times as large droplet diameter, and the small diameter case, with 1/5th the droplet diameter. thermocouple temperatures, logging point 1.

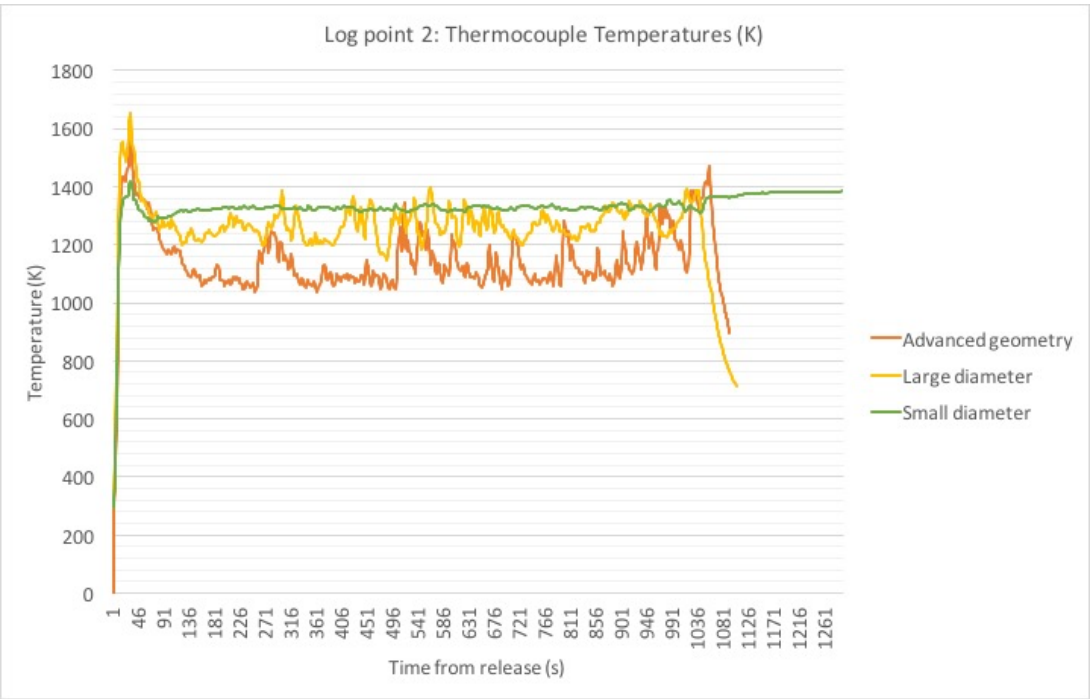

Figure 4.29: Investigation into the effect of fuel droplet size. The advanced geometry case (base case)(with droplet diameters given in Table. (3.2)) is compared to the large diameter case, with 5 times as large droplet diameter, and the small diameter case, with 1/5th the droplet diameter. thermocouple temperatures, logging point 2.

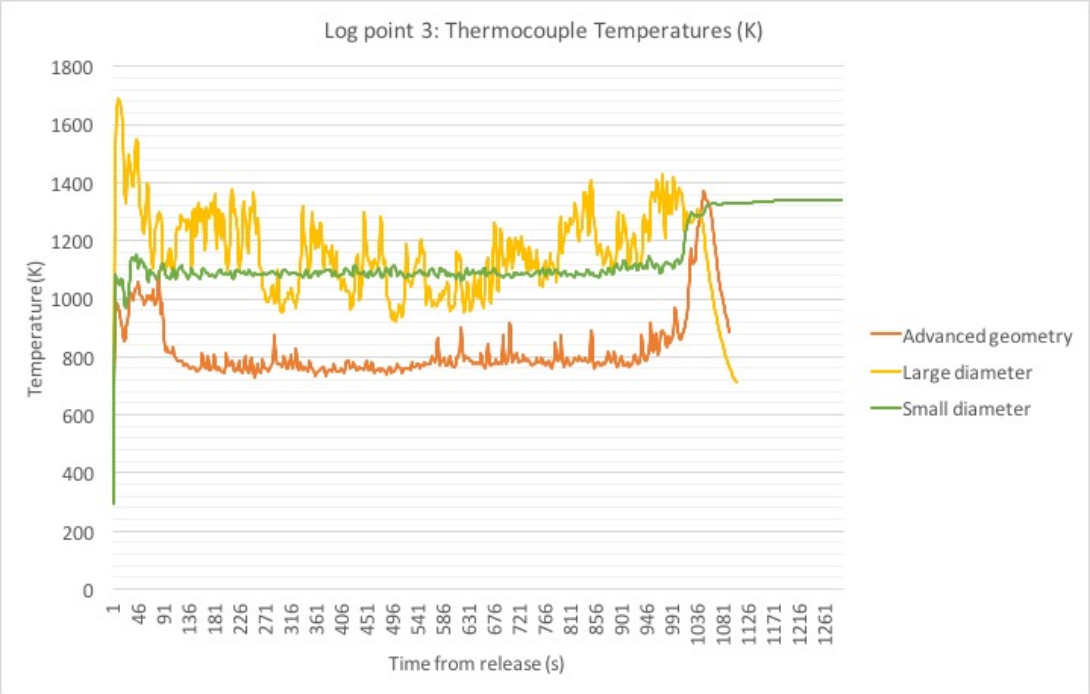

Figure 4.30: Investigation into the effect of fuel droplet size. The advanced geometry case (base case)(with droplet diameters given in Table. (3.2)) is compared to the large diameter case, with 5 times as large droplet diameter, and the small diameter case, with 1/5th the droplet diameter. thermocouple temperatures, logging point 3.

600 s after the fuel release starts, until the fuel release was stopped. As for logging point 2, the temperature distribution of the small diameter case had a different development compared to the advanced geometry (base case) and large diameter cases. The recorded variations of the small diameter case were smaller. Initially, the small diameter case had a more gradual temperature increase to quasi-stable temperatures, where the temperatures logged for the small diameter case were stable at approximately 1100 K. Interestingly, from the time when the fuel release was stopped, the small diameter case showed an increase in temperatures at logging point 3.

At logging point 4, given in Fig. (4.31), the large diameter case generally recorded slightly higher temperatures than the advanced geometry case (base case), with the small diameter generally recording the highest temperatures. As observed at the other thermocouple temperature logging points, stable temperatures and small temperature variations were recorded for the small geometry case. For the small diameter case, the same trend as seen in logging point 3, of increase in temperature when the fuel release was stopped, was witnessed at logging point 4.

Radiation heat flux

The logging of radiation heat fluxes showed similar trends as the logging of temperatures. At logging point 5, given in Fig. (4.32), the highest heat fluxes were recorded for the small diameter case. The heat fluxes recorded for the advanced geometry (base case) and large

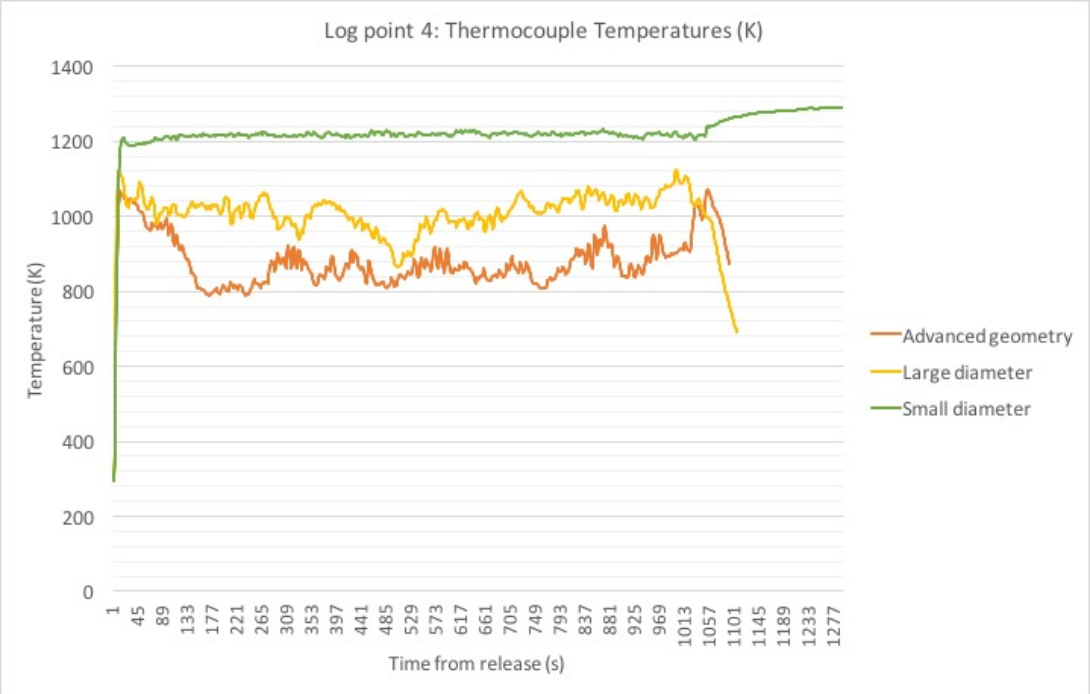

Figure 4.31: Investigation into the effect of fuel droplet size. The advanced geometry case (base case)(with droplet diameters given in Table. (3.2)) is compared to the large diameter case, with 5 times as large droplet diameter, and the small diameter case, with 1/5th the droplet diameter. thermocouple temperatures, logging point 4.

diameter cases were more similar, with more variations observed than at the small diameter case. When the fuel release was stopped, the heat fluxes recorded for the advanced geometry (base case) and large diameter cases decreased rapidly, while the small diameter case had a more gradual decrease in recorded radiation heat fluxes.

The recorded radiation heat fluxes were lower for all cases at logging point 6, given in Fig. (4.33), compared to logging point 5. Initially, all cases had a rapid increase in recorded radiation heat fluxes, before the recorded radiation heat fluxes decreased to a lower quasi-stable state. More variations were recorded for the large diameter case, compared to the small diameter and advanced geometry (base case) cases, during the quasi-stable time period. Compared to logging point 5, the variations recorded for the small diameter case increased at logging point 6. Towards the end of the simulation, all cases showed an increase in recorded radiation heat fluxes. The trend observed at logging point 5, of when the fuel release was stopped the recorded heat fluxes decreased more rapidly for the large diameter and the advanced geometry (base case) cases compared to the small diameter case, continued at logging point 6.

The recorded heat fluxes at logging point 7, given in Fig. (4.34), showed an increase in recorded heat fluxes for the small diameter case compared to logging point 6. The variations in the large diameter case were reduced at logging point 7 compared to logging point 6. Variations recorded in the advanced geometry case (base case) were higher at logging point 7 than at logging point 6. Similar magnitudes of radiation heat fluxes were recorded

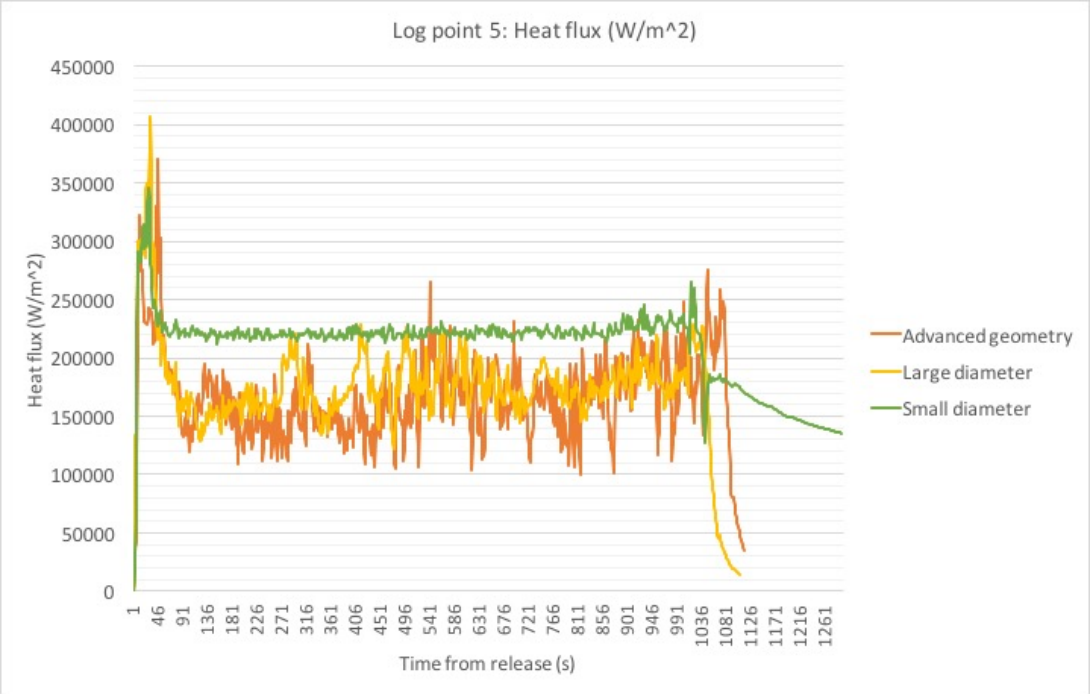

Figure 4.32: Investigation into the effect of fuel droplet size. The advanced geometry case (base case)(with droplet diameters given in Table. (3.2)) is compared to the large diameter case, with 5 times as large droplet diameter, and the small diameter case, with 1/5th the droplet diameter. radiation heat flux, logging point 5.

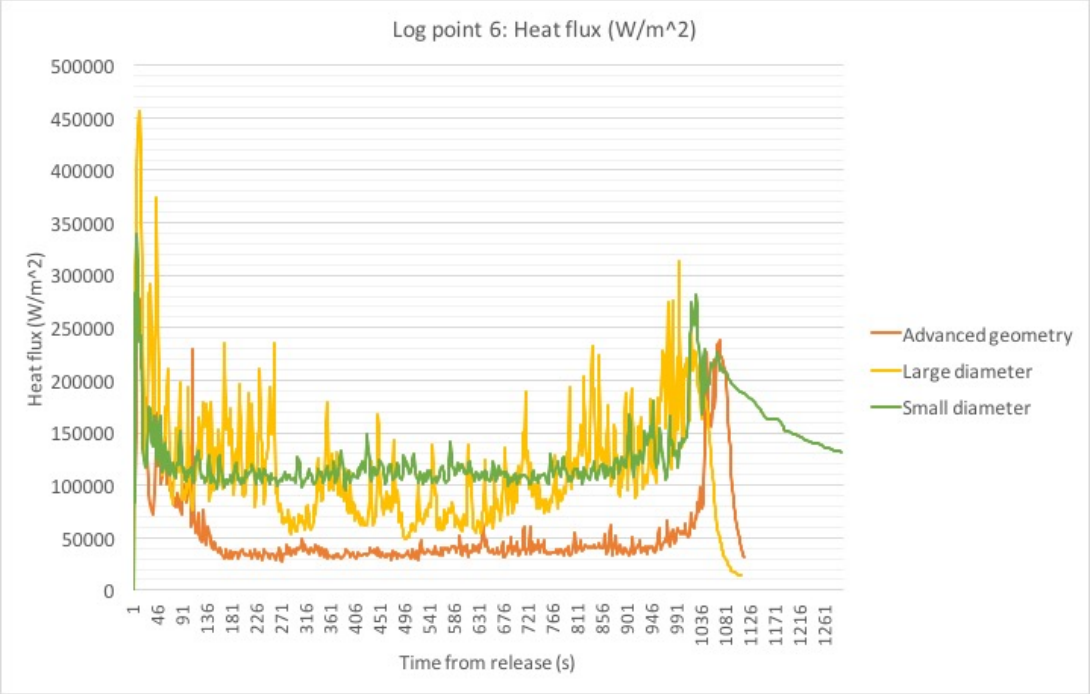

Figure 4.33: Investigation into the effect of fuel droplet size. The advanced geometry case (base case)(with droplet diameters given in Table. (3.2)) is compared to the large diameter case, with 5 times as large droplet diameter, and the small diameter case, with 1/5th the droplet diameter. radiation heat flux, logging point 6

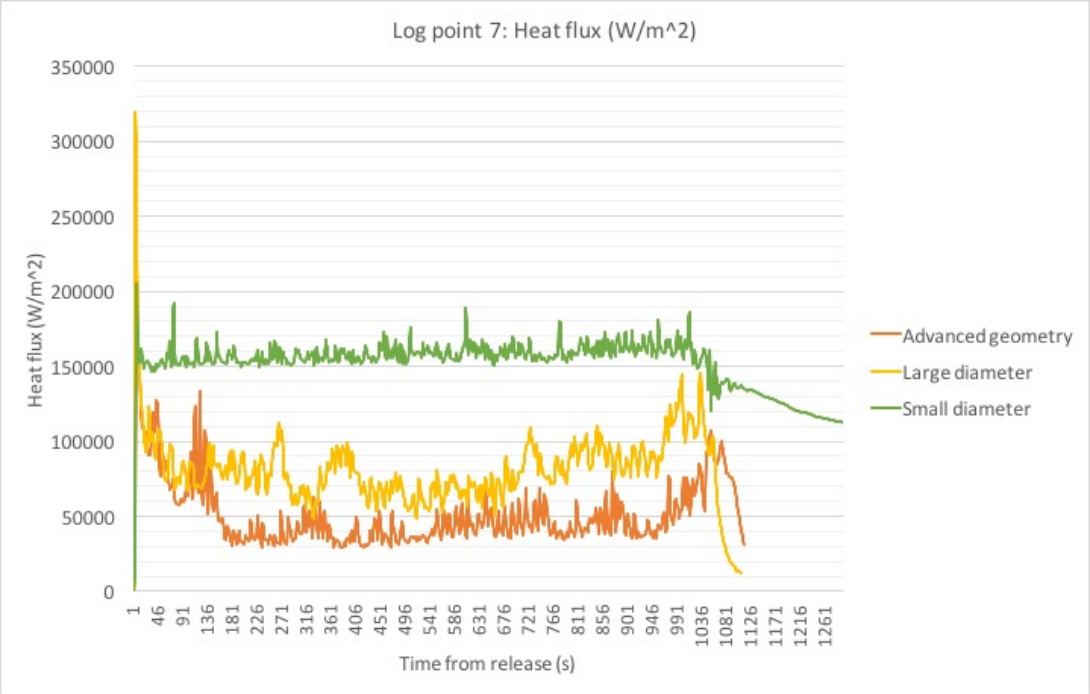

Figure 4.34: Investigation into the effect of fuel droplet size. The advanced geometry case (base case)(with droplet diameters given in Table. (3.2)) is compared to the large diameter case, with 5 times as large droplet diameter, and the small diameter case, with 1/5th the droplet diameter. radiation heat flux, logging point 7

at logging points 6 and 7 for the advanced geometry (base case) and large diameter cases. The advanced geometry (base case) and large diameter cases recorded a larger increase in radiation heat fluxes than the small diameter case, before the fuel release was stopped. As for logging points 5 and 6, the heat flux decreased more rapidly for the large diameter and advanced geometry (base case) cases when the fuel release was stopped, compared to the small diameter case.

Air inside the compartment

For logging of oxygen quantity inside the enclosure, transient development in the quasi-steady temperature time period was observed. As seen in Fig. (4.35), the inflow recorded for the advanced geometry (base case), large diameter and small diameter cases were very similar. The logging of oxygen quantity inside the enclosure at the z=0.3 m plane revealed some differences between the cases. The large diameter case showed similar development as the advanced geometry case (base case), with the oxygen fluttering between the north and south wall, but the distance the oxygen travelled into the compartment, was observed to vary more for the large diameter case. Oxygen, of approximately atmospheric quantities, was observed to reach 5-9 m into the compartment, measured from the vent, compared to 5-7 m for the advanced geometry case (base case). For the small diameter case oxygen, was observed to reach further into the compartment than for the advanced geometry (base case) and large diameter cases, with oxygen, of approximately atmospheric quantities, reaching

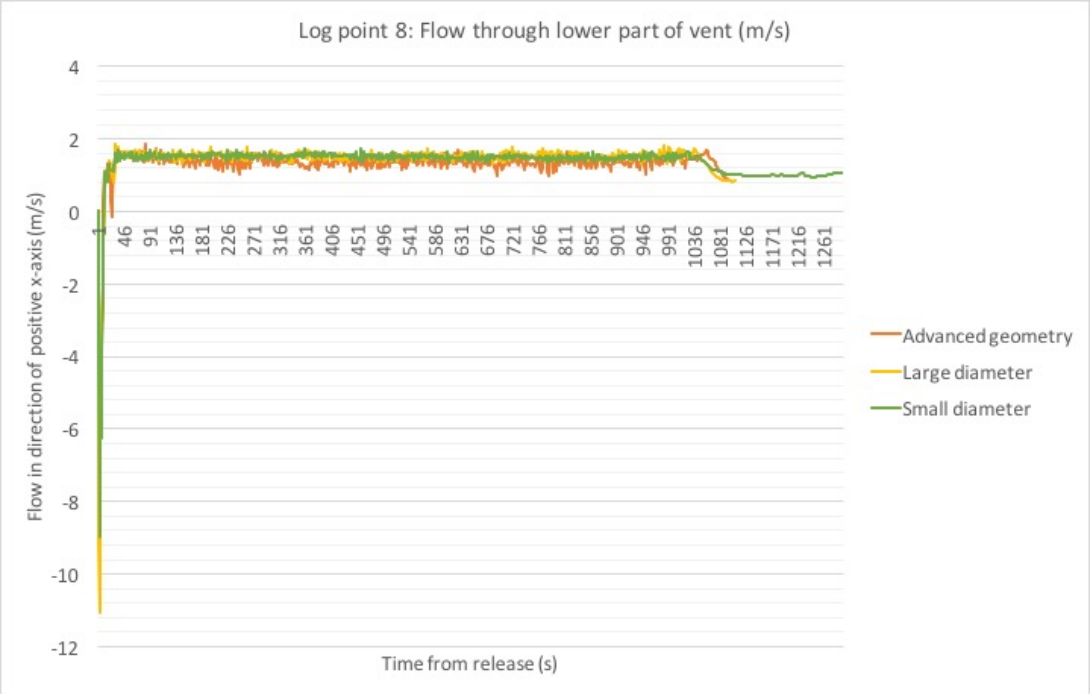

Figure 4.35: Investigation into the effect of fuel droplet size. The advanced geometry case (base case)(with droplet diameters given in Table. (3.2)) is compared to the large diameter case, with 5 times as large droplet diameter, and the small diameter case, with 1/5th the droplet diameter. vent flow, logging point 8

9-11 m into the compartment, measured from the vent. The position of the oxygen was also observed to be more stable for the small diameter case, with no change in flow direction and no flickering between the walls, as were observed for the advanced geometry (base case) and large diameter cases.

4.5 Dispersion angle

For investigating the effect the spray dispersion angle has on flame development, three cases are compared. The first case is the advanced geometry case (base case), which has a dispersion angle of 10°, the second case is a case with a dispersion angle of 5° (the small dispersion angle case), and the third case is a case with a dispersion angle of 20° (the large dispersion angle case).

Flame behaviour

The large and small dispersion angle cases had similar flame development as observed for the advanced geometry case (base case) in Sec. (4.1). An initial period where the flame fills the upper part of the enclosure was observed. The initial period was followed by flame extinction close to the west wall of the enclosure, moving the flame towards the east wall and the vent of the enclosure. An external flame was observed flowing out of the vent and up along the outside of the east wall. The internal flame enclosed the upper parts of the vent

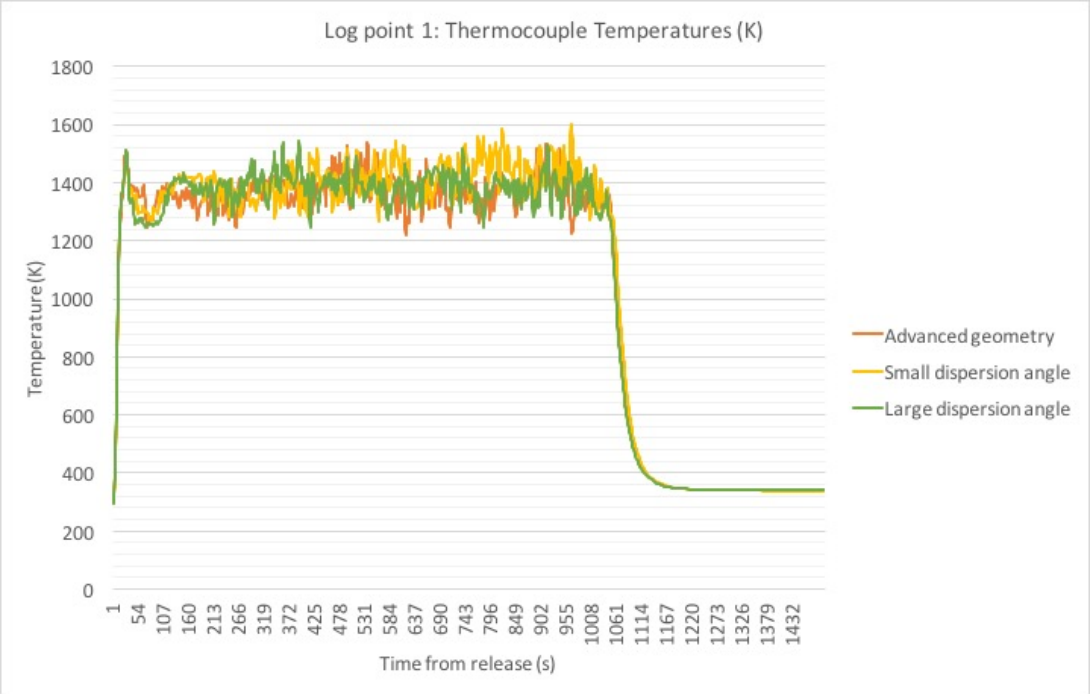

Figure 4.36: Investigation into the effect of the fuel spray dispersion angle. The advanced geometry case (base case), with fuel spray dispersion angle of 10°, is compared to the large dispersion angle case, with fuel spray dispersion angle of 20°, and the small dispersion angle case, with fuel spray dispersion angle of 5°. thermocouple temperatures, logging point 1.

and east wall. From approximately 120 s quasi-stable flames were observed flowing out of the vent and in the east part of the enclosure. The flames stretched from the fuel release point towards the east wall and out of the vent, and spanned to the north and south walls.

Temperatures

As can be seen from the logging points, given in Figs. (4.36), (4.37), (4.38) and (4.39), the recorded temperatures were very similar for the three cases. At logging point 1, given in Fig. (4.36), the small dispersion angle case had a slightly higher temperature increase during the quasi-stable temperature period, compared to the advanced geometry (base case) and large dispersion angle cases.

At logging point 2 and 3, given in Figs. (4.37) and (4.38), very similar temperature developments were observed among the cases. All the cases recorded high temperatures initially, followed by a temperature decrease to a quasi-stable temperature time period. At logging point 3, all cases recorded lower temperature variations than what was recorded at logging point 2. A sharp increase in recorded temperatures was recorded finally, at logging point 3. During the transient logging of temperatures at logging points 2 and 3 the large dispersion angle case generally recorded slightly higher temperatures than the advanced geometry (base case) and small dispersion angle cases. At logging point 4, given in Fig. (4.39), the logged thermocouple temperature distributions were very similar for the three cases.

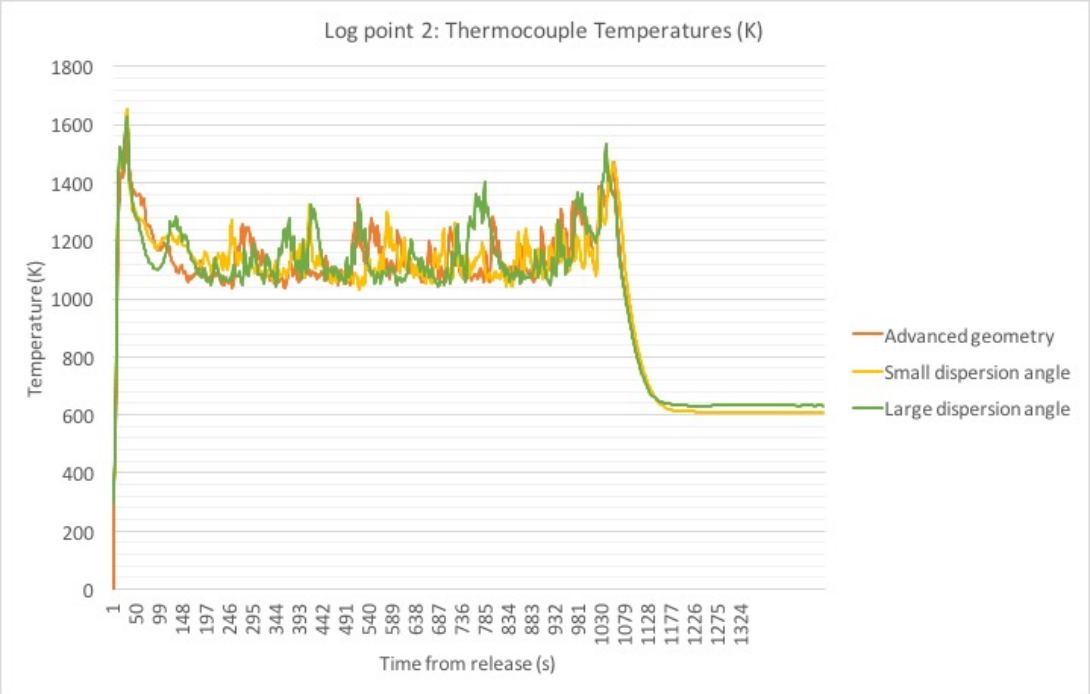

Figure 4.37: Investigation into the effect of the fuel spray dispersion angle. The advanced geometry case (base case), with fuel spray dispersion angle of 10°, is compared to the large dispersion angle case, with fuel spray dispersion angle of 20°, and the small dispersion angle case, with fuel spray dispersion angle of 5°. thermocouple temperatures, logging point 2.

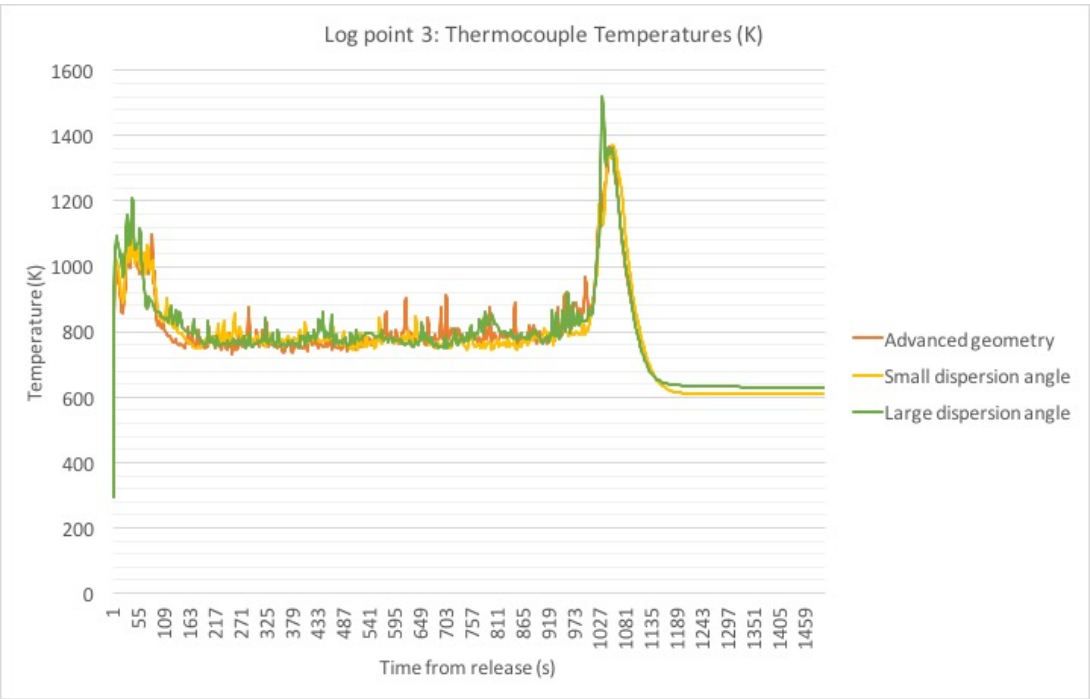

Figure 4.38: Investigation into the effect of the fuel spray dispersion angle. The advanced geometry case (base case), with fuel spray dispersion angle of 10°, is compared to the large dispersion angle case, with fuel spray dispersion angle of 20°, and the small dispersion angle case, with fuel spray dispersion angle of 5°. thermocouple temperatures, logging point 3.

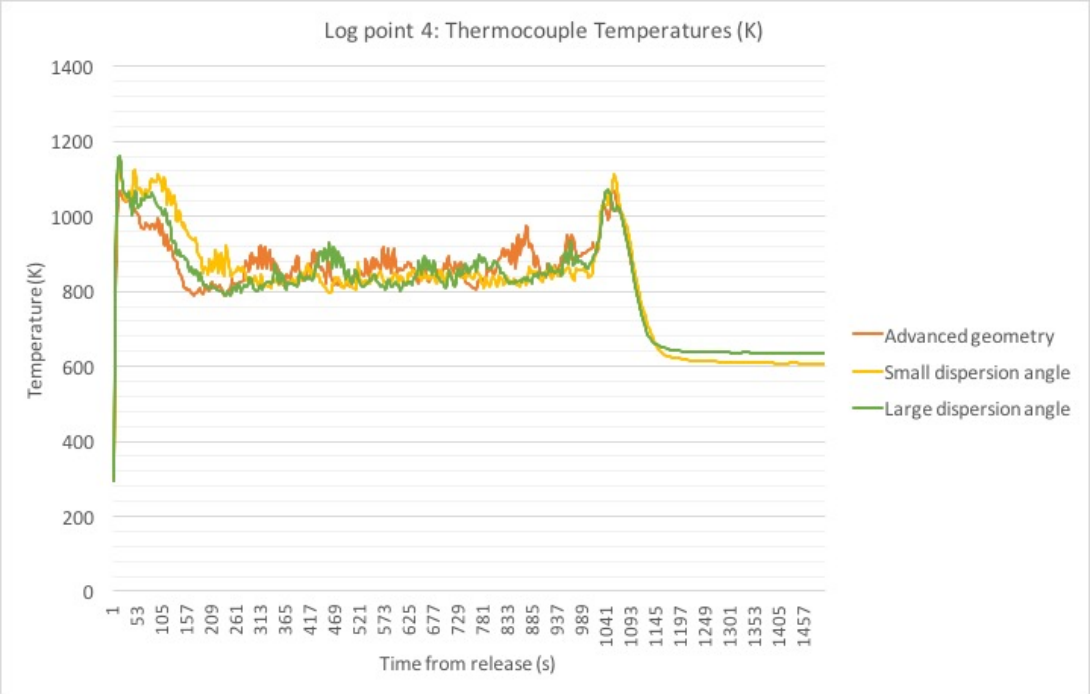

Figure 4.39: Investigation into the effect of the fuel spray dispersion angle. The advanced geometry case (base case), with fuel spray dispersion angle of 10°, is compared to the large dispersion angle case, with fuel spray dispersion angle of 20°, and the small dispersion angle case, with fuel spray dispersion angle of 5°. thermocouple temperatures, logging point 4.

Radiation heat flux

The logging of radiation heat fluxes, given in Figs. (4.40), (4.41) and (4.42) showed similar trends as observed for the logging of thermocouple temperatures. All three cases recorded very similar radiation heat fluxes at all logging points. At logging points 6 and 7, high initial heat fluxes were recorded initially, before a decrease to lower quasi-steady heat fluxes. This quasi-steady time period lasted approximately until the fuel release was stopped. A large increase in radiation heat fluxes was observed finally, at logging point 6, and a slightly smaller final increase was observed at logging point 7. Significantly higher variations in recorded radiation heat fluxes were observed at logging point 5, for all cases, compared to at logging points 6 and 7.

Oxygen inside the compartment

The oxygen quantity at the inside of the enclosure was logged at the z=0.3 m plane, while inflow into the compartment was measured at logging point 8. Regarding oxygen distribution at the inside of the compartment, the large and small dispersion angle cases showed similar distributions as the advanced geometry case (base case), where the oxygen was seen to enter 5-7 m into the compartment, measured from the vent. Similar values for inflow into the compartment were measured at logging point 8, given in Fig. (4.43). The oxygen flow was observed to flutter in the y-direction, moving between the north wall and the south wall of

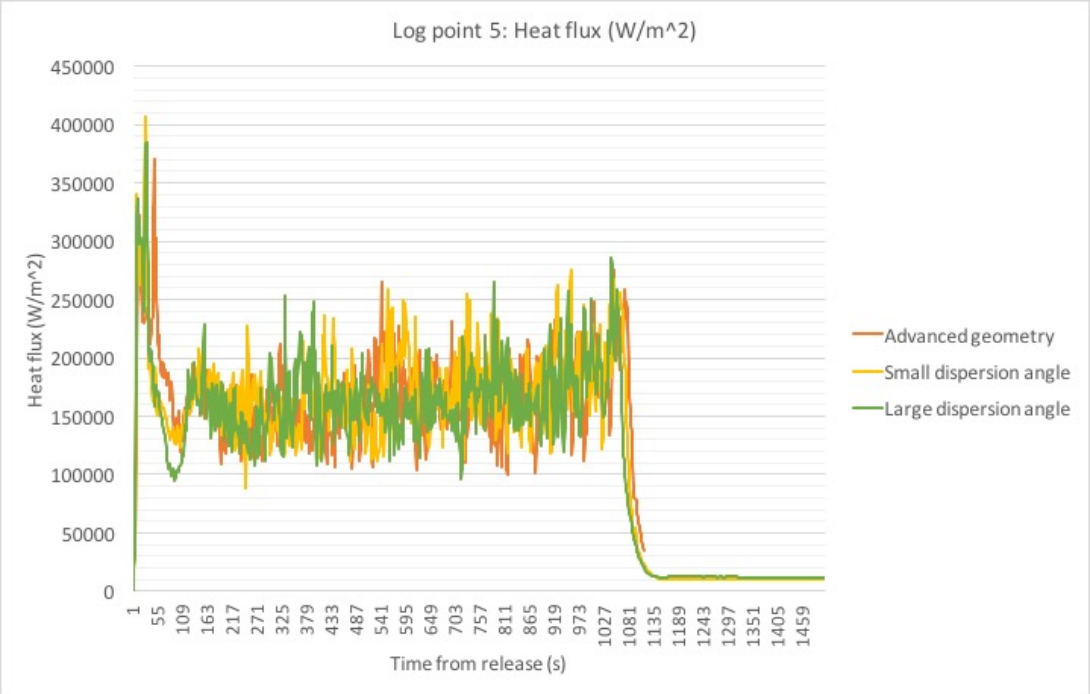

Figure 4.40: Investigation into the effect of the fuel spray dispersion angle. The advanced geometry case (base case), with fuel spray dispersion angle of 10°, is compared to the large dispersion angle case, with fuel spray dispersion angle of 20°, and the small dispersion angle case, with fuel spray dispersion angle of 5°. Radiation heat flux, logging point 5.

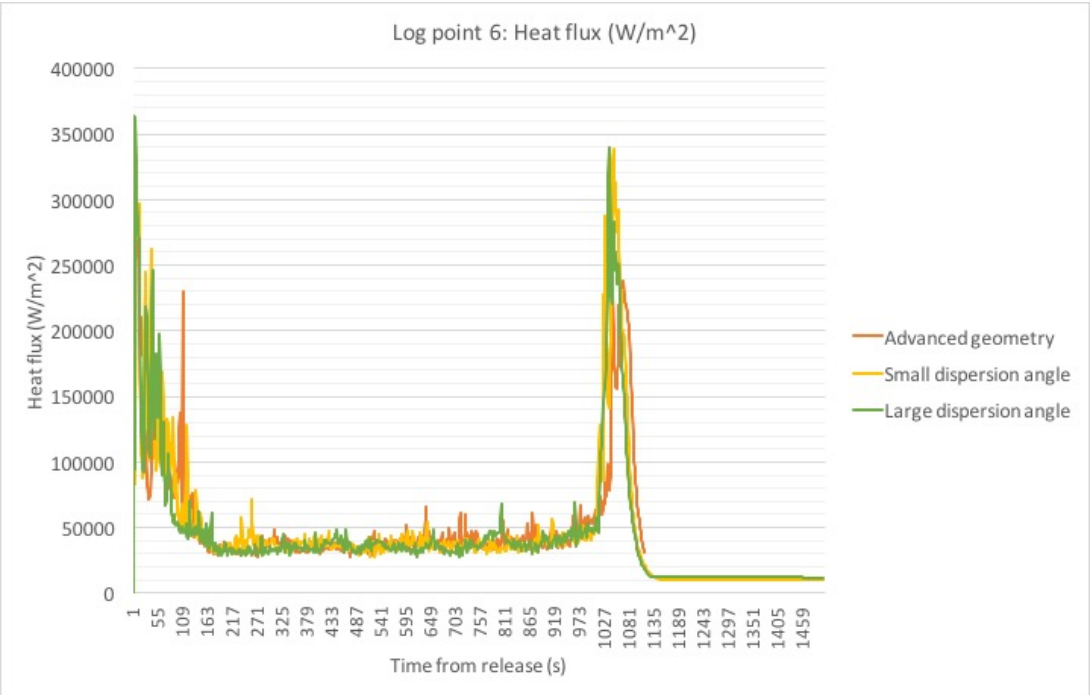

Figure 4.41: Investigation into the effect of the fuel spray dispersion angle. The advanced geometry case (base case), with fuel spray dispersion angle of 10°, is compared to the large dispersion angle case, with fuel spray dispersion angle of 20°, and the small dispersion angle case, with fuel spray dispersion angle of 5°. Radiation heat flux, logging point 6.

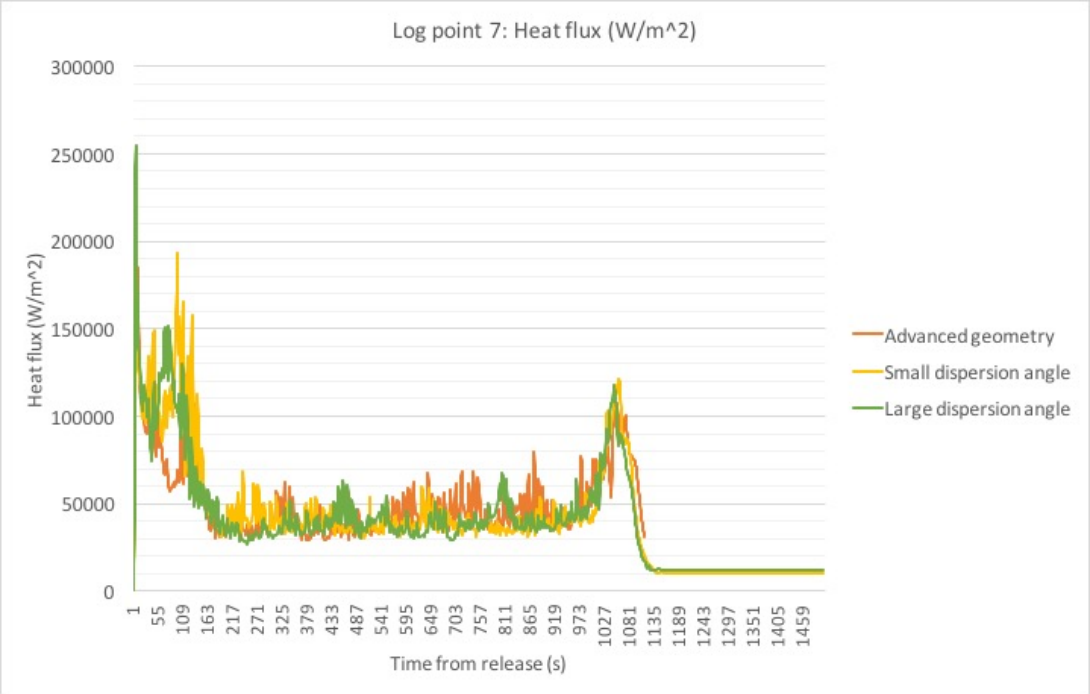

Figure 4.42: Investigation into the effect of the fuel spray dispersion angle. The advanced geometry case (base case), with fuel spray dispersion angle of 10°, is compared to the large dispersion angle case, with fuel spray dispersion angle of 20°, and the small dispersion angle case, with fuel spray dispersion angle of 5°. Radiation heat flux, logging point 7.

the compartment.

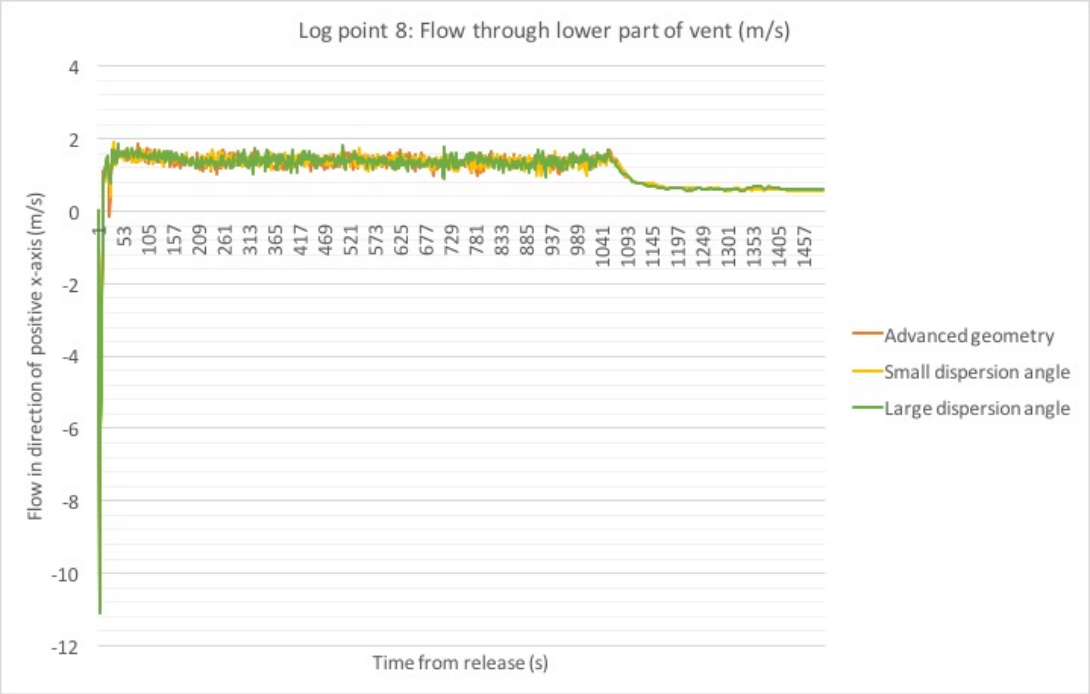

Figure 4.43: Investigation into the effect of the fuel spray dispersion angle. The advanced geometry case (base case), with fuel spray dispersion angle of 10°, is compared to the large dispersion angle case, with fuel spray dispersion angle of 20°, and the small dispersion angle case, with fuel spray dispersion angle of 5°. Vent flow, logging point 8.

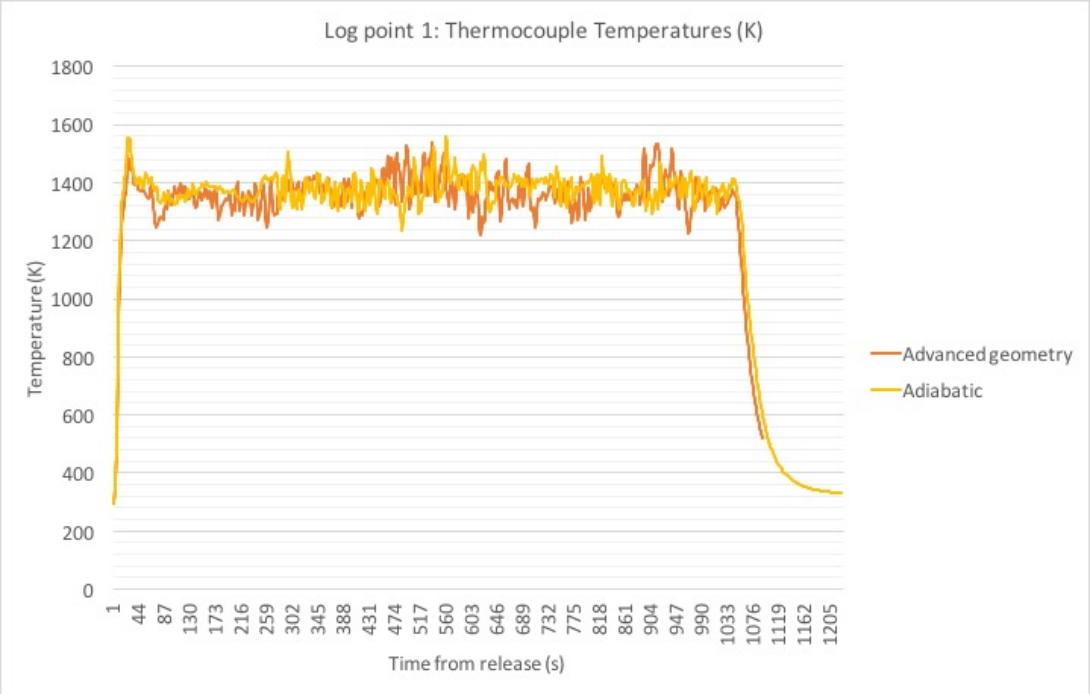

Figure 4.44: Investigation into the effect of increased compartment insulation. The advanced geometry case (base case), with K=0.161 W/mK, is compared against the adiabatic case, with K=10^{-6} W/mK. thermocouple temperatures, logging point 1

4.6 Insulation

For investigation of the effect of heat transfer through the walls of the enclosure, two cases are compared with different material heat conductivities, K (W/mK). The first case is the advanced geometry case (base case) (K=0.161 W/mK), described in Ch. (3). The second case is identical to the advanced geometry case (base case), except with K changed to 10^{-6} W/mK (the adiabatic case).

Flame behaviour

Both the adiabatic case and the advanced geometry case (base case) showed similar flame development. The initial flame development was as described in Sec. (4.1). After approximately 120 s after start of fuel release, a quasi-stable flame was observed. The flame was observed at a boundary positioned approximately from the fuel release point towards the east wall of the enclosure and spanned to the north and south walls, enclosing the upper parts of the vent and east wall. On the west side of the boundary, fuel was observed, and on the east side of the boundary, air was observed.

Temperatures inside the enclosure

At logging point 1, given in Fig. (4.44), the two cases showed very similar transient temperature distributions. Both cases had a sharp initial temperature increase, before reaching

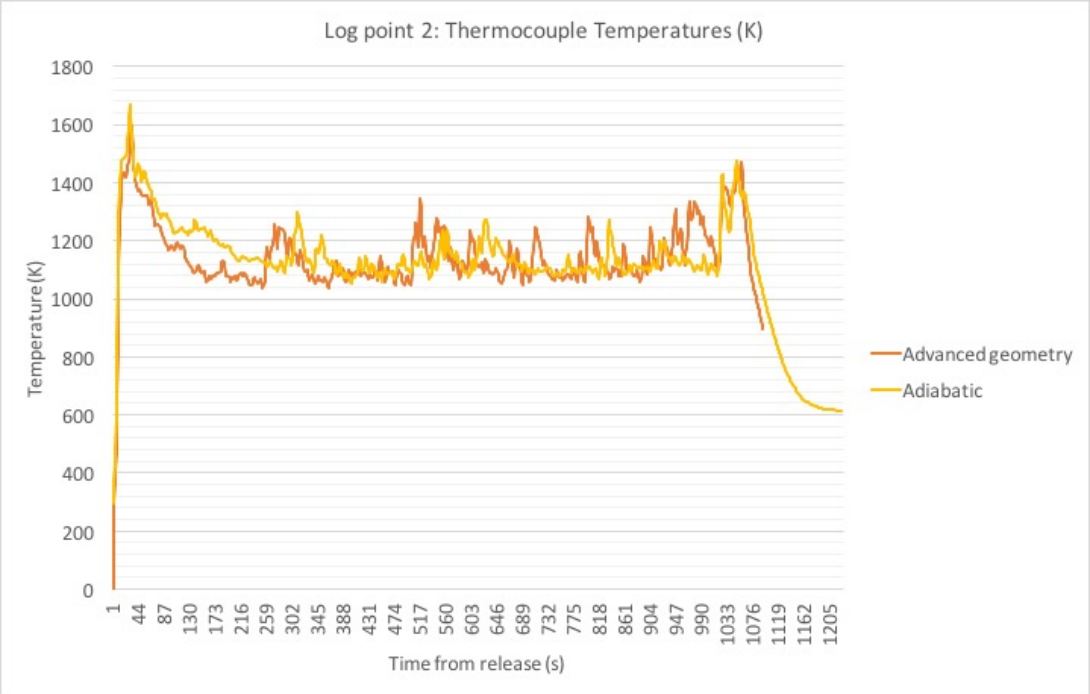

Figure 4.45: Investigation into the effect of increased compartment insulation. The advanced geometry case (base case), with K=0.161 W/mK, is compared against the adiabatic case, with K=10^{-6} W/mK. thermocouple temperatures, logging point 2

quasi-stable temperatures of approximately 1300-1400 K. The cases had some temperature variations during the quasi-stable time period. When the fuel release was stopped, the temperatures at logging point 1 decreased quickly, reaching ambient temperatures.

At logging point 2, given in Fig. (4.45), the two cases showed very similar transient temperature development, as also observed at logging point 1, but the temperatures recorded at logging point 2 were approximately 200 K lower than the temperatures recorded at logging point 1. Towards the end of the simulation, before the fuel release was stopped, an increase in temperatures was recorded for both cases.

The temperatures recorded at logging point 3, given in Fig. (4.46), showed a small difference between the two cases, with the temperatures of the adiabatic case being slightly higher. Compared to logging point 2, the temperatures were approximately 300 K lower. Both cases had a similar transient development, with less temperature variations during the quasi-stable temperature time period than observed at logging point 1 and 2. As for logging point 2, both cases recorded an increase in temperatures, before the fuel release was stopped. At this increase, the adiabatic case reached higher temperatures than the advanced geometry case (base case).

The quasi-stable temperatures recorded at logging point 4, given in Fig. (4.47), were higher than the quasi-stable temperatures reached at logging point 3. Although the temperature variations at logging point 4 were similar to logging point 3, the variations in temperatures recorded during the quasi-stable temperature period were bigger at logging point 4. Both cases showed a small temperature increase during the quasi-stable temperature time

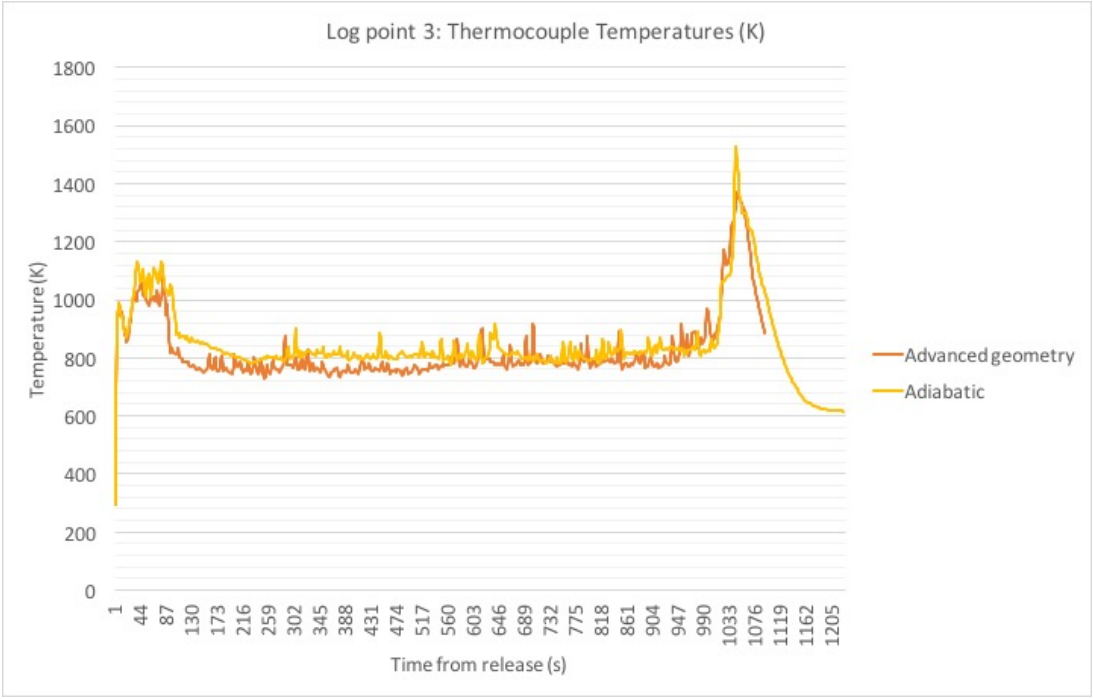

Figure 4.46: Investigation into the effect of increased compartment insulation. The advanced geometry case (base case), with K=0.161 W/mK, is compared against the adiabatic case, with K=10^{-6} W/mK. thermocouple temperatures, logging point 3

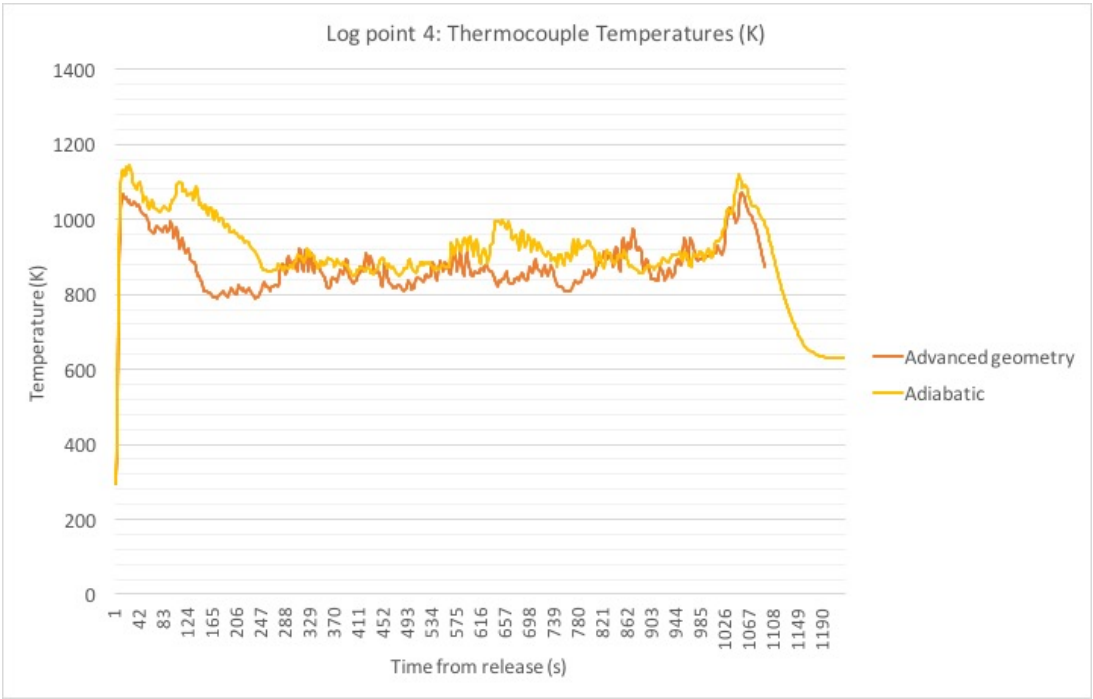

Figure 4.47: Investigation into the effect of increased compartment insulation. The advanced geometry case (base case), with K=0.161 W/mK, is compared against the adiabatic case, with K=10^{-6} W/mK. thermocouple temperatures, logging point 4

period, culminating to a temperature of approximately 1100 K, before the fuel release was stopped.

Wall temperatures

The adiabatic case recorded higher maximum wall temperatures than the advanced geometry case (base case) on the inside of the enclosure walls. Maximum temperatures of approximately 1700 K were logged for the adiabatic case, with stable temperatures between 1000 K and 1500 K logged at the east side of the the compartment and temperatures of 800 K logged at the west side of the compartment. Large transient temperature variations were logged on the inside surface of the enclosure walls. The inside wall temperatures recorded for the advanced geometry case (base case) were more uniform, with less spatial variations than the adiabatic case. Stable temperatures of approximately 280 K were logged on the outside wall surfaces of the compartment.

Radiation heat flux

The logged radiation heat fluxes close to the ceiling of the enclosure, given in Figs. (4.48), (4.49) and (4.50), showed a similar trend as the logging of temperatures. The differences in recorded radiation heat flux between the adiabatic and advanced geometry case (base case), were larger close to the west wall than close to the east wall. At logging points 5 and 7 larger variations in radiation heat fluxes were recorded than at logging point 6. Sharp increases and decreases in radiation heat fluxes were recorded at logging points 6 and 7, both initially and finally.

Oxygen in the compartment

Regarding inflow, given in Fig. (4.51), and oxygen quantity, measured at the z=0.3 m plane, the advanced geometry (base case) and the adiabatic cases were very similar. The oxygen content at the inside of the enclosure was observed during the quasi-stable temperature time period. Both cases recorded oxygen reaching 5-7 m into the compartment, and for both cases, the oxygen was observed to flutter between the south and north walls inside the compartment.

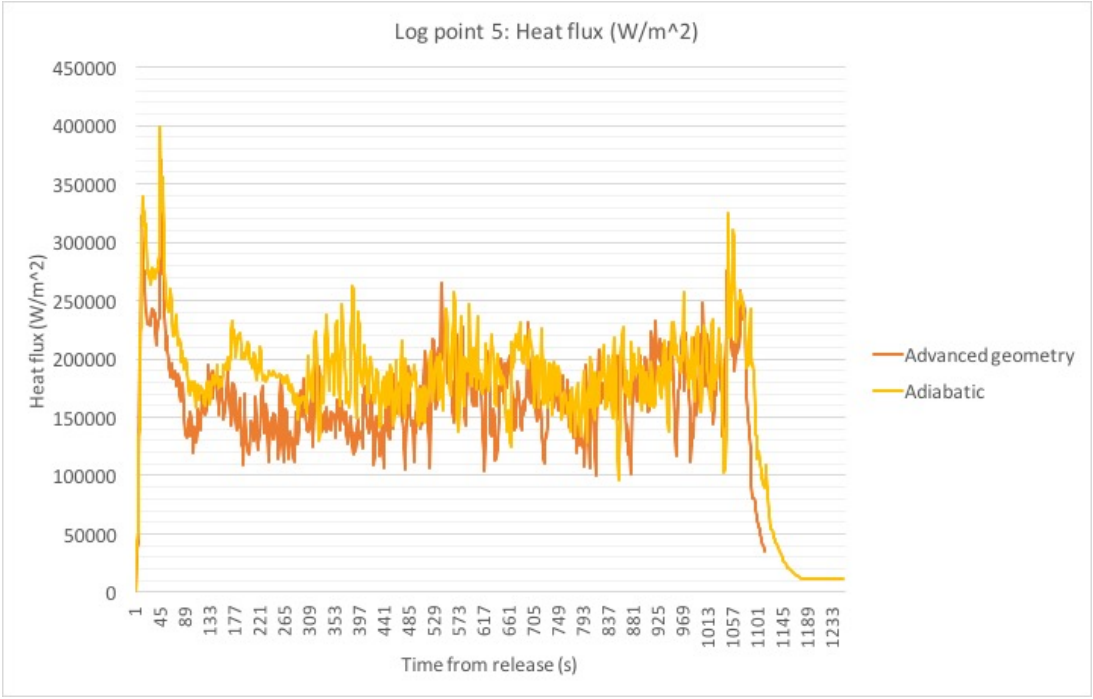

Figure 4.48: Investigation into the effect of increased compartment insulation. The advanced geometry case (base case), with K=0.161 W/mK, is compared against the adiabatic case, with K=10^{-6} W/mK. radiation heat flux, logging point 5

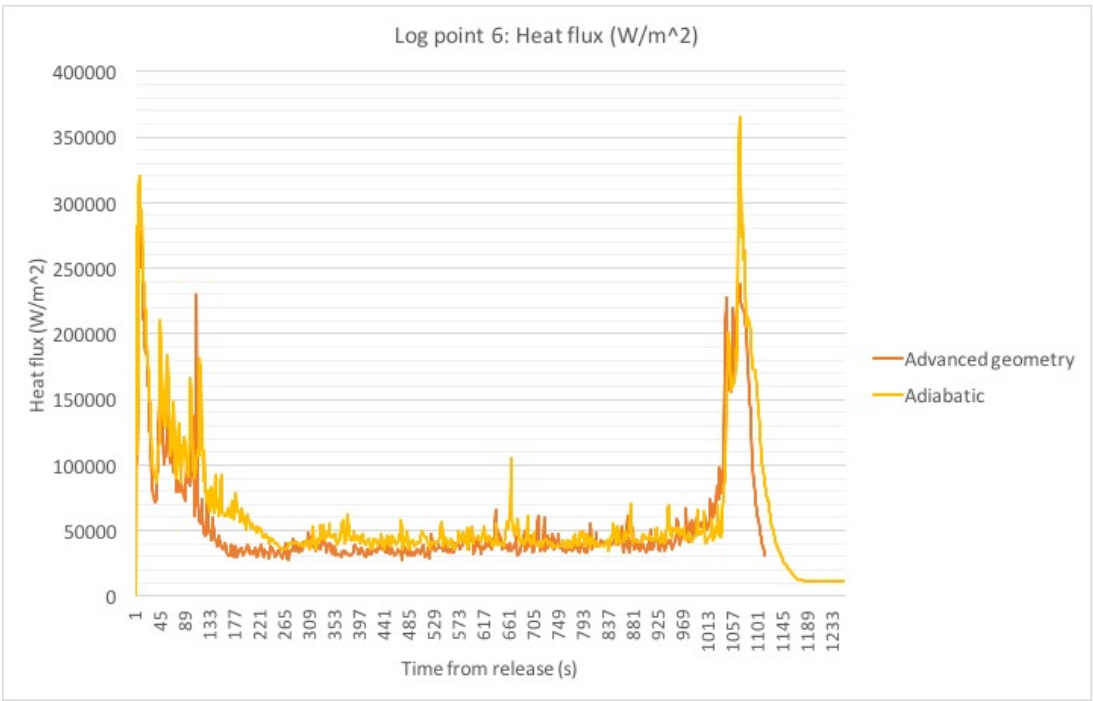

Figure 4.49: Investigation into the effect of increased compartment insulation. The advanced geometry case (base case), with K=0.161 W/mK, is compared against the adiabatic case, with K=10^{-6} W/mK. radiation heat flux, logging point 6

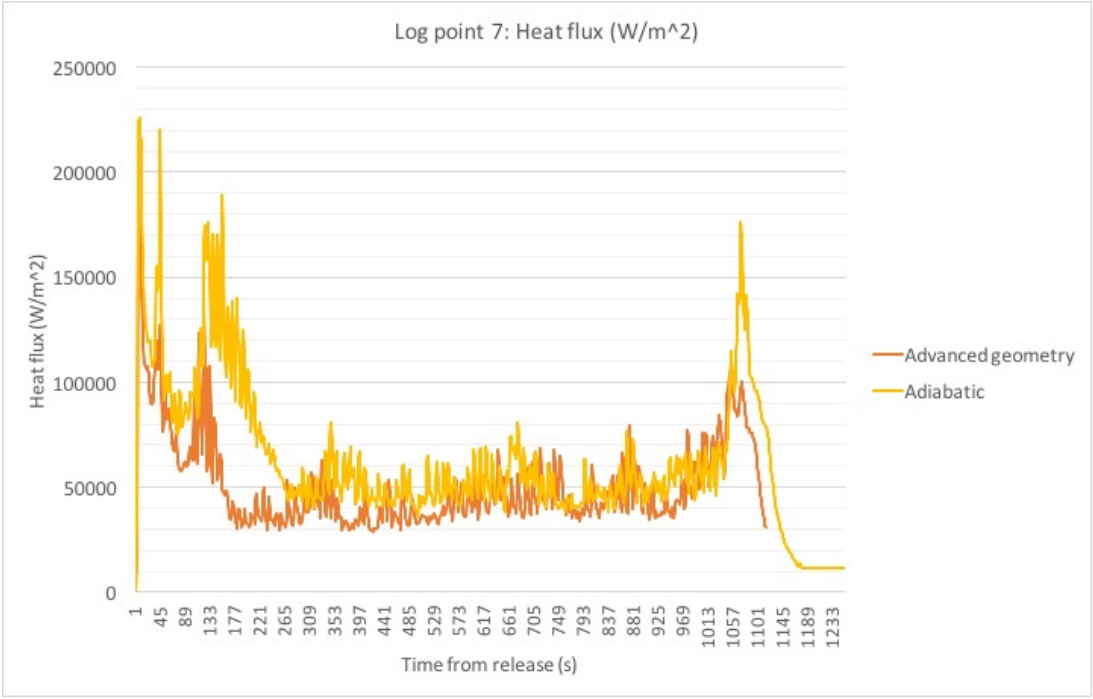

Figure 4.50: Investigation into the effect of increased compartment insulation. The advanced geometry case (base case), with K=0.161 W/mK, is compared against the adiabatic case, with K=10^{-6} W/mK. radiation heat flux, logging point 7

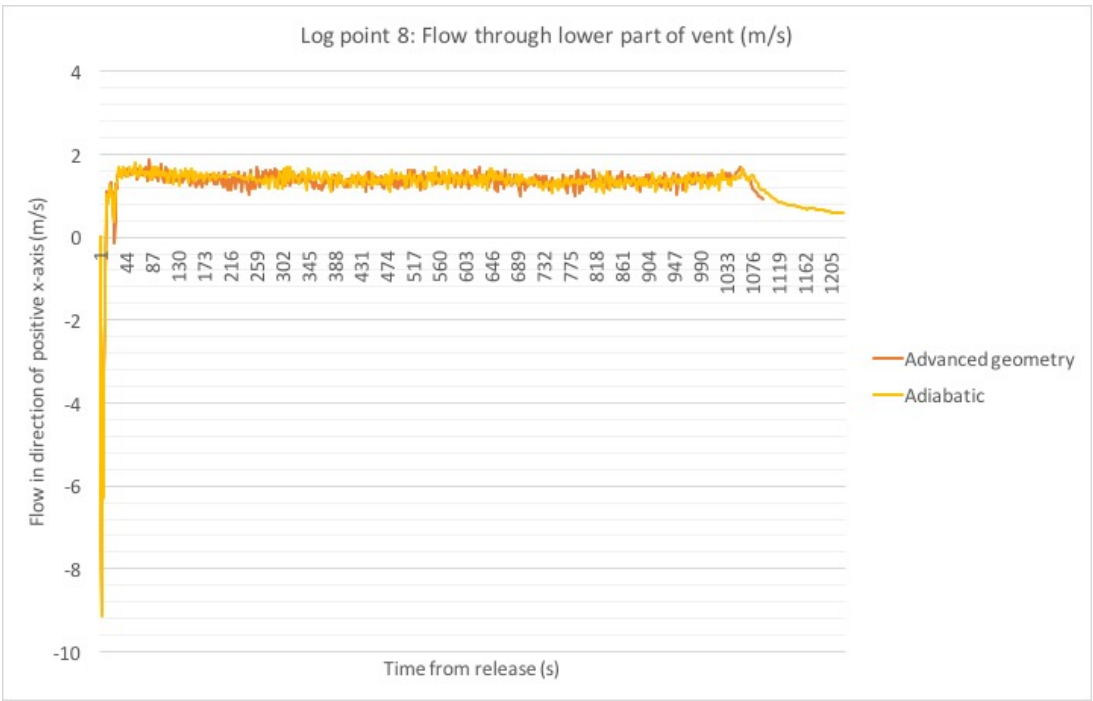

Figure 4.51: Investigation into the effect of increased compartment insulation. The advanced geometry case (base case), with K=0.161 W/mK, is compared against the adiabatic case, with K=10^{-6} W/mK. vent flow, logging point 8

4.7 Size of ventilation opening

For investigation on the effect the inflow and outflow through the vent of the compartment, have on the simulation, two cases are compared with different vent sizes. The first case is the advanced geometry case (base case). The second case is based on the advanced geometry case (base case), but with an increase in vent area of approximately 7.8 m^2 (the big vent case).

Flame development

The big vent case showed a different flame development inside the enclosure than what was observed for the advanced geometry case (base case). While both cases had a similar initial development, as described in Sec. (4.1), the big vent case maintained the upper layer flame, when extinction in the upper layer was observed for the advanced geometry case (base case).

Temperatures

The size of the ventilation opening showed to have significant effects on the temperatures recorded on the inside of the enclosure. At logging point 1, given in Fig. (4.52), the recorded temperatures of the big vent and the advanced geometry (base case) cases, were similar in magnitude. Quasi-stable temperatures of approximately 1300 K were recorded for both cases. The final temperature decrease, after the fuel flow was stopped, was observed earlier for the big vent case than for the advanced geometry case (base case). Interestingly, the temperatures recorded for the advanced geometry case (base case) varied much more than what was recorded for the big vent case. The big vent case had a very stable temperature distribution at logging point 1.

At logging point 2, given in Fig. (4.53), large temperature differences between the advanced geometry (base case) and the big vent cases, were recorded. The big vent case generally recorded approximately 400-500 K higher temperatures than the advanced geometry case (base case), during the quasi-stable temperature time period. As observed at logging point 1, the big vent case had a more stable temperature distribution, while the advanced geometry case (base case) recorded more temperature variations. Towards the end of the simulation, the advanced geometry case (base case) had an increase in recorded temperatures, while the big vent case recorded stable temperatures of approximately 1600 K, without the final increase in temperatures. The trend of an earlier final temperature decrease in the big vent case, was observed in all logging points recording thermocouple temperatures.

At logging point 3, given in Fig. (4.54), similar trends as observed at logging point 2 were seen. The big vent case generally recorded higher temperatures than the advanced geometry case (base case), but both cases recorded lower temperatures than what was observed at logging point 2. The big vent case recorded a similar final temperature increase as observed for the advanced geometry case (base case), but the final temperature increase of the advanced geometry case (base case) was higher, reaching approximately similar temperatures

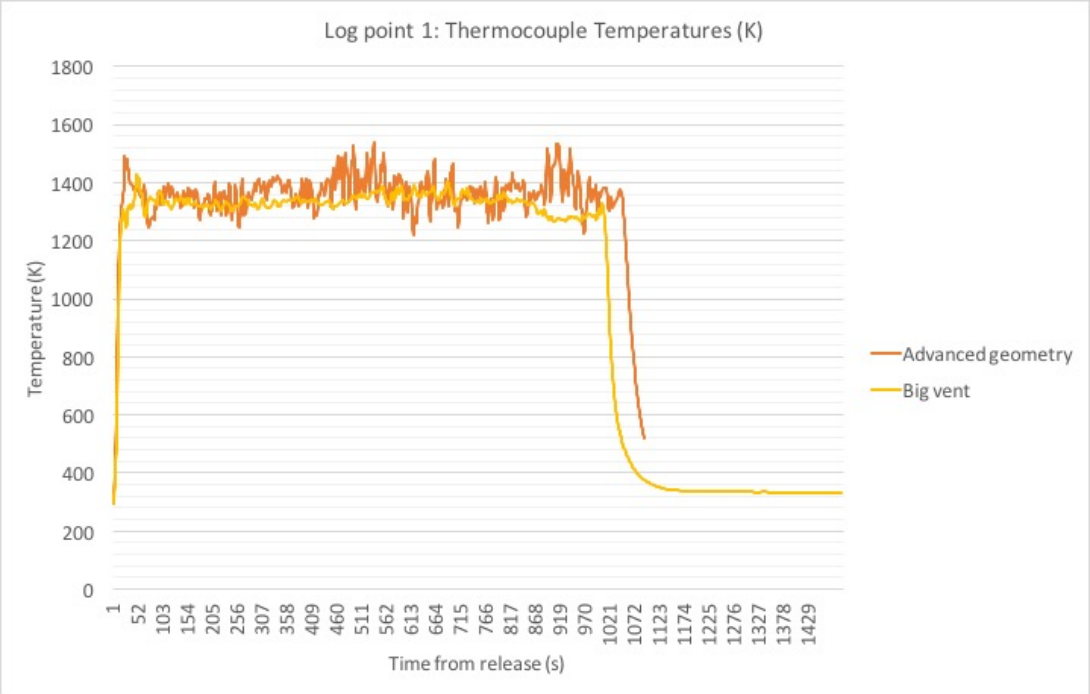

Figure 4.52: Investigation into the effect of the ventilation opening size. The advanced geometry case (base case), with ventilation opening as given in Fig. (3.1), is compared with the big vent case, with approximately 7.8 m^2 bigger ventilation opening. thermocouple temperatures, logging point 1.

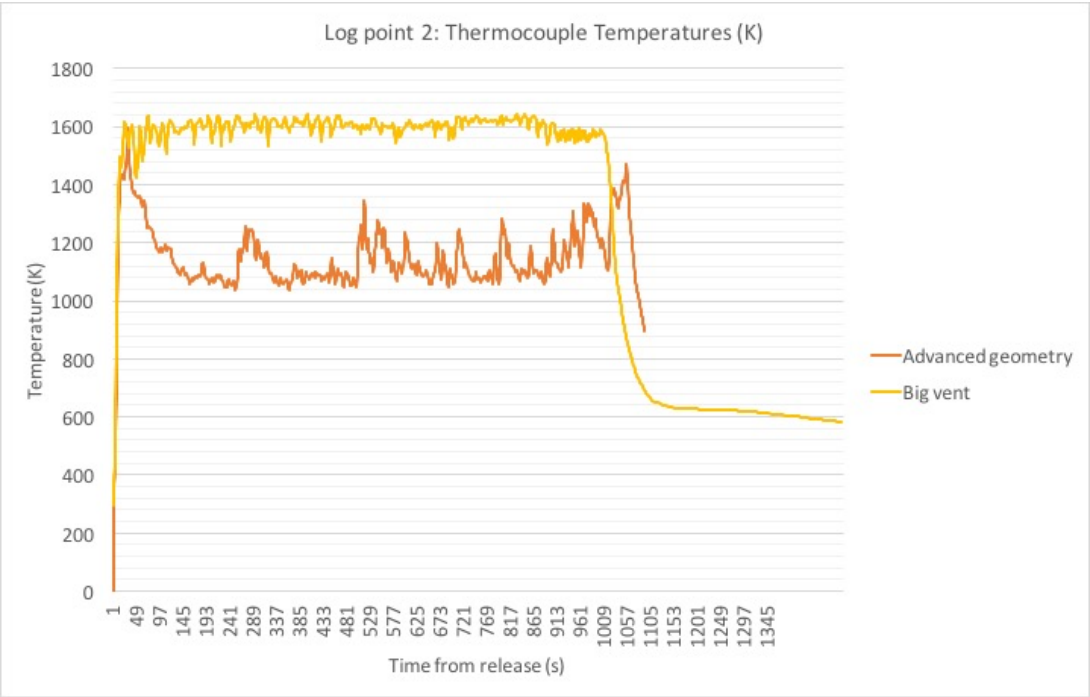

Figure 4.53: Investigation into the effect of the ventilation opening size. The advanced geometry case (base case), with ventilation opening as given in Fig. (3.1), is compared with the big vent case, with approximately 7.8 m^2 bigger ventilation opening. thermocouple temperatures, logging point 2.

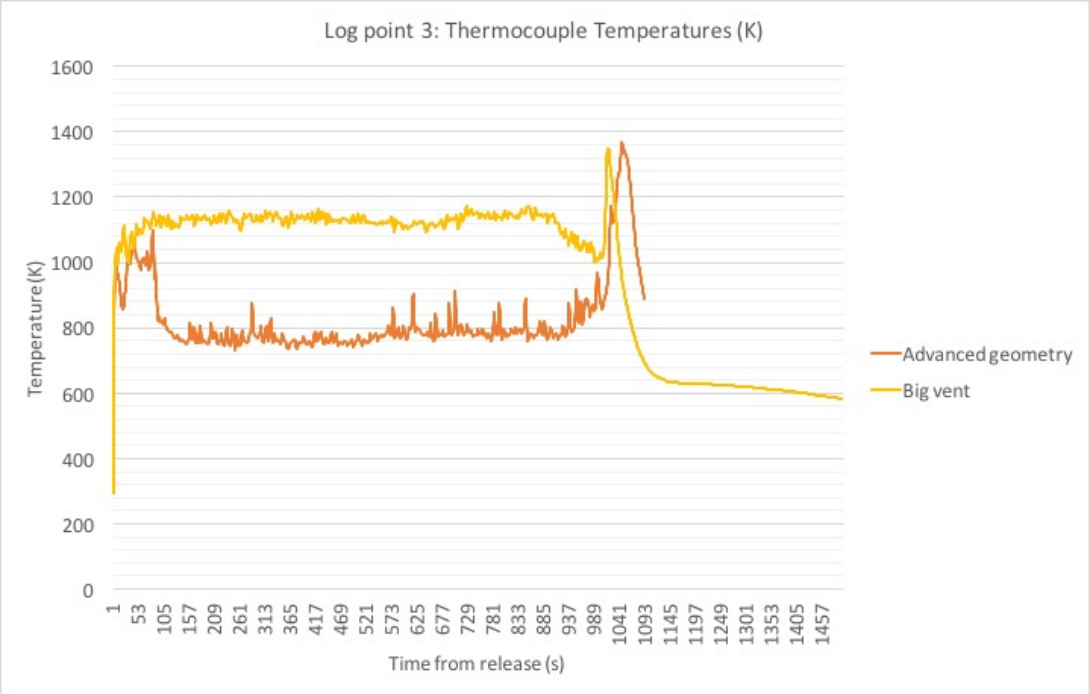

Figure 4.54: Investigation into the effect of the ventilation opening size. The advanced geometry case (base case), with ventilation opening as given in Fig. (3.1), is compared with the big vent case, with approximately 7.8 m^2 bigger ventilation opening. thermocouple temperatures, logging point 3.

as the big vent case. Both cases generally recorded less temperature variations than what was observed at logging point 2.

At logging point 4, given in Fig. (4.55), both cases showed a small increase in recorded temperatures compared to logging point 3. The temperature difference between the cases, was similar to what was observed at logging points 2 and 3. For the big vent case, no final temperature increase was recorded at logging point 4, while the temperature increase of the advanced geometry case (base case) was smaller and more gradual than what was observed at logging point 3.

Radiation heat flux

The big vent case generally recorded much higher radiation heat fluxes than the advanced geometry case (base case). The highest heat fluxes were logged at logging point 5, given in Fig. (4.56), for both the advanced geometry (base case) and big vent cases. The big vent case recorded more variations in radiation heat flux at logging point 6, given in Fig. (4.57), than recorded at logging point 5, especially initially.

At logging point 7, given in Fig. (4.58), the big vent case recorded higher variation amplitudes than what was recorded at logging points 5 and 6. The radiation heat fluxes of the big vent case was generally lower than what was recorded at logging point 6. The difference between the cases in recorded radiation heat fluxes witnessed at logging points 5 and 6, was maintained at logging point 7.

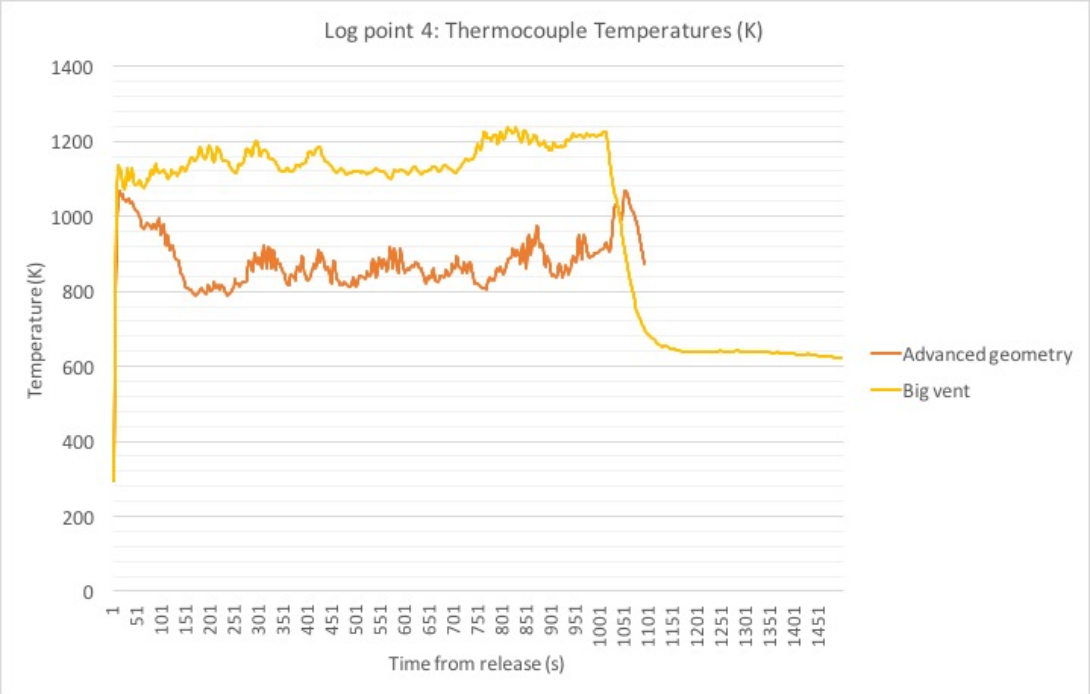

Figure 4.55: Investigation into the effect of the ventilation opening size. The advanced geometry case (base case), with ventilation opening as given in Fig. (3.1), is compared with the big vent case, with approximately 7.8 m^2 bigger ventilation opening. thermocouple temperatures, logging point 4.

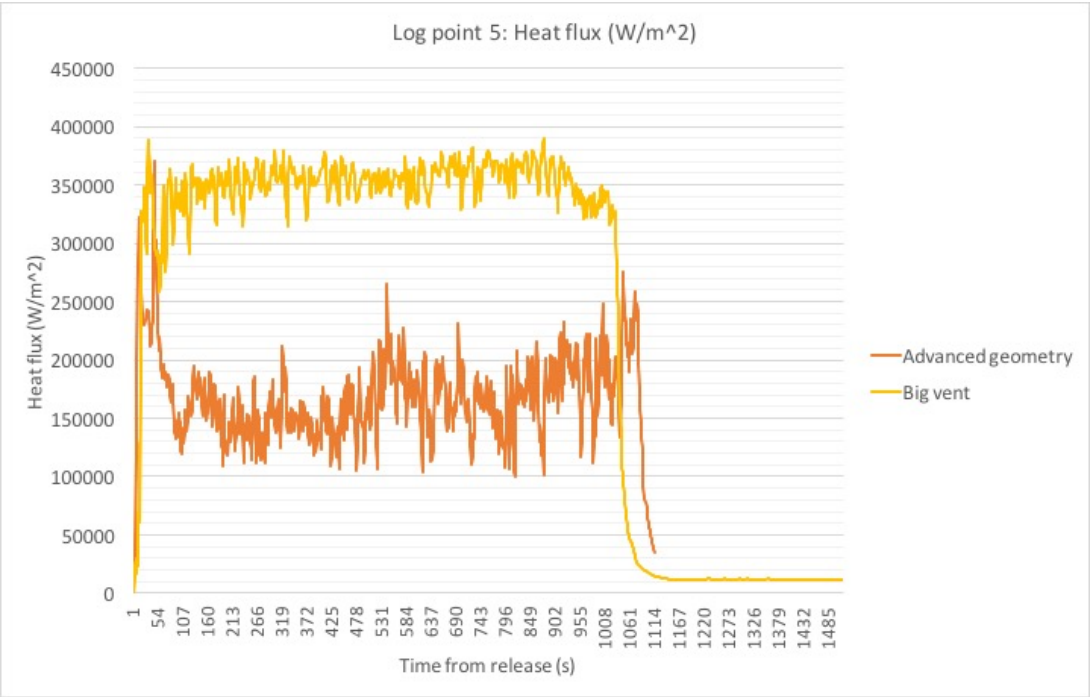

Figure 4.56: Investigation into the effect of the ventilation opening size. The advanced geometry case (base case), with ventilation opening as given in Fig. (3.1), is compared with the big vent case, with approximately 7.8 m^2 bigger ventilation opening. Radiation heat flux, logging point 5.

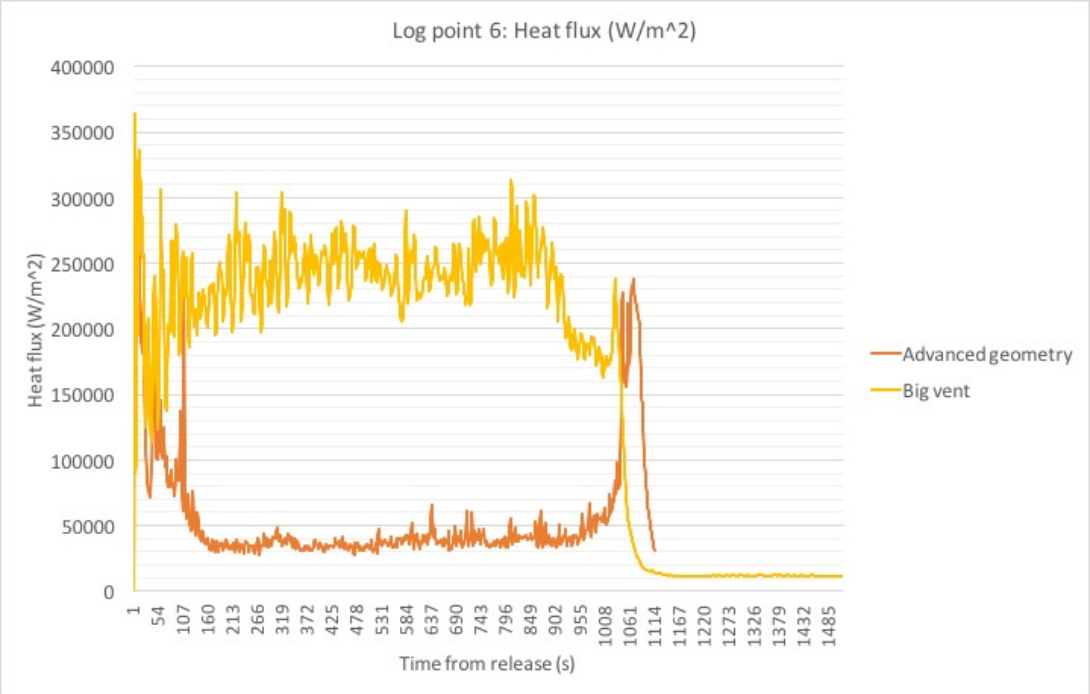

Figure 4.57: Investigation into the effect of the ventilation opening size. The advanced geometry case (base case), with ventilation opening as given in Fig. (3.1), is compared with the big vent case, with approximately 7.8 m^2 bigger ventilation opening. Radiation heat flux, logging point 6.

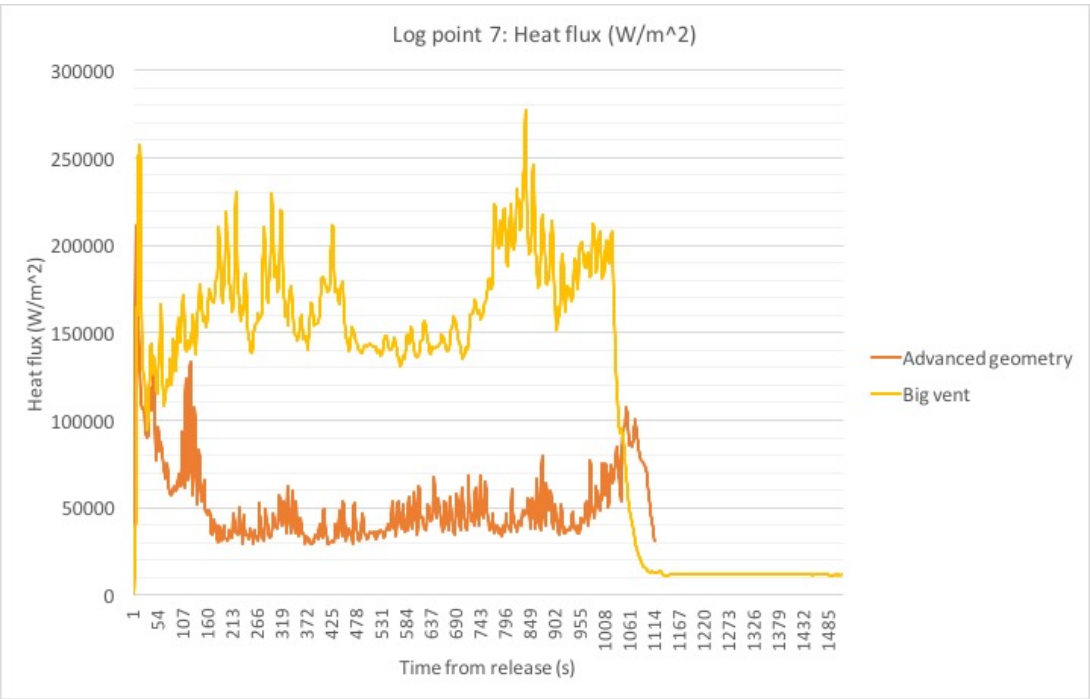

Figure 4.58: Investigation into the effect of the ventilation opening size. The advanced geometry case (base case), with ventilation opening as given in Fig. (3.1), is compared with the big vent case, with approximately 7.8 m^2 bigger ventilation opening. Radiation heat flux, logging point 7.

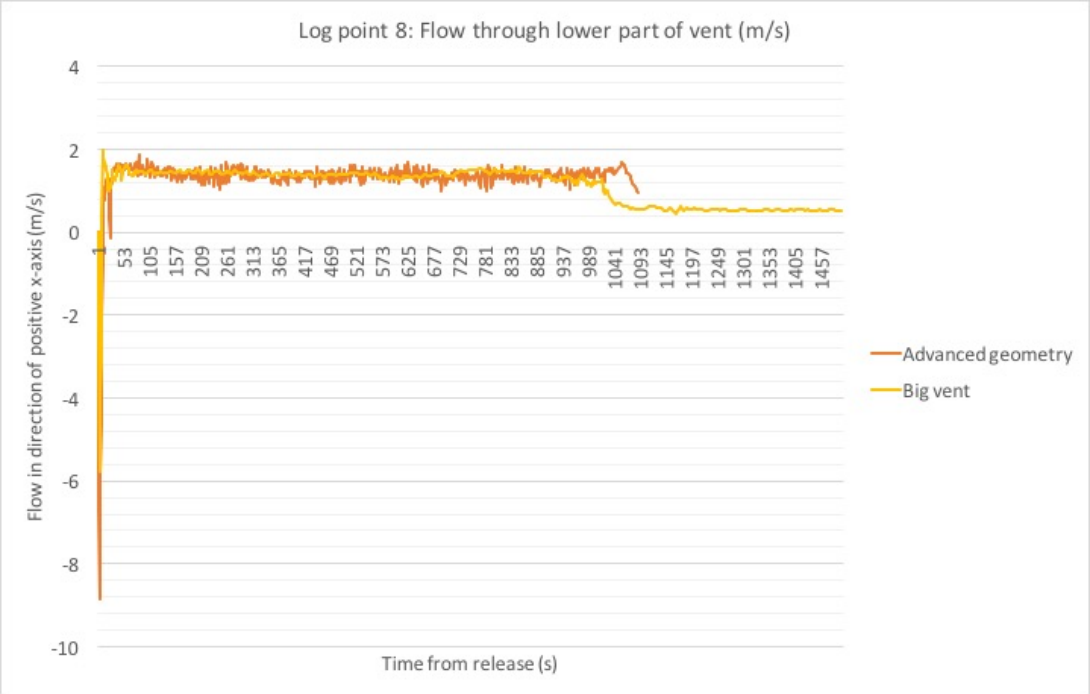

Figure 4.59: Investigation into the effect of the ventilation opening size. The advanced geometry case (base case), with ventilation opening as given in Fig. (3.1), is compared with the big vent case, with approximately 7.8 m^2 bigger ventilation opening. Vent flow velocity , logging point 8.

Oxygen in the compartment

Similar inflow velocity, given in Fig. (4.59), was observed for the advanced geometry (base case) and the big vent cases. This observation was of interest, because the larger vent size of the big vent case would indicate a much higher flow rate into the compartment. The oxygen quantity, measured at the z=0.3 m plane, showed large differences between the advanced geometry case (base case) and the big vent case. While the oxygen was limited to a small area close to the vent, for the advanced geometry case (base case), oxygen of approximately atmospheric content was observed along the whole z=0.3 m plane, for the big vent case. Regarding flow at the inside of the enclosure, a large circular motion was observed inside the whole compartment. The flow moved towards the west wall along the floor, and when reaching the west wall, flowing towards the ceiling. In the upper layer, flow was directed towards the vent. This description of flow motion is based on general trends, of the flow, observed at the inside of the enclosure. Variations in flow, especially around the walls and close to the spray, were observed, but generally, the flow velocity in the east-west direction was higher than in north-south direction.

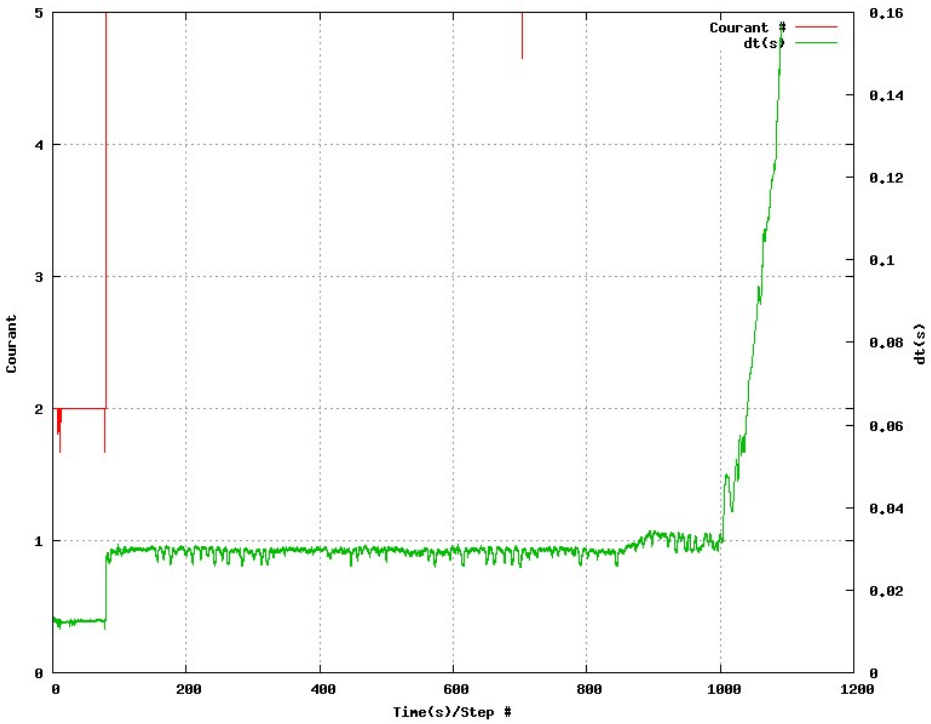

Figure 4.60: Courant number development for the advanced geometry case (base case)

4.8 Courant number

A small investigation on maximum Courant number was completed in the advanced geometry case (base case), by increasing the maximum Courant number from 2-5. As observed in Fig. (4.60), the change in Courant number happened at approximately 100 s, where it was also observed that the increase in Courant number led to an increase in the time step. The larger time step translated to a significant reduction in calculation time.

The stability of the calculation can be observed by a carbon balance, as given in Fig. (4.61). The carbon entering the domain was quite stable at 0.85 kg/s, for the first 850 seconds, with a linear decrease to 0.75 kg/s, between approximately 850 and 900 seconds. After 900 seconds, the carbon entering the domain was stable at 0.75 kg/s. Some variations were observed, in the form of large peaks for the entering carbon. These peaks can be understood as a warning of instability. Immediately after the observed peaks, the values for entering carbon stabilized at the set values, indicating no breach of the stability of the calculation.

Also worth noting in the carbon balance, was that the change in Courant number at approximately 100 s seemed to have very little effect on the stability of the calculation. The same trends as seen before the increase in maximum Courant number, continued after the increase.

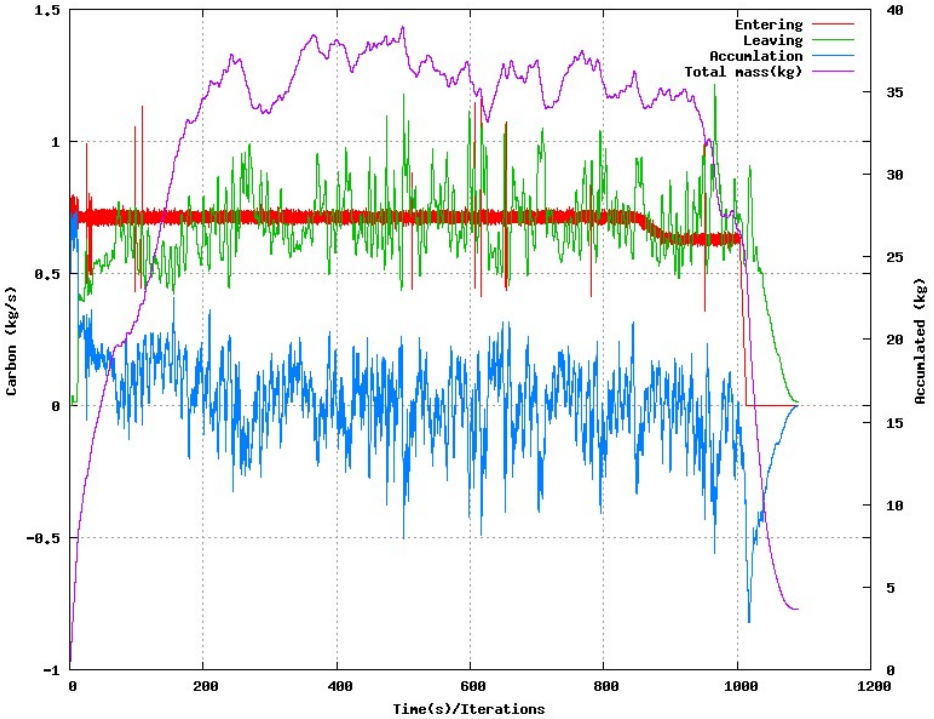

Figure 4.61: Carbon balance development for the advanced geometry case (base case)

Chapter 5

Discussion

5.1 Model choices

Combustion hierarchy

In the reaction hierarchy described in Sec. (3.1.2), the hydrocarbon reactions were calculated simultaneously, before the CO and H_2 reactions. An indication of this reaction hierarchy was observed in the quasi-stable flame period, in the advanced geometry case (base case). The concentrations of H_2, CO and C_7H_{16} were observed at the z=4.5 m plane. Here the O_2 concentration was zero. The mole fraction $\frac{n_{H_2}}{n_{CO}}$ was observed to be spatially stable at 1.14-1.15. For the mole fraction $\frac{n_{H_2}}{n_{C_7H_{16}}}$, a spatial variation of approximately 8, close to the west wall, increasing to approximately 50 close to the vent, was observed. It seems like the concentration of H_2 increased, while the concentration of C_7H_{16} decreased, when moving from the west wall towards the vent. The observation indicated that the reaction hierarchy mentioned in Sec. (3.1.2) was followed.

It could be argued that this reaction hierarchy is not physically correct. Hydrogen is known to react fast [38](p.148-172), raising the question if the reaction hierarchy should be altered with H_2 combustion being prioritized. In this thesis oxygen depletion was observed, making the reaction hierarchy more important. Fuels lower down in the hierarchy will not combust, because of the lack of oxygen. Instead of all the hydrocarbon species reacting simultaneously and risking oxygen depletion and no hydrogen reactions, a hierarchy among the hydrocarbons based on reaction rate could be established. For every step in the hierarchy, the hydrogen reactions could be solved and thereby confirming the physics behind the faster hydrogen reactions. The oxygen depletion will, consequently, to a higher degree limit the slower hydrocarbon reactions rather than the faster hydrogen reactions.

Challenges with estimating correct compositions in simulations of under-ventilated fires have also been found in Gottuk et al. [12]. Here the collection of computer codes used was CHEMKIN by Kee et al. [16] and the kinetics model used was a subset of the Miller and Bowman mechanism [27]. Here, it was found that the model used over-predicted CO concentrations for under-ventilated fires, while under-predicting CO_2 concentrations. According to

the model used, the O_2 was depleted during hydrocarbon oxidation and high levels of CO and H_2 were observed. In Gottuk et al. [12], it was argued that the discrepancy between the model results and experimental measurements, could be due to incorrect gas-phase kinetics and incorrect modelling approach and assumptions. Gottuk and Lattimer [11] has discussed the production of species within a compartment fire and the transport of these gases out of the fire compartment to adjacent areas. Results from experiments on a small-scale two-layer environment by Beyler [2] were reported. Here it was found an increase in H_2 quantity in under-ventilated burning conditions. From the results found in this thesis, and by others, it is challenging to estimate the effect of altering the reaction hierarchy and what hierarchy that would best estimate experimental values.

The choice of combustion hierarchy, in KFX, was done by ComputIT because it allowed them to obtain more correct flame temperatures compared to real fire tests. Initially, only global reactions were calculated, but by splitting the reactions by including H_2 and CO reactions, more correct temperatures were obtained. The choice was made only for increased precision in prediction of temperatures, and the effect the change has had on compositions was not addressed. The compositions obtained in the simulations in this thesis are therefore not necessarily correct, ComputIT therefore discourage the use of the compositions as valid parameters.

The Eddy Dissipation Concept

In the simulations χ was calculated by Eq. (2.22). The model used was similar to the one presented in Ertesvåg [7], formulated by Gran [13] from Magnussen [23]. Here η in Eq. (2.25) correspond to χ_3 in Ertesvåg [7]. It was observed, that the model used in the simulations does not have the limitation on χ seen in Ertesvåg [7] for χ_2. The omittance of this limitation could potentially lead to high values for χ in the simulations, possibly above the constraints set by Gran [13] of $0 \leq \chi \leq 1$. A large χ could lead to faster reactions. In the simulations conducted in this thesis the mixing was slow, leading to the reaction rate being more dependant on the mixing processes. The reactions were seen as infinitely fast so if the conditions allowed reactions, the reactants would react. Hence, how fast the reactions were was of less importance.

Turbulence

The buoyancy equation from Vembe et al. [39], given in Eq. (2.14) is not dimensionally correct.

$$B = -\frac{\mu_t}{\sigma_t}\frac{\partial \overline{\rho}}{\partial x_i} g_i \tag{5.1}$$

The model differs from one of the models found in Chung and Devaud [5], which is given as:

$$B = -\frac{\mu_t}{\sigma_t}\frac{1}{\overline{\rho}}\frac{\partial \overline{\rho}}{\partial x_i} g_i \tag{5.2}$$

where Eq. (5.1) is divided by $\overline{\rho}$ in Eq. (5.2). The average density ($\overline{\rho}$) is often approximately 1, indicating that the effects of incorrect B were not substantial in the simulations performed in this thesis.

5.2 Enclosure modelling

The way the enclosure was modeled, showed to have large impact on the fire development. The results from the cases run with different enclosure modelling indicated that the most important decider of temperatures at the inside of the enclosure, was air entrainment and mixing. The further into the compartment the air was transported, the higher temperatures were observed. In the advanced geometry case (base case), in the quasi-stable temperature time period, a flow was observed down the west wall and along the floor towards the vent. This flow was quite stable compared to the KFX geometry case, where a flow with more variations was observed flowing both up and down the west wall. This flow observed in the advanced geometry case (base case) could be one possible explanation of the limitation of air inflow into the compartment. The flow down the west wall could contribute by forcing the inflowing air back towards the vent, thereby preventing the air from reaching further into the compartment.

In the results, it was observed that the KFX geometry case had air reaching further into the enclosure than the simple geometry, advanced geometry (base case) and no-imported-geometry cases. A thorough review of the KFX generated geometry revealed no inconsistencies in the wall geometries which could lead to potential air leaks. The wall properties were also correct, also indicating that the explanation of the results could not be due to geometry model faults. By reviewing the modelled enclosure in the advanced geometry case (base case) against the modelled enclosure in the KFX geometry case, a difference in how the walls, ceiling and floor were created was observed. In the KFX geometry, the walls, ceiling and floor were created by small sections, which together formed the larger solid structures of the walls, ceiling and floor. In the advanced geometry case(base case), every wall, ceiling and floor were modelled as one section. Based on these differences in representation of the geometry, it is possible that there were small openings in the walls where air was entrained, for the KFX geometry case. This air flow was, however, too small to be easily detected in the simulations.

The CAD geometry import works by converting CAD geometry files into a geometry format supported by KFX. The geometry is processed into surface and volume porosities. KFX read porosity input from two sources, namely the input case file and the porosity file. The input case file has limitations regarding porosity, where only open, half-blocked and fully blocked surfaces are supported. By including the porosity file, a more detailed porosity field can be created [40]. For the advanced geometry (base case), simple geometry and no-imported-geometry cases, the geometry cells were altered and a CAD block was placed over them, before importing the geometry again. The CAD block prevented porosity file input on

the CAD blocked cells. The porosity file was consequently not used for calculations on the solid geometry of the advanced geometry (base case), simple geometry and no-imported-geometry cases. Given the more detailed representations given by the porosity file, a geometry not using the porosity file would be less detailed. The big differences in results between the KFX geometry case and the advanced geometry (base case), simple geometry and no-imported-geometry cases, indicated that the influence of the porosity file could be significant. The porosity file seems to significantly influence the temperature and flow distributions at the inside of the enclosure. One explanation for the obtained results, could be related to case sensitivity. The simulation of fire test JF5 seemed very sensitive to the enclosure modelling, where small changes to the model, could give large changes in flow distributions at the inside of the enclosure. The extra precision in modelling of the geometry walls, provided by the porosity file, could therefore be of importance. The small differences between the advanced geometry case (base case) and the solid cell case indicated that the choice of solid cell type does not significantly influence the results. The case using solid cells and the case using thin walled cells gave very similar results.

The influence of the enclosure model on air flow and temperatures at the inside of the enclosure was further confirmed in the big vent case. An increase in the vent area allowed more air to enter further into the compartment. The air was mixed with the fuel in the upper layer, and higher temperatures inside the enclosure were observed. The big vent case was also observed to record less variations in temperatures, than the advanced geometry case (base case). Based on these results from the big vent case and the results obtained from the KFX geometry case, there seems to be a relation between temperature variations inside the compartment and the degree of under-ventilation. The lesser under-ventilation of the big vent case was indicated by the similar air flow velocity as the advanced geometry case (base case) at logging point 8, but with a bigger vent, giving larger flow rate. The similar velocities recorded for all cases, could indicate that the flow through the vent reached a critical velocity, where an additional increase in velocity was not possible. The big vent case also showed a different flow distribution at the inside of the enclosure, where generally one large circulatory motion was observed filling the whole compartment.

For the no-imported-geometry case, no structures were included inside the enclosure. The lack of structures did not seem to give radical changes in the temperature distributions at the inside of the enclosure. One explanation, could be that all cases showed established flow distributions during the quasi-stable temperature time period. Large flow patterns were created, utilizing the whole of the compartment. The impact of the structures was thereby reduced by the flow flowing around the structures, without the structures significantly affecting the flow. The velocity of the flow and the size of the structures did not seem to be of such a magnitude to initiate additional turbulent motions and mixing inside the enclosure. The effect of the horizontal and vertical structures on flow at the inside of the enclosure, was not investigated in Drangsholt et al. [6].

The high temperature and heat flux variations observed initially for all cases, seemed to

be related to the position of the flame. Initially, the flame was observed to fill the upper part of the enclosure, which would give high temperatures and heat fluxes. When the fuel release was stopped, the external flame decreased and the flame moved towards the inside of the enclosure, which would give higher temperatures and heat fluxes. This development was also confirmed by the positions of the logging points. The highest variations were recorded, where the flames were estimated to be.

Insulation

The simulation of the adiabatic case showed only small differences in temperatures compared to the advanced geometry case (base case). The small increases in temperatures and radiation heat fluxes of the adiabatic case compared to the advanced geometry case (base case) could be explained by heat transfer through the walls of the compartment. The surface temperatures measured on the inside of the enclosure walls were similar for the two cases, with the adiabatic case generally recording approximately 100 K higher temperatures than the advanced geometry case (base case). Maximum temperatures of approximately 1700 K for the adiabatic case and 1650 K for the advanced geometry case (base case) were observed. A heat balance equation for the surface is given by:

$$q_{\text{rad,in}} + q_{\text{conv}} = q_{\text{rad,out}} + q_{\text{cond}} \tag{5.3}$$

$q_{\text{r,in}}$ is the radiative heat flux absorbed by the surface, q_{conv} is the convective heat flux from the adjacent flow to the surface, $q_{\text{r,out}}$ is the radiative heat flux from the surface and q_{cond} is the conductive heat transfer into the obstacle control volume.

q_{cond} is dependent on the temperature gradient in the wall close to the wall surface:

$$q_{\text{cond}} = K(\frac{dT}{dx}) \tag{5.4}$$

where $(\frac{dT}{dx})$ is the temperature gradient of the wall close to the wall surface. One simple choice of temperature gradient is:

$$(\frac{dT}{dx}) = \frac{T_s - T_p}{dx_p} \tag{5.5}$$

where dx_p is the distance from the surface to the control volume centre. T_s is the surface temperature and T_p is the temperature at the control volume centre.

Given the low K-value of 0.161 W/mK, the heat transferred by conductivity was very small for the advanced geometry case (base case). For a surface temperature of 1650 K, control volume centre temperature of 293 K and dx_p of 0.151 m, the heat transferred due to conduction was calculated to be approximately 1450 W/m^2. Given the recorded radiation heat fluxes inside the room of 25000 to 400000 W/m^2, the heat removed due to conduction through the walls in the advanced geometry case (base case, $K = 0.161$) could potentially only account for approximately 0.3-6% of the incident heat flux on the wall. Consequently, most of the

heat absorbed by the surface will be re-emitted into the enclosure by radiation from the surface. A further reduction of the heat conductivity of the walls will mean that less heat will be transported through the walls and more heat will be re-emitted into the enclosure. Since most of the incident heat on the inside surface of the enclosure walls in the advanced geometry case (base case) was already re-emitted into the enclosure, the potential extra heat that could be emitted from the walls by lowering the heat conductivity in the adiabatic case does not seem significant. The close to atmospheric temperatures observed at the outside of the walls for both the advanced geometry case (base case) and the adiabatic case indicated that both cases were substantially insulated. Low temperatures, below the ambient temperatures, were observed at the outside surface of the adiabatic case. This observation was not further researched in this thesis, but could indicate problems with the calculation of heat transfer through the walls.

The effect of insulation found in this thesis is further substantiated by Welch et al. [42]. The findings of Welch et al. [42] on effect of insulation were based on two fire experiments in a large compartment, measuring 12x12 m in floor area by 3 m in height, where the thermal insulation of the compartment boundaries was varied. The first insulation case had walls with a thermal inertia of 1600 J/(m^{2}s$^{1/2}$K), while the second insulation case had walls with thermal inertia of 720 J/(m^{2}s$^{1/2}$K) (Comparing to the advanced geometry case (base case) which had a thermal inertia of 198 J/(m^{2}s$^{1/2}$K)). Both temperatures and heat fluxes inside the compartment were logged. Comparison of the results from the two cases showed very small differences between the two cases. The varying fire insulation in the cases had very little influence on temperatures [42].

5.3 Fuel release modelling

Varying the dispersion angle did not show to significantly impact the fire development inside the enclosure, as observed in Sec. (4.5). The flow distributions at the inside of the enclosure, for the small dispersion angle and large dispersion angle cases, were similar to the flow distribution of the advanced geometry case (base case). The droplet size was seen to significantly influence the flame development in the compartment, as seen in the results given in Sec. (4.4). For the different droplet diameters, big differences in flow motion at the inside of the compartment were observed. The advanced geometry (base case), the large diameter and small diameter cases generally had two circular flow motions inside the room, one close to the vent and one further into the room, closer to the west wall. For all three cases, the three dimensional flow distributions at the inside of the enclosure were quite stable. Except around the impingement point of the fuel spray on the ceiling, the velocity of the flow motions in east-west direction were generally significantly higher than the flow motions in north-south direction. Some transient flow variations were observed, especially close to the fuel spray and close to the walls, but the trend of the two circular motions was observed in the whole compartment. Close to the north and south walls more shifting flows were observed,

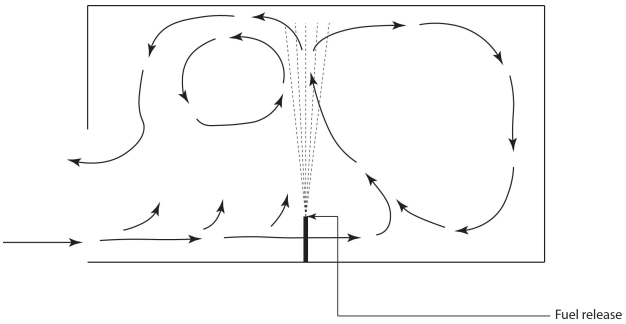

Figure 5.1: Flow inside enclosure, the small diameter case. The figure is based on three dimensional trends observed at the inside of the enclosure. The trends were observed during the quasi-stable temperature time period.

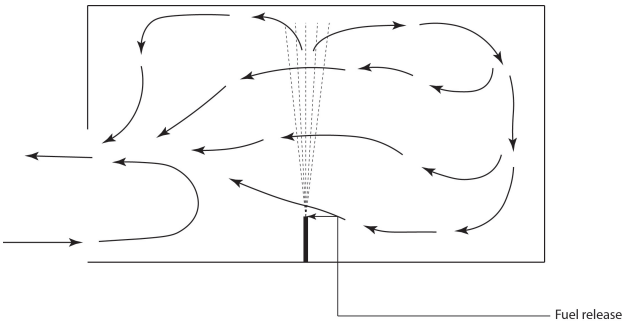

Figure 5.2: Flow inside enclosure, the advanced geometry case (base case), droplet sizes as given for SMD in Table (3.2). The figure is based on three dimensional trends observed at the inside of the enclosure. The trends were observed during the quasi-stable temperature time period.

with oxygen flow fluttering between the north and south walls. The two circular motions inside the room were spinning in opposite direction of each other. In the small diameter case, a simple 2D representation (plane normal to y-direction) of the flow inside the room, can be seen in Fig. (5.1), the vent side flow was observed to be bigger than the flow further into the room. In the advanced geometry case (base case), with a simple 2D representation given in Fig. (5.2), the flow closest to the west wall was observed to be bigger than the vent side flow. In the large diameter case, with a simple 2D representation given in Fig. (5.3), the two circular flows were approximately equal.

The investigation into droplet diameter further confirmed the observations regarding enclosure modelling in Sec. (5.2). The further the oxygen reaches into the enclosure, the more combustion and higher temperatures are observed. As observed from the figures describing the flow at the inside of the compartment, the droplet momentum seems to be one deciding factor for flow motions. For the large diameter case a separation zone seems to be established along the fuel release spray, with two separate circular motions either side of the separation zone. It is possible that the droplet momentum is of such a magnitude that a flow separation zone is set up around the spray. The flow motions inside the room would not able to move through the separation zone, leading to the formation of the two circular motions

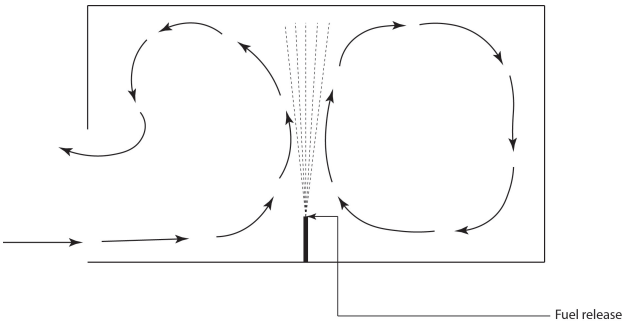

Figure 5.3: Flow inside enclosure, the large diameter case. The figure is based on three dimensional trends observed at the inside of the enclosure. The trends were observed during the quasi-stable temperature time period.

either side of the separation zone. The air flow from the vent would not be able to move through the separation zone, limiting the oxygen inflow. For the advanced geometry case (base case), it seems like the droplet momentum is also of such a magnitude low down in the compartment, to not allow the air flowing through the vent and along the floor to move through a separation zone set around the spray flow. Higher up in the enclosure, where more of the droplets have evaporated, the droplet momentum has decreased to such a degree, that the circular motion closest to the west wall would be able to move through it and flow out of the vent. As observed from Fig. (5.2), it is possible that the momentum of the west wall flow is of such a magnitude that it is able to force the air flow back towards the vent, and prevent the air from reaching further into the compartment. For the small diameter case, it seems like the droplet momentum is small enough to let air-flow from the vent past the spray separation zone. This allows a large vent side flow to be formed, leading to increased oxygen mixing and combustion as a result. The rate of droplet evaporation and the position of the combustion could also be possible explanations of flow motions at the inside of the compartment, and how far the air reaches into the compartment. In the small diameter case, full evaporation of the spray was observed lower down in the compartment, as seen in Fig. (4.27). The larger amount of gaseous fuel lower down in the enclosure could potentially also give combustion lower down in the compartment. The following expansion and buoyancy effects could initiate increased mixing in lower parts of the compartment, and allow oxygen to flow further into the compartment.

In the logging of thermocouple temperatures in Sec. (4.4), it was observed that the small diameter case showed less variations in temperatures than the large diameter case and advanced geometry case (base case). This difference could be explained by flame stability. The variation of flame heights on the outside of the compartment was bigger for the advanced geometry case (base case), than for the small diameter case. 8-15 m compared to 8-11 m. Together with the variations in flow observed at logging point 8, given in Fig. (4.35), this could indicate a cyclic pulsating fire development, where oxygen flowing into the room is followed by an increase in flame height. The increase in flame height means less room in the vent for fresh air to move through, which again give a decrease in flame height and increase in

inflow through the vent. This cycle is repeated, giving the pulsating development. Because the flames of the advanced geometry case (base case) and large diameter case were located closer to the vent, these cases could be more susceptible to changes in the oxygen inflow, compared to the small diameter case, where a stable flame layer in the upper half of the enclosure could give a fire less susceptible to oxygen variations. The small diameter case also had similar temperature variations and a similar upper layer flame development as the big vent case and the KFX geometry case. These observations indicate that the increased combustion and mixing inside the room, due to air reaching further into the room, give more stable temperatures. The increase in thermocouple temperatures observed for the small diameter case after the fuel release was stopped, given in Figs. (4.29), (4.30) and (4.30), could be related to oxidation of soot in the upper parts of the enclosure. The logging points 2, 3 and 4 were all placed in the upper parts of the enclosure, where a soot layer was observed after the fuel release was stopped. The results obtained from the low fuel flow rate case seems to confirm what were observed for several of the other cases, where a decrease in fuel flow rate seems to give an increase in recorded thermocouple temperatures. By decreasing the flow rate of the rich component, fuel, an increase in temperatures are observed. The increase in recorded temperatures could be explained by a smaller fuel flow rate, giving less underventilated conditions at the inside of the enclosure and potentially a smaller external flame, as explained in Gottuk and Lattimer [11]. This would allow more oxygen to flow through the vent and mix with the fuel at the inside of the compartment, giving more combustion and higher temperatures. In the experimental data in Drangsholt et al. [6], a standard deviation for the fuel flow rate of ±1.3% was presented. The limit of error for fuel flow rate in tables and charts, was maximum ±2.6% (two standard deviations used for 95% confidence interval). Given the results obtained for different fuel flow rates in this thesis, the potential deviations in fuel flow rate were probably not large enough to drastically influence the results in this thesis. It was also reported in Drangsholt et al. [6], that the change in fuel flow rate from 0.85 kg/s to 0.75 kg/s did not have significant effect on measured temperatures.

5.4 Courant number

The simulation of the enclosure jet fire was particularly computationally demanding, as witnessed by long simulation times. The Courant number, as recommended in the KFX simulation software, of 2 for jet fires, gave very long simulation times of up towards 2 months. A literature search and experimental procedure on critical Courant numbers, was investigated. The transient behaviour in the simulations was modelled with the backward Euler scheme. The scheme was second order upwind, and an implicit numerical method was used[39]. Gerolymos and Vallet [10] found upwind schemes to be very robust for treating the convection of turbulence variables, and did research into "developing a fully coupled implicit upwind scheme for the three-dimensional compressible Navier–Stokes equations, combining computational efficiency and computational robustness". In the research Courant num-

bers as high as 80 were found to give convergence. The possibilities of experimenting with Courant numbers could consequently be described as vast, where the maximum possible Courant number depends on the case. For especially computationally demanding cases, experiments with Courant numbers could give a large reduction in computational time.

5.5 Spray fire in an under-ventilated enclosure

The trend shown through the simulations seem to be that the oxygen entrainment and flow movements at the inside of the compartment are some of the most important parameters regarding fire development in an under-ventilated spray fire. All simulations indicated that the further the oxygen was transported into the enclosure, the higher temperatures would be recorded. Modelling parameters that influence the oxygen flow will therefore be of great importance. Great care should be taken when modelling both the spray and the geometry, while small changes in flow distributions at the inside of the enclosure could potentially give drastically different fire developments.

The variations in oxygen quantity between the walls observed in the advanced geometry case (base case), could potentially be explained by flame movements at the inside of the room and at the vent. The flame moves to positions with more oxygen. The movement of the flame would reduce the oxygen inflow through the vent at the given location, increasing oxygen inflow to a position with a smaller flame, which again would shift the flame. This relation on the oxygen motions correspond to the findings of Hwang et al. [14], where more oxygen was found to flow along the side walls of a enclosure, where the flames were at its smallest.

The relation given by Williams [43](p.130,131) and described in Sec. (1.2.1), that combustion with small droplets will give less sooting, was found in the simulations in this thesis as well. In the upper part of the enclosure, significantly less soot was found in the small diameter case, than in the large diameter case and advanced geometry case (base case). Increasing the dispersion angle did not lead to a significant reduction in soot production, where the quantity of soot found in the upper part of the enclosure for the large dispersion angle case, small dispersion angle case and advanced geometry case(base case) was similar.

The experimental study done by Hwang et al. [14], described in Sec. (1.2.2), showed similarities with the results obtained here in the advanced geometry case (base case). A Fire test was conducted in an under-ventilated room, and the flame was observed to attach only to the front side of the fuel release, with direction towards the vent. Most of the flame was observed burning externally. Sharp gradients across the flame were found with atmospheric oxygen on the vent side and no oxygen on the side facing the back wall of the compartment. These results differed from some of the results found for gas phase fires in Chamberlain [3], where in an under-ventilated compartment fire, the whole compartment except for a narrow layer close to the floor was filled with turbulent flames. For one of the fire tests in Chamberlain [3], a liquid propane fuel was used. For this fire test, the upper layer did not ignite,

showing results more similar to the advanced geometry case (base case), and the experimental study of Hwang et al. [14].

The observations by Hwang et al. [14] and Chamberlain [3] and the results obtained here from the simulations investigating the vent size, raises the question of critical conditions that are needed for ignition of the upper layer in a compartment fire. Sudden ignitions of combustible gases are found in phenomenons like backdraft and flashover [45] [17], where parameters like compartment geometry, compartment material, size of ventilation opening, fuel flow rate and jet momentum are found to be of importance. In Sec. (1.2.1), it was also referred to Williams [43] about the importance of the geometry and spray distribution on mixing. In the simulations conducted in this thesis some of the cases have ignition of the upper layer, while some of the cases have not. Giving the varied results for different modelling parameters in this thesis, one could argue that a critical condition of ignition of the upper layer exists, and that a more thorough analysis on parameter sensitivity on upper layer ignition needs to be conducted.

5.6 Validation of simulations against JF5

For validation of the simulations, the temperatures obtained in the simulation logging points 1-4, given in Table (3.3), were compared with the temperatures of test JF5, in the Blast and Fire Engineering for Topside Structures Test Programme F3, given in Figs. (1.2), (1.3), (1.4) and (1.5)

At logging point 1 most of the simulations showed quite good coherence with JF5, given in Fig. (1.2)(p.10). The stable temperatures recorded in the KFX geometry case, given in Fig. (4.1)(p.48), were lower than the maximum temperatures recorded at JF5. Other cases, like the small dispersion angle case given in Fig. (4.36)(p.76), recorded more variations in temperature than the KFX geometry case, although the stable temperatures were similar to the KFX geometry case, and therefore higher maximum temperatures comparable to JF5. The reason for the similar temperatures recorded in the different cases, could be explained by the location of logging point 1. Logging point 1 was placed in the upper part of the ventilation opening. Due to buoyancy of warmer flows, the flame was expected to exit the compartment at the upper part of the vent, while inflow of air would be in the lower part of the vent. The temperatures recorded at logging point 1 would therefore be related to the flame temperature. The flame temperatures depend on the fuel composition, which was similar for all cases, giving similar temperatures at logging point 1. The transient temperature development of JF5 was slightly different compared to the simulated cases. While JF5 had a more gradual transient increase in temperatures, the simulations had a very steep transient temperature increase initially, followed by more stable temperatures.

For logging point 2, the KFX geometry case, given in Fig. (4.2)(p.49), and the big vent case, given in Fig. (4.53)(p.89), were able to quite correctly predict the temperatures achieved in JF5, given in Fig. (1.3)(p.10). Most of the other cases predicted temperatures that were ap-

proximately 200-300 K lower than what were observed at JF5. The logging point was positioned in the upper layer, at the inside of the enclosure. Simulations, where combustion in the upper layer was observed, predicted more correct temperatures, giving the observed combustion in the upper layer of JF5. The big vent case and the KFX geometry case were some of the cases that most clearly showed ignition and flames in the upper layer of the enclosure.

At logging point 3, most of the cases under-predicted the stable temperatures in JF5, given in Fig. (1.4)(p.11). The stable temperatures of JF5 were higher than what were observed for all the simulated cases. Some of the cases, like the KFX geometry case, given in Fig. (4.3)(p.50), the large dispersion angle case (given in Fig. (4.38)(p.77)) and the adiabatic case (given in Fig. (4.46)(p.84)), correctly predicted the maximum temperatures seen in JF5, but only due to a final sharp increase in temperatures. It is possible that the under-predictions seen by the simulated cases, were due to logging point 3 being positioned close to the fuel spray. The lower temperature fuel spray could therefore have influenced the recorded temperatures. This explanation was further confirmed by the final temperature increase, because the time of this temperature increase corresponded with the time of reduction of the fuel release. This could possibly allow for the flame to enter positions earlier occupied by the fuel spray.

For the logging point 4, similar trends as observed at logging point 2 were observed. The cases with combustion in the upper layer of the compartment: The KFX geometry (given in Fig. (4.4)(p.50)), small diameter (given in Fig. (4.31)(p.72)) and big vent (given in Fig. (4.55)(p.91)) cases, correctly predicted the temperatures. The KFX geometry case even over-predicted the temperatures by up to 400 K. The cases without observed combustion in the upper layer under-predicted the stable temperatures of JF5 (given in Fig. (1.4)(p.11)), but for many of these cases the observed final temperature increase was comparable to the stable temperatures observed at JF5. This observation was further confirmed by the results obtained for the low fuel flow rate case. The low fuel flow rate case, given in Figs. (4.17-4.24)(p.61-p.66) gave quite good temperature predictions at all the logging points, indicating that the ignition and temperature of the upper layer were dependent on flame stoichiometry.

In this thesis simulations with different droplet diameters were conducted. In JF5, the droplets were observed to hit the ceiling, and droplet rain from the ceiling, forming small pools on the floor, was observed initially. Of the three simulations, investigating the droplet diameter, only the large diameter case droplets impinged on the ceiling, as seen in Fig. (4.25)(p.68). Due to the modelling of the droplets being terminated or evaporated, when impinging on surfaces no droplet rain from the ceiling was observed. Interestingly, the initial droplet diameters specified in the large diameter case were significantly larger than the ones calculated in Sec. (3.1.3), or given in Sec. (1.2.1). For some of the tests in Blast and Fire Engineering for topside structure [4], the distance between the release point and the ceiling was observed to be too short to allow full atomisation and droplet evaporation. Given the large differences in results obtained with different droplet diameters, it is possible that

a more detailed spray dispersion and droplet break up model could be of significant importance.

The observations of case sensitivity and critical parameters needed for ignition of the upper layer, were also observed in the Blast and Fire for Topside structures, test programme F3 [4]. It was observed that for obtaining the high temperatures at the inside of the enclosure in the the test programme F3, an escalation of combustion was needed. This escalation of combustion, was thought to be related to the forming of a high temperature core zone and "radiation trapping". For this high temperature core zone to stabilize, a critical size had to be reached. If a sufficiently large temperature core zone was established, the radiation would be "trapped" inside this zone. With radiation trapping, radiation from the core zone were absorbed by layers close to the core zone and radiated back to the core zone, giving increased growth of the core zone until other limiting conditions occur. Limiting conditions could be oxygen transport to the core zone, limiting the thermal energy release. As observed in the simulations in this thesis, for the formation of the high temperature core zone, initial conditions and the solid geometry seemed to be of importance. Flow patterns were also observed to influence fire development, with combustion product and buoyancy driven flows being especially important. Buoyant plumes lower down in the compartment were observed being able to set up different flow patterns, which could explain the flow patterns observed in this thesis for the small diameter case compared to the large diameter case and the advanced geometry case (base case). In Chamberlain et al. [4] it was also observed that as the underventilation was increased in the cases, the higher temperatures was observed to move closer to the vent, with the most intense combustion in the lower region of the smoke layer. This led to unstable layering, which induced mixing and the appearance of temperature oscillations. Similar differences as observed between the low fuel flow rate case and the advanced geometry case (base case) were also observed in fire tests in Chamberlain et al. [4], where high mass flow rates of fuel gave a highly ventilation controlled fire, where the lack of oxygen within the compartment limited the internal combustion to a relatively low intensity. As the fuel could not burn completely inside the compartment, long external flames were observed.

Chapter 6

Conclusions and Recommendations for Further Work

In this thesis, a parameter study investigating the effects of enclosure modelling and spray dispersion on fire development has been conducted. A set of simulations has been created in Kameleon FireEx (KFX), and compared against the fire test JF5 in Blast and Fire Engineering for Topside Structures, Test Programme F3.

The results from the simulations, revealed that some parameters are more decisive on fire development than others. A study into the effect of fuel spray droplet diameters, conducted in this thesis, showed that different fuel spray droplet diameters gave very different results. The highest temperatures were recorded in the case with the smallest fuel spray droplet diameter, while the case with the largest fuel spray droplet diameter also recorded high temperatures. The explanation for the different temperatures and flame developments, is thought to be related to different flow distributions at the inside of the compartment. In this thesis, it was also found, that the enclosure modelling and spray fuel flow rate are important parameters. A significant reduction in fuel flow rate, led to a significant increase in temperatures.

Some of the simulations predicted the fire development of the experimental fire test JF5 quite accurately, while some of the simulations did not. The cases that most accurately predicted the experimental data from JF5, while also using comparable input data, were a case with relatively small droplet diameters (the small diameter case), and a case with a detailed enclosure model, created through CAD import in KFX (the KFX geometry case). The KFX geometry case enclosure model was the most detailed of the enclosure models used in this thesis. This indicates that valid simulations, on under-ventilated fires, set demands on how detailed an enclosure model should be.

Almost all of the simulations had challenges with predicting temperatures, at least at one of the logging points. Although discrepancies from the fire test JF5 were found for most of the cases, the high temperatures at different positions, observed for different cases investigating different parameters, indicate that a valid simulation of JF5 is possible within the software. Given the varied results of the simulations, the question is on choosing correct parameters.

Much and good information about the simulated tests, as well as information on spray dispersion and geometry modelling are needed for prediction of correct flame developments.

This thesis has shown that a spray fire in an under-ventilated enclosure is sensitive to changes in enclosure model specifications and spray dispersion. In the simulations, it was shown that combustion in the upper layer, at the inside of the enclosure, is the deciding factor for obtaining the high temperatures. The simulated cases with combustion in the upper layer, generally recorded more stable temperature distributions than the cases without upper layer combustion. As has been found in this thesis, as well as in Chamberlain et al. [4], for combustion in the upper layer of the enclosure, critical states need to be met. Air entrainment in the upper layer of the compartment seems to be the deciding factor for upper layer combustion. The modelling of the enclosure geometry and spray dispersion have shown to significantly influence flow distributions at the inside of the enclosure. Hence, a detailed enclosure geometry model and spray model are of importance.

In this thesis, modelling challenges regarding combustion hierarchy in under-ventilated fires have also been discussed. As found in Gottuk et al. [12] and in this thesis, estimating correct compositions of H_2 and CO is a challenge. For under-ventilated fires, the O_2 inside the enclosure is depleted, giving little H_2 and CO combustion. Hydrogen is known to react fast [38](p.148-172), raising the question if the reaction hierarchy should be altered with H_2 combustion being prioritized.

The indicated sensitivity of the fire test JF5, found in this thesis, influences the interpretation of the results. The differences between the simulated cases were drastic, and it is a possibility that important developments are obscured by the large differences between the cases. Conclusions about parameters can therefore not be drawn on the basis of the results obtained in this thesis, without much more research on specific parameters. In this research, cases with small variations within one parameter could be conducted to further expand the knowledge on the effect of certain parameters. The indicated high case sensitivity would also set requirements on the available information from the experimental data. In the experimental data, plentiful information are provided on the compartment design and fuel release conditions. As shown by the simple models used for calculating droplet diameter and dispersion angle in this thesis, it is possible to validate droplet break up models based on the experimental data in JF5.

The results presented in this thesis could be used in discussions on fire safety design in under-ventilated enclosures. The modelling uncertainties are too large to draw any conclusions on the validity of the simulation software. Based on the results and modelling uncertainties, it is not possible to conclude that one of the simulation cases is better suited for the simulation of under-ventilated spray fires. Giving that fire safety design to a large degree is based on fire simulations, good predictions based on validations against experimental results are important. This thesis has shown that the uncertainties present in the modelling could be crucial to the simulation results, and further research is needed for being able to accurately predict fire developments.

Recommendations for Further Work

In this thesis many uncertainties regarding correct modelling of geometry and spray dispersion have been discovered. The recommendations for further work are therefore based on further research into parameters influencing fire development.

- The droplet modelling in this thesis showed discrepancies from the observed spray dispersion in fire test JF5 in Blast and Fire Engineering for Topside Structures, Test Programme F3. Given the significant impact a difference in droplet diameter has shown on the fire simulations in this thesis, more experimental research on spray distribution and research on a valid droplet break up model, should be conducted.

- The uncertainties observed in the results in this thesis, indicate the possibility of more simulations, on this test case and other test cases, for further increasing information on the parameter impacts.

- The combustion hierarchy specified in this thesis could give incorrect species compositions in the rich zones at the inside of the enclosure. A study investigating the effect of combustion hierarchy on fire development in under-ventilated enclosures could therefore be of importance.

- The geometry modelling choices investigated in this thesis revealed different results. The difference in results seemed to be related to how detailed the geometry model was. A study into geometry model demands needed for correct simulations could be done.

- In this thesis, the results indicated that the solid structures at the inside of the enclosure did not significantly affect flow distributions. A more thorough research of the effect of solid structures at the inside of the enclosure, on flow distributions in under-ventilated fires, could be conducted.

- The results in this thesis showed that the flame development at the inside of the compartment was highly dependent on air entrainment. In Drangsholt et al. [6], the equivalence ratio between inflowing air and fuel release is mentioned. A study on the different simulations in this thesis, based on the global equivalence ratio concept presented in Pitts [33], could be conducted.

Bibliography

[1] N. Ashgriz. *Handbook of Atomization and Sprays, Theory and Applications*. Springer, Toronto, Canada, 2011.

[2] C. L. Beyler. Major species production by diffusion flames in a two-layer compartment fire environment. *Fire Safety Journal*, 10:47–56, 1986.

[3] G. A. Chamberlain. An experimental study of large-scale compartment fires. *Process Safety and Environmental Protection: Transactions of the Institution of Chemical Engineer, Part B.*, 72:211–219, 1994.

[4] G. A. Chamberlain, M. A. Persaud, R. Wighus, and G. Drangsholt. *Blast and Fire Engineering for Topside Structures. Test Programme F3, Confined Jet and Pool Fires. Final Report*. SINTEF NBL, Trondheim, Norway, 2008.

[5] W. Chung and C. B. Devaud. Buoyancy-corrected k–ϵ models and large eddy simulation applied to a large axisymmetric helium plume. *International Journal for Numerical Methods in Fluids*, 58:57–89, 2008.

[6] G. Drangsholt, G. Tronstad, R. Wighus, L. E. Lønvik, and K. Nygård. *Blast and fire engineering for topside structures, Test programme F3, Confined Jet and Pool Fires, Technical report for test JF5*. Sintef NBL, 1996.

[7] I. S. Ertesvåg. *Turbulent Strøyming og Forbrenning*. Tapir, Trondheim, Norway, 2000.

[8] G. M. Faeth. Evaporation and combustion of sprays. *Prog. Energy Combust. Sci.*, 9:1–76, 1983.

[9] J. D. Felske and C. L. Tien. Calculation of the emissivity of luminous flames. *Combustion Science and Technology*, 7:25–31, 1973.

[10] G. A. Gerolymos and I. Vallet. Implicit computation of three-dimensional compressible navier–stokes equations using k-epsilon closure. *AIAA Journal*, 34:1321–1330, 1996.

[11] D. T. Gottuk and B. Y. Lattimer. Effect of combustion conditions on species production. *SFPE Handbook of Fire Protection Engineering*, pages 486–528, 2016.

[12] D. T. Gottuk, R. J. Roby, and C. L. Beyler. The role of temperature on carbon monoxide production in compartment fires. *Fire Safety Journal*, 24:315–331, 1995.

[13] I. R. Gran. *Mathematical modeling and numerical simulation of chemical kinetics in turbulent combustion*. Universitetet i Trondheim, Norges tekniske høgskole, Trondheim, Norway, 1994.

[14] C. Hwang, A. Lock, M. Bundy, E. Johnsson, and G. H. Ko. Studies on fire characteristics in over- and underventilated full-scale compartments. *Journal Of Fire Sciences*, pages 459–486, 2010.

[15] C. Hwang, A. Lock, M. Bundy, E. Johnsson, and G. H. Ko. Effects of fuel location and distribution on full-scale underventilated compartment fires. *Journal Of Fire Sciences*, 29:21–52, 2011.

[16] R. J. Kee, F. M. Rupley, and J. A. Miller. The chemkin thermodynamic data base. *Sandia Report SAND89-8009*, 1990.

[17] H. J. Kim and D. G. Lilley. Flashover: A study of parameter effects on time to reach flashover conditions. *Journal of Propulsion and Power*, 18:669–673, 2002.

[18] B. E. Launder and D. B. Spalding. The numerical computation of turbulent flows. *Computer Methods in Applied Mechanics and Engineering*, 3:269–289, 1974.

[19] B. Leckner. Spectral and total emissivity of water vapor and carbon dioxide. *Combustion and Flame*, 19:33–48, 1972.

[20] M. Liberman. *Introduction to Physics and Chemistry of Combustion*. Springer, Uppsala, Sweden, 2008.

[21] F. C. Lockwood and N. G. Shah. A new radiation solution method for incorporation in general combustion prediction procedures. *Eighteenth Symposium (International) on Combustion*, pages 1405–1414, 1981.

[22] B. F. Magnussen. On the structure of turbulence and a generalized eddy dissipation concept for chemical reaction in turbulent flow. *19th American Institute of Aeronautics and Astronautics Aerospace Science Meeting*, 1981.

[23] B. F. Magnussen. Modeling of no$_x$ and soot formation by the eddy dissipation concept. *Int. Flame Research Foundation, 1st Topic Oriented Technical Meeting*, 1989.

[24] B. F. Magnussen. The eddy dissipation concept, a bridge between science and technology. *Invited paper at ECCOMAS Thematic Conference on Computational Combustion*, 2005.

[25] B. F. Magnussen and B. H. Hjertager. On mathematical modeling of turbulent combustion with special emphasis on soot formation and combustion. *Symposium (International) on Combustion*, 16:719–729, 1977.

[26] A. C. Merrington and E. G. Richardson. The break-up of liquid jets. *The Proceedings of the Physical society, Vol. 59, Part 1*, 1947.

[27] J. A. Miller and C. T. Bowman. Mechanism and modeling of nitrogen chemistry in combustion. *Progress in Energy and Combustion Science*, 15:287–338, 1989.

[28] M. F. Modest. *Radiative Heat Transfer, 3rd Ed.* Elsevier, Oxford, UK, 2013.

[29] Y. Onuma and M. Ogasawara. Studies on the structure of a spray combustion flame. *Symposium (International) on Combustion*, 15:453–465, 1975.

[30] Y. Onuma, M. Ogasawara, and T. Inoue. Further experiments on the structure of a spray combustion flame. *Symposium (International) on Combustion*, 16:561–567, 1977.

[31] W. M. Pitts. Reactivity of product gases generated in idealized enclosure fire environments. *Twenty-Fourth Symposium (International) on Combustion/The Combustion Institute*, pages 1737–1746, 1992.

[32] W. M. Pitts. Application of thermodynamic and detailed chemical kinetic modeling to understanding combustion product generation in enclosure fires. *Fire Safety Journal*, 23:271–303, 1994.

[33] W. M. Pitts. The global equivalence ratio concept and the formation mechanisms of carbon monoxide in enclosure fires. *Prog. Energy Combust. Sci.*, 21:197–237, 1995.

[34] W. Rodi. Turbulence models and their application in hydraulics. *IAHR, Delft, Netherlands*, 1980.

[35] W. Rodi. Introduction to the modeling of turbulence, examples of turbulence model applications. *Lecture Series 1991-02, von Karman Institute for Fluid Dynamics, Belgium*, 1991.

[36] K. D. Steckler, J. G. Quintiere, and W. J. Rinkinen. Flow induced by fire in a compartment. *Nineteenth Symposium (International) on Combustion*, 19:913–920, 1982.

[37] J. C. Tannehill, D. A. Anderson, and R. H. Pletcher. *Computational Fluid Mechanics and Heat Transfer*. Taylor and Francis, USA, 2nd edition, 1997.

[38] S. R. Turns. *An Introduction to Combustion, Concepts and Applications, 2nd Ed.* Mcgraw-Hill, Boston, 2000.

[39] B. E. Vembe, K. E. Rian, J. K. Holen, N. I. Lilleheie, B. Grimsmo, and M. T. *Theory manual*. Computational Industry Technologies AS, Trondheim, Norway, 2001.

[40] B. E. Vembe, R. N. Kleiveland, B. Grimsmo, N. I. Lilleheie, K. E. Rian, R. Olsen, B. Lakså, V. Nilsen, J. E. Vembe, and T. Evanger. *KFX Furcifier - User Manual*. Computational Industry Technologies AS., Trondheim, Norway, 2014.

[41] H. K. Versteeg and W. Malalasekara. *An introdution to computational fluid dynamics The finite volume method, 1st Ed.* Longman Scientific & Technical, England, 1995.

[42] S. Welch, A. Jowsey, S. Deeny, R. Morgan, and J. L. Torero. Bre large compartment fire test–characterising post-flashover fires for model validation. *Fire Safety Journal*, 42: 548–567, 2007.

[43] A. Williams. *Combustion of Liquid Fuel Sprays*. Butterworths, Leeds, UK, 1990.

[44] H. W. M. Witlox, M. Harper, A. Oke, P. J. Bowen, and P. Kay. Sub-cooled and flashing liquid jets and droplet dispersion i. overview and model implementation/validation. *Journal of Loss Prevention in the Process Industries*, 23:831–842, 2010.

[45] J. Wu, Y. Zhang, X. Gou, M. Yan, E. Wang, and L. Liu. Experimental research on gas fire backdraft phenomenon. *Procedia Environmental Sciences*, 11:1542–1549, 2011.